MINERALOGICAL STUDY OF URANIUM AND NIOBIUM MINERALIZATION AT THE MAIN INTRUSION OF THE LOFDAL CARBONATITE COMPLEX, NAMIBIA, AFRICA

Matthew A. Gaudet

Submitted in Partial Fulfillment of the Requirements

for the Degree of Bachelor of Science, Honours

Department of Earth Sciences

Dalhousie University, Halifax, Nova Scotia

April 2013

Distribution License

DalSpace requires agreement to this non-exclusive distribution license before your item can appear on DalSpace.

NON-EXCLUSIVE DISTRIBUTION LICENSE

You (the author(s) or copyright owner) grant to Dalhousie University the non-exclusive right to reproduce and distribute your submission worldwide in any medium.

You agree that Dalhousie University may, without changing the content, reformat the submission for the purpose of preservation.

You also agree that Dalhousie University may keep more than one copy of this submission for purposes of security, back-up and preservation.

You agree that the submission is your original work, and that you have the right to grant the rights contained in this license. You also agree that your submission does not, to the best of your knowledge, infringe upon anyone's copyright.

If the submission contains material for which you do not hold copyright, you agree that you have obtained the unrestricted permission of the copyright owner to grant Dalhousie University the rights required by this license, and that such third-party owned material is clearly identified and acknowledged within the text or content of the submission.

If the submission is based upon work that has been sponsored or supported by an agency or organization other than Dalhousie University, you assert that you have fulfilled any right of review or other obligations required by such contract or agreement.

Dalhousie University will clearly identify your name(s) as the author(s) or owner(s) of the submission, and will not make any alteration to the content of the files that you have submitted.

If you have questions regarding this license please contact the repository manager at dalspace@dal.ca.

Grant the distribution license by signing and dating below.

______________________________	______________________________
Name of signatory	Date

DALHOUSIE
UNIVERSITY
Inspiring Minds

Department of Earth Sciences
Halifax, Nova Scotia
Canada B3H 4J1
(902) 494-2358
FAX (902) 494-6889

DATE: ____________________

AUTHOR: ____

TITLE: ____

____

____

____

Degree: ____________ Convocation: ____________ Year: ____________

Permission is herewith granted to Dalhousie University to circulate and to have copied for non-commercial purposes, at its discretion, the above title upon the request of individuals or institutions.

____
Signature of Author

THE AUTHOR RESERVES OTHER PUBLICATION RIGHTS, AND NEITHER THE THESIS NOR EXTENSIVE EXTRACTS FROM IT MAY BE PRINTED OR OTHERWISE REPRODUCED WITHOUT THE AUTHOR'S WRITTEN PERMISSION.

THE AUTHOR ATTESTS THAT PERMISSION HAS BEEN OBTAINED FOR THE USE OF ANY COPYRIGHTED MATERIAL APPEARING IN THIS THESIS (OTHER THAN BRIEF EXCERPTS REQUIRING ONLY PROPER ACKNOWLEDGEMENT IN SCHOLARLY WRITING) AND THAT ALL SUCH USE IS CLEARLY ACKNOWLEDGED.

Abstract

The Lofdal carbonatite complex, Namibia, Africa, intruded into basement rocks of the Huab Metamorphic Complex in the late Neoproterozoic during rifting between the Congo and Kalahari cratons. The complex is currently exposed in a basement inlier of the Congo craton called the Welwitschia inlier. The Lofdal carbonatite complex consists of nepheline syenite and carbonatite as plugs and dykes, with associated breccias and fenites, an alteration rock. The Main intrusion, the focus area of this study, consists of a sovite plug, intruding into overlying nepheline syenite body accompanied by associated contact phases, potassic fenite and siliciocarbonatite. Potassic fenites are dominantly composed of potassium feldspar, and are metasomatised from nepheline syenite. Siiciocarbonatites are dominantly composed of magmatic coarse-grained aegirine, calcite, and apatite and are interpreted to have formed from a residual carbonatite melt.

A total of twenty-two representative end-member samples were collected from the various lithologies at the Main intrusion. Petrographic descriptions, whole rock geochemistry, and mineral chemistry analyses of these samples provides insight into the magmatic history of the Main intrusion, and the nature and origin of niobium and uranium mineralization. Pyrochlore, a relatively common accessory mineral in potassic fenites and siliciocarbonatites, with a unit cell structure $A_2B_2O_6Z$ is determined to be the main host mineral for niobium and uranium. The cores of pyrochlores from siliciocarbonatites are interpreted to have grown in a calm magmatic environment. The rims of pyrochlores from siliciocarbonatites are uranoan pyrochlore and uranpyrochlore and are interpreted to have crystallized from a residual carbonatite melt, rich in volatiles and silica, in the presence of magmatic fluids. The growth of these rims is interpreted to have been enhanced by rapid crystallization of fluorapatite. The siliciocarbonatites lithology, then, is interpreted to be late-magmatic in origin, while the potassic fenite lithology is interpreted to be the result of an early homogeneous potassium-rich metasomatic event, overprinted by a later carbonate and sodium-rich heterogeneous alteration event. Metasomatic fluids are interpreted to have originated from the carbonatite body, released during various stages of crystallization.

Table of Contents

Table of Contents

List of Figures

List of Tables

Acknowledgements

I would like to thank my supervisors Yana Fedortchouk and Scott Swinden. Yana was an excellent mentor for analytical techniques, petrographic descriptions, and interpretation of mineral chemical and geochemical data. Scott provided me with an exciting and challenging project, and an abundance of field information and literature, and a chance to meet with the Namibia Rare Earth's Ltd. team. He was also an excellent mentor for interpreting the complex-scale implications of my study, allowing me to really maximize the use of my data set to arrive at some very interesting interpretations.

I would also like to thank Anne-Marie Ryan and Mike Young. Anne-Marie was an enormous help with interpreting whole rock geochemistry results and providing me with strategies for locating uranium host specimens in the early stages of this study. Mike was a great help with interpreting textural evidence and putting those observations into a larger context to help me arrive at some solid conclusions.

Additionally I would like to thank Ryan Kressall for all of his help understanding carbonatite complexes. Ryan's previous experience and willingness to engage in discussion of possible models was a huge asset to furthering my understanding of these types of occurrences.

I would also like to thank Richard Cox and Dan Macdonald for all of their help with the microprobe work in this study. Dan was a huge help with understanding the theory behind microprobe work and proper collection of quantitative data. Richard was an immense help with helping me to acquire the necessary data for interpreting pyrochlore in this study; without his help producing X-ray composition maps I can't imagine how I would have been able to come so far in my interpretations.

Chapter 1: Introduction

1.1 General Statement

The Lofdal area, Namibia, Africa, is host to a mid Neoproterozoic rifting related alkaline silicate – carbonatite intrusive complex. Exploration to date has primarily focused on light rare earth element (LREE) and variably heavy rare earth element (HREE) enriched carbonatite dikes on the property. However, during airborne radiometric surveys carried out in 2010, two significant uranium anomalies were identified at the Main intrusion. A grab sampling program over the south western uranium anomaly returned maximum enrichment grades of approximately 0.1% U_3O_8, and 1.2% Nb_2O_5 (Swinden, 2012). These grades are economically significant, and similar to grades at actively producing uranium and niobium deposits. The purpose of this study is to use geological and mineralogical observations to provide an interpretation of the magmatic and post-magmatic processes which may have produced the observed lithologies, and associated uranium and niobium mineralization. Furthermore, these observations are used to provide an interpretation of the evolutionary history of the Main intrusion.

1.2 Classification, Mineralogy, and Occurrences

Carbonatites are defined, according to the IUGS igneous classification guide, as volcanic or plutonic rocks containing greater than 50 modal per cent carbonate minerals (*Le Maitre 2002*). They can be subdivided into four categories: calcite-carbonatites, dolomite-carbonatites, ferrocarbonatites, and natrocarbonatites. The terms calcite or dolomite carbonatite should be used when the dominant carbonate mineral present is either calcite or dolomite, whereas ferrocarbonatite and natrocarbonatite should be used when the majority of carbonate minerals are either rich in iron or alkalis, respectively (Le Maitre 2002). An alternative naming convention proposed by Wooley and Kempe (1989) uses a chemical classification scheme, where carbonatites may be classified based on the dominant weight per cent oxide present, as shown in *Figure 1.1*. Finally, if the rock contains more than 20 per cent SiO_2, the term “siliciocarbonatite” may be applied (Le Maitre, 2002).

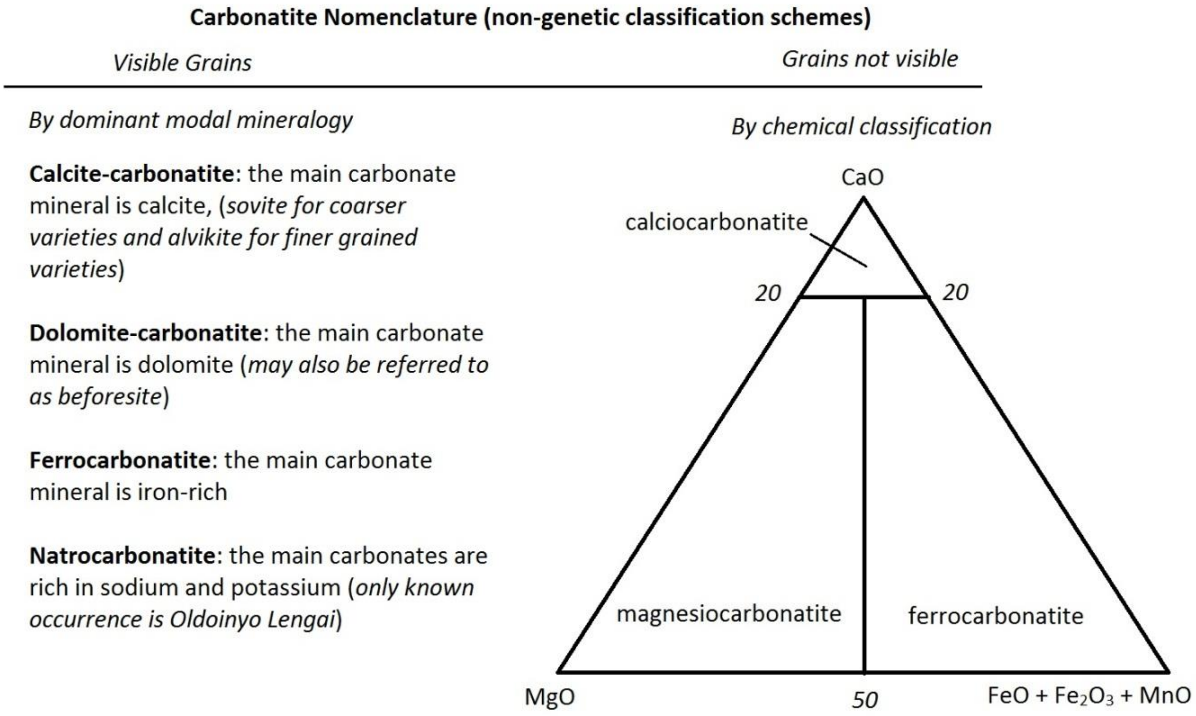

Carbonatite Nomenclature (non-genetic classification schemes)

Visible Grains

By dominant modal mineralogy

Calcite-carbonatite: the main carbonate mineral is calcite, (*sovite for coarser varieties and alvikite for finer grained varieties*)

Dolomite-carbonatite: the main carbonate mineral is dolomite (*may also be referred to as beforesite*)

Ferrocarbonatite: the main carbonate mineral is iron-rich

Natrocarbonatite: the main carbonates are rich in sodium and potassium (*only known occurrence is Oldoinyo Lengai*)

Grains not visible

By chemical classification

***Figure* 1.1 - Mineralogical and chemical classification schemes for naming carbonatites (After LeMaitre 2002)**

Carbonatite mineralogy-reflects a number of magmatic conditions: an abundance of carbonate, low silica content, high concentrations of rare earth elements, volatiles (CO_2, F, Cl, S) and unusually high concentrations of barium, strontium, rare earth elements, phosphorus, and niobium (Winter 2010). Carbonatites may locally contain economically significant concentrations of barium, fluorine, strontium, vanadium, thorium, uranium, zircon and copper. Their mineralogy is highly variable, with over 280 observed mineral associations; some are common whereas others are incredibly rare. A summary of the diagnostic mineralogy of a carbonatite is shown in *Figure 1.2* after Winter (2010).

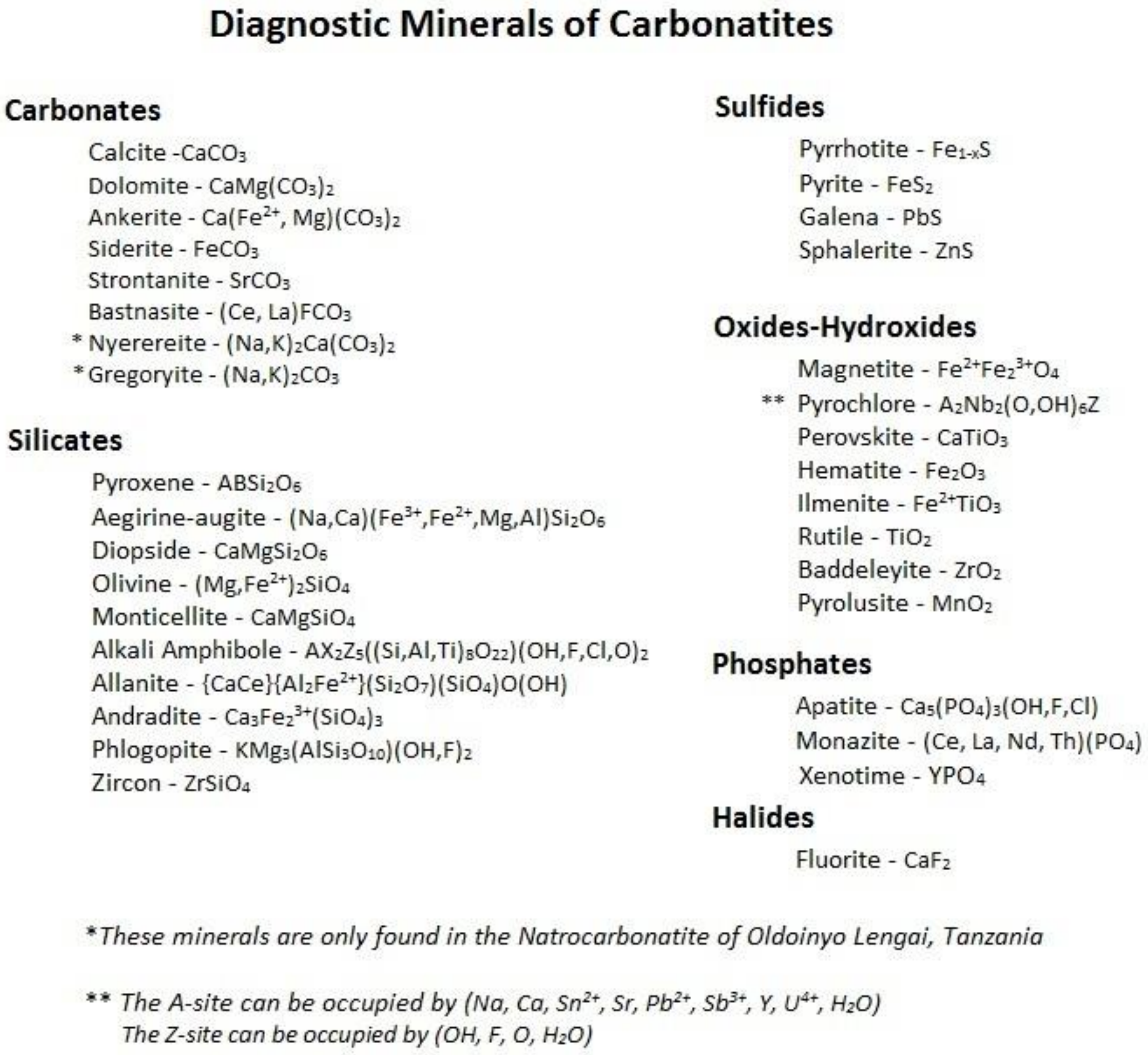

Diagnostic Minerals of Carbonatites

Carbonates

Calcite - $CaCO_3$
Dolomite - $CaMg(CO_3)_2$
Ankerite - $Ca(Fe^{2+}, Mg)(CO_3)_2$
Siderite - $FeCO_3$
Strontanite - $SrCO_3$
Bastnasite - $(Ce, La)FCO_3$
* Nyerereite - $(Na,K)_2Ca(CO_3)_2$
* Gregoryite - $(Na,K)_2CO_3$

Silicates

Pyroxene - $ABSi_2O_6$
Aegirine-augite - $(Na,Ca)(Fe^{3+},Fe^{2+},Mg,Al)Si_2O_6$
Diopside - $CaMgSi_2O_6$
Olivine - $(Mg,Fe^{2+})_2SiO_4$
Monticellite - $CaMgSiO_4$
Alkali Amphibole - $AX_2Z_5((Si,Al,Ti)_8O_{22})(OH,F,Cl,O)_2$
Allanite - $\{CaCe\}\{Al_2Fe^{2+}\}(Si_2O_7)(SiO_4)O(OH)$
Andradite - $Ca_3Fe_2{}^{3+}(SiO_4)_3$
Phlogopite - $KMg_3(AlSi_3O_{10})(OH,F)_2$
Zircon - $ZrSiO_4$

Sulfides

Pyrrhotite - $Fe_{1-x}S$
Pyrite - FeS_2
Galena - PbS
Sphalerite - ZnS

Oxides-Hydroxides

Magnetite - $Fe^{2+}Fe_2{}^{3+}O_4$
** Pyrochlore - $A_2Nb_2(O,OH)_6Z$
Perovskite - $CaTiO_3$
Hematite - Fe_2O_3
Ilmenite - $Fe^{2+}TiO_3$
Rutile - TiO_2
Baddeleyite - ZrO_2
Pyrolusite - MnO_2

Phosphates

Apatite - $Ca_5(PO_4)_3(OH,F,Cl)$
Monazite - $(Ce, La, Nd, Th)(PO_4)$
Xenotime - YPO_4

Halides

Fluorite - CaF_2

**These minerals are only found in the Natrocarbonatite of Oldoinyo Lengai, Tanzania*

*** The A-site can be occupied by (Na, Ca, Sn^{2+}, Sr, Pb^{2+}, Sb^{3+}, Y, U^{4+}, H_2O)*
The Z-site can be occupied by (OH, F, O, H_2O)

***Figure* 1.2 – Diagnostic mineralogy for carbonatites, after (Winter 2010)**

There are just over 500 documented occurrences of carbonatite worldwide *(Figure 1.3)*; the vast majority are found in Africa and Asia, followed by North America and Greenland (Woolley and Kjarsgaard 2008). Of these occurrences, nearly 25% occur without associated alkaline silicate bodies. The other 75% which do show spatial and temporal association with alkaline silicate bodies are broken down into seven types of associations, discussed in *Section 1.3* (Woolley and Kjarsgaard 2008).

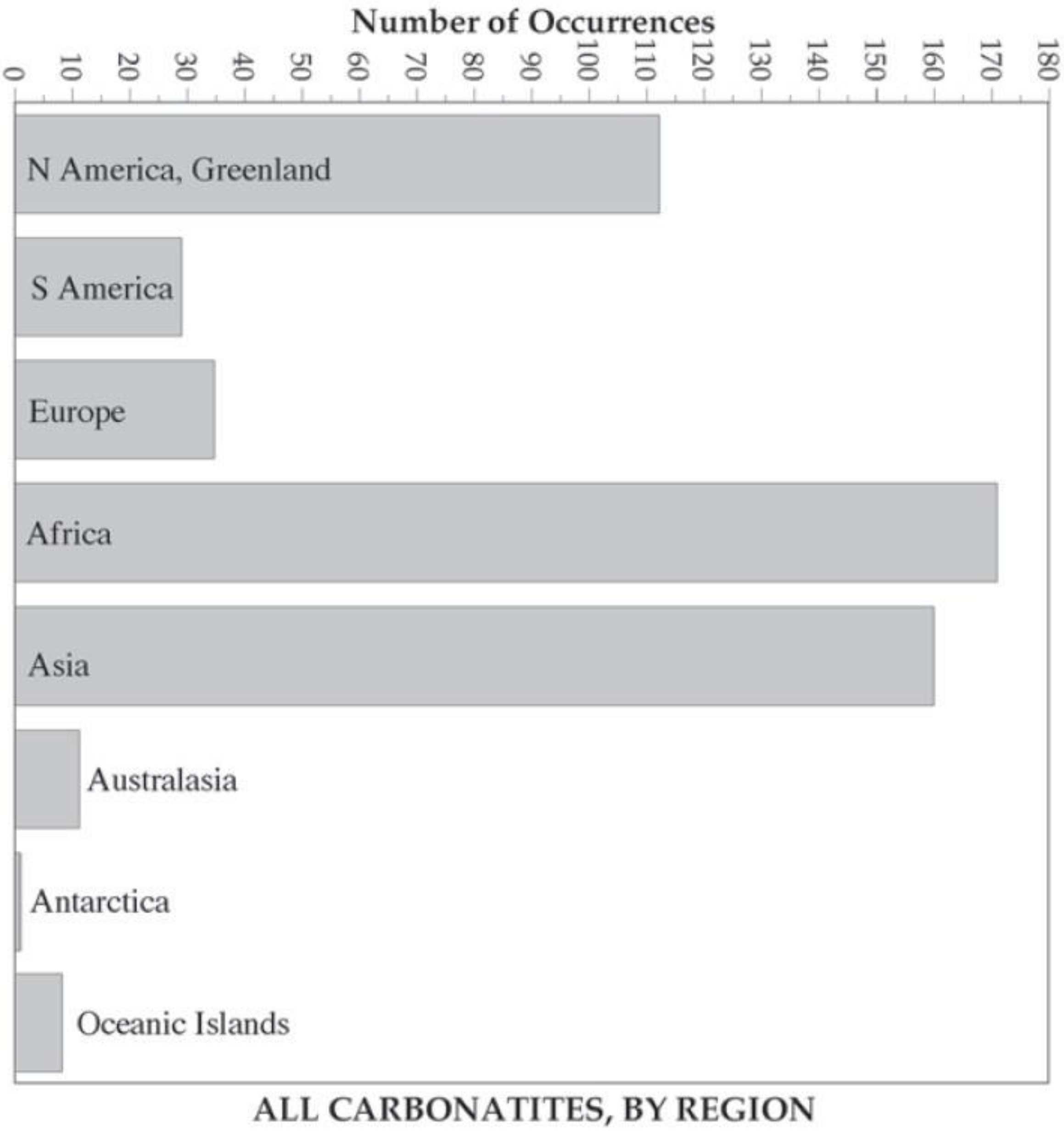

***Figure* 1.3 – Worldwide distribution of over 500 documented Carbonatite occurrences (Woolley and Kjarsgaard 2008)**

1.3 Association with Alkaline Silicates

Of the over 500 carbonatite occurrences mentioned in *Section 1.2*, 75% show a strong spatial and temporal association with alkaline silicates. This relationship is demonstrated in *Figure 1.4*, after Woolley and Kjarsgaard (2008), which illustrates the “carbonatite only”, plus seven major alkaline silicate- carbonatite associations. For each, the origins of the carbonatite magma are illustrated, in terms of their relative depth of formation.

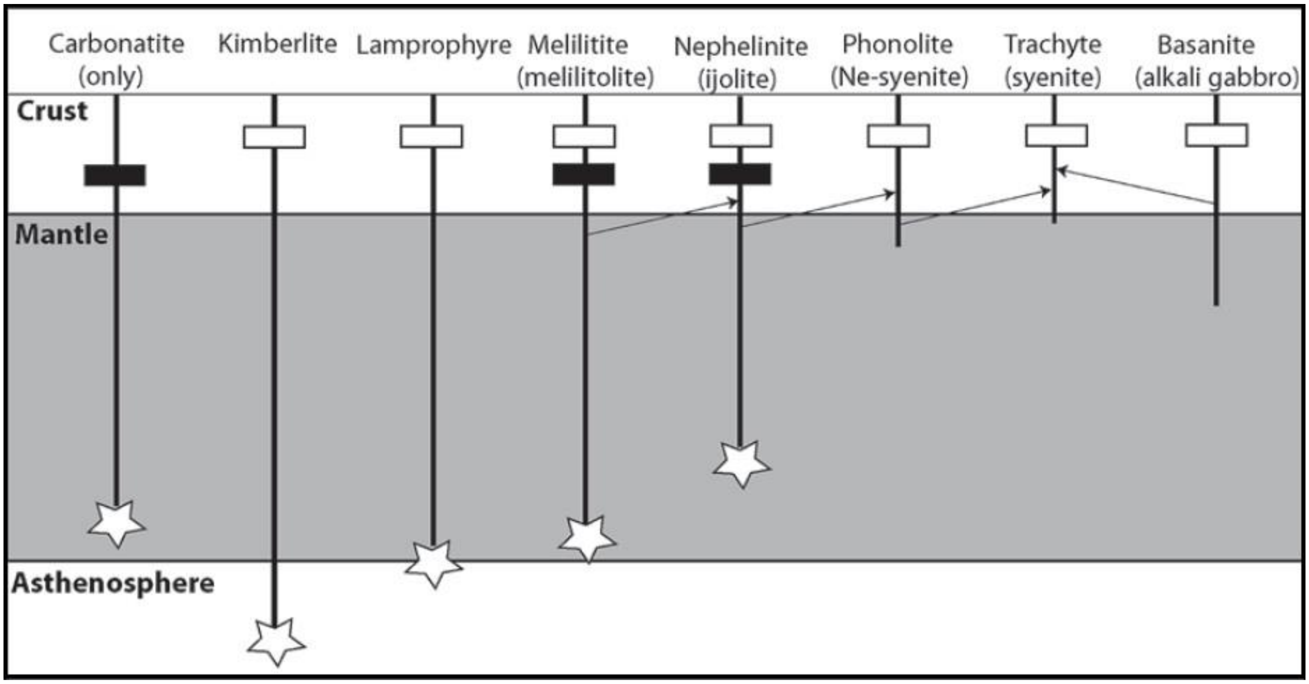

***Figure* 1.4 – Carbonatite occurrences are illustrated in terms of their depth origins, and associations with or without alkaline silicate rocks. White stars - indicate the formation of primary carbonatite magma in the metasomatised mantle. White boxes-indicate the formation of a differentiate carbonatite magma either through crystal fractionation or liquid immiscibility. Black boxes-indicate a known association with cumulate ultramafics, which differentiate at shallow crustal levels. Black lines-indicate a known differentiation of the alkaline silicate series (ie: ijolite is known to differentiate from melilitolite) (after Woolley and Kjarsgaard 2008).**

Carbonatites which occur with no associated alkaline silicate rocks are believed to form only as primary magmas in the metasomatised mantle, and may occur with associated ultramafic cumulate rocks, indicated by the black box on *Figure 1.4*. Kimberlites and lamprophyres with significant carbonate are interpreted to originate from the asthenosphere as indicated by the white stars. Any carbonate-rich portion of these magmas would differentiate at shallow crustal levels as indicated by the white boxes. Carbonatites which are associated with intrusive melilitolites and ijolites, as well as their extrusive equivalents, are interpreted to form via partial-melting of deep metasomatised mantle. These initial magmas commonly fractionate an ultramafic component as well as a carbonatite component, at shallow crustal levels. Finally, carbonatites associated with nepheline syenites, syenites, and alkali gabbros (and equivalent), are formed either by low degrees of partial melting in the upper mantle, or as late-stage differentiates from one of their parental alkaline magmas, indicated by the black lines in *Figure 1.4*. These black lines are based on field observations at the various documented carbonatite occurrences.

One final important point to note, is that carbonatite magmas originating in the mantle are not necessarily involved in shallow differentiation. Carbonatites associated with kimberlites, lamprophyres, melilitolites and ijolites, may form either as a primary magma in the mantle, or as a product of crystal differentiation at shallow crustal levels (Woolley and Kjarsgaard 2008).

The carbonatite complex at Lofdal falls within the nepeheline syenite silicate association. This association is the third most common (14% of all documented magmatic carbonatites). The data of Woolley and Kjarsgaard (2008) suggests that statistically, it is unlikely that carbonatites associated with nepheline syenites could have originated in the mantle as primary magmas. It is therefore suggested that The Lofdal carbonatites are likely to have originated via shallow crustal differentiation, either through fractionation or liquid immiscibility.

1.4 Carbonatite Genesis

Determining the origins of carbonatitic magma has proven challenging, and has been the topic of debate for almost a century. Leading up to the 1950's many geologists believed that carbonatites were "remobilized limestones, marble xenoliths, or precipitates from hydrothermal solutions" (Winter 2010). In the 1950's Wyllie & Tuttle (1960) demonstrated that in a CO_2 rich system, calcite could melt at relatively low P/T conditions. This discovery reignited interest in the study of carbonatite genesis within the scientific community (Winter 2010). Since the 1960's two generally accepted models have emerged to explain the origins of carbonatite magmas based both on experimental studies and field associations.

In the first view, carbonatite magmas form as primary magmas in a metasomatised lithospheric mantle, and may or may not have 'accompanying' alkaline silicate magmas (*Figure 1.5 B*, Woolley and Kjarsgaard 2008). In the second view, carbonatite magmas form as a differentiation product from an alkaline silicate parent, either by fractionation or liquid immiscibility (*Figure 1.5 A*, Woolley and Kjarsgaard 2008).

In *Figure 1.5 A*, three independent partial melts are generated at different levels in the mantle, with the melilitite magma being carbonate saturated. As these magmas ascend to shallow crustal levels, the carbonated magma will differentiate through fractionation or liquid immiscibility to produce a carbonatite magma. These four magmas will be emplaced, with only one of these magmas being genetically linked to the carbonatite magma. In contrast, *Figure* 1.5B shows two independent magmas of carbonatite and nephelinites which were generated at different levels in the mantle, and were emplaced in close proximity.

The key to distinguishing whether or not a carbonatite body is genetically related to an alkaline silicate body is through study of radiogenic isotopes. Similar isotopic signatures will be observed for carbonatite and alkaline silicate bodies which share a common source. Field observations demonstrate that while many carbonatites with spatially associated alkaline silicate rocks show a similar isotopic signature, there are a number of occurrences where the associated alkaline silicate rocks contain distinct isotopic signatures. This has led to a large debate about whether or not both models are indeed valid, or whether there is an issue of observation bias. On one hand, carbonatite occurrences with no associated alkaline silicate rocks constitute 24% of all magmatic carbonatites. Even considering the remaining occurrences which do have spatially associated alkaline silicate rocks, not all of them show isotopic signatures that imply a genetic relationship. From this point of view, the remaining complexes which show similar isotopic signatures could be attributed to a model in which both bodies formed at similar mantle depths during separate partial melting events. On the other hand, many of the paired occurrences do show similar isotopic signatures. It is possible that in the cases where similar isotopic signatures are not observed, the true genetically associated alkaline silicate body was lost to erosion or remains otherwise undiscovered (*Figure* 1.5 A).

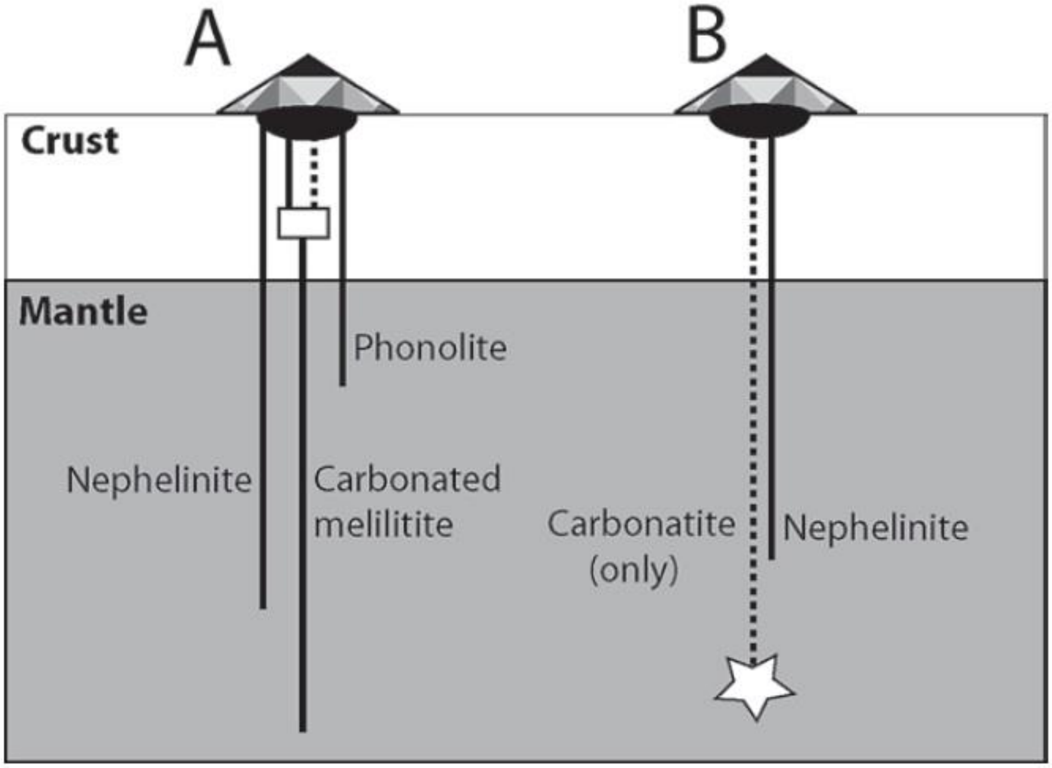

***Figure* 1.5 – (A) A differentiation model to explain the occurrence of a carbonatite magma, which formed as a product of crystal fractionation or liquid immiscibility from a parental carbonated alkaline silicate magma. (B) A primary magma model in which a carbonatite magma and a nephelinite magma are independently derived via partial melting of a metasomatised mantle at different mantle depths. (Woolley and Kjarsgaard 2008)**

In addition to the debate about primary versus differentiation models for the derivation of carbonatite magmas, a second debate has been ongoing about the mechanisms through which a carbonatite magma might differentiate. If the differentiation model is accepted as plausible, the issue then becomes whether or not these carbonatite magmas differentiate though fractional crystallization or through liquid immiscibility. The initial preferred hypothesis followed a silicate fractionation analogue in which fractional crystallization of a carbonated alkaline silicate magma would eventually leave a small residual carbonate melt (Winter 2010). There were a number of outstanding issues with this theory though. If fractionation was indeed the main differentiation mechanism, then one might expect that the alkaline silicate bodies present with associated carbonatite would be significantly larger in volume than the carbonatite body. However, this is not commonly observed. Similarly, one might also expect some sort of gradation between silicate and carbonatite bodies representative of late stage fractionation, also not generally observed in the field. Regardless, fractional crystallization remained the generally accepted theory until the mid-1960's when Koster van Groos and Wyllie first began experimental studies to identify an immiscibility gap between carbonate and silicate magmas. Fascinatingly, these ongoing experiments along with similar experiments by others have identified immiscibility between an alkaline silicate liquid, a carbonatite liquid and an alkaline fluid, above 870°C and 0.1 GPa in a CO_2 saturated system (*Wyllie et al. 1966*). This discovery has offered compelling evidence to explain the relatively similar volumes of carbonatite and associated alkaline silicate, and the lack of observed gradation between the two bodies. However, the debate is ongoing and a general consensus has not been reached about which theory is correct.

1.5 Ore minerals in Carbonatites

Carbonatites are mainly explored as potential sources of phosphorus, niobium, and rare earth elements. Additionally, they are known to possess significant quantities of barium, copper, fluorite, strontium, Vanadium, Thorium and Uranium (*Winter 2010*). Some of the most common ore minerals encountered in carbonatites are listed in *Figure 1.6*.

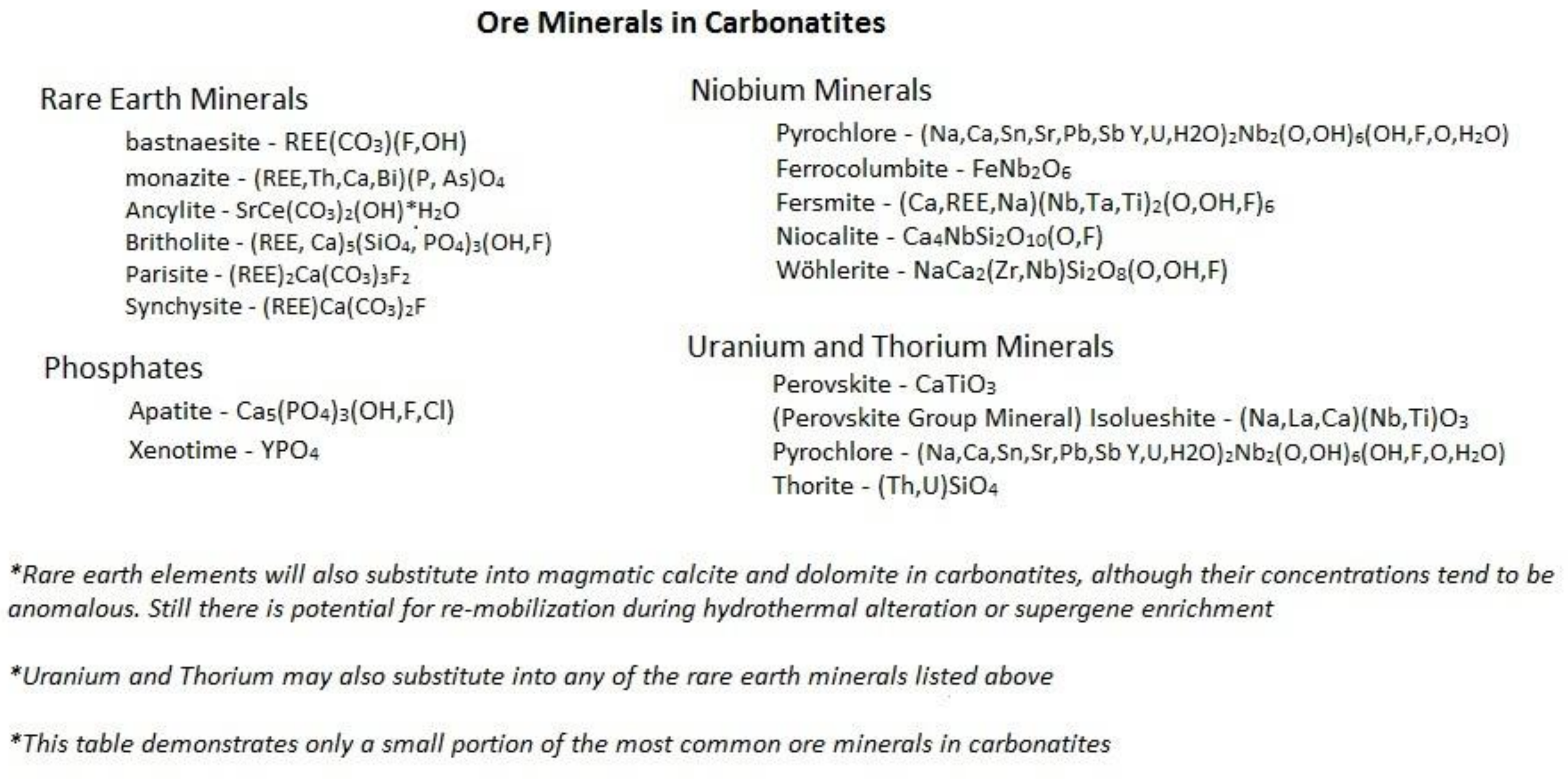

Ore Minerals in Carbonatites

Rare Earth Minerals

bastnaesite - $REE(CO_3)(F,OH)$
monazite - $(REE,Th,Ca,Bi)(P, As)O_4$
Ancylite - $SrCe(CO_3)_2(OH)*H_2O$
Britholite - $(REE, Ca)_5(SiO_4, PO_4)_3(OH,F)$
Parisite - $(REE)_2Ca(CO_3)_3F_2$
Synchysite - $(REE)Ca(CO_3)_2F$

Phosphates

Apatite - $Ca_5(PO_4)_3(OH,F,Cl)$
Xenotime - YPO_4

Niobium Minerals

Pyrochlore - $(Na,Ca,Sn,Sr,Pb,Sb\ Y,U,H2O)_2Nb_2(O,OH)_6(OH,F,O,H_2O)$
Ferrocolumbite - $FeNb_2O_6$
Fersmite - $(Ca,REE,Na)(Nb,Ta,Ti)_2(O,OH,F)_6$
Niocalite - $Ca_4NbSi_2O_{10}(O,F)$
Wöhlerite - $NaCa_2(Zr,Nb)Si_2O_8(O,OH,F)$

Uranium and Thorium Minerals

Perovskite - $CaTiO_3$
(Perovskite Group Mineral) Isolueshite - $(Na,La,Ca)(Nb,Ti)O_3$
Pyrochlore - $(Na,Ca,Sn,Sr,Pb,Sb\ Y,U,H2O)_2Nb_2(O,OH)_6(OH,F,O,H_2O)$
Thorite - $(Th,U)SiO_4$

**Rare earth elements will also substitute into magmatic calcite and dolomite in carbonatites, although their concentrations tend to be anomalous. Still there is potential for re-mobilization during hydrothermal alteration or supergene enrichment*

**Uranium and Thorium may also substitute into any of the rare earth minerals listed above*

**This table demonstrates only a small portion of the most common ore minerals in carbonatites*

***Figure* 1.6 – Common ore minerals associated with carbonatites (after Mariano 1989).**

1.5.1. Rare earths

Carbonatites are well known for their abundance of rare earth elements; however, these elements rarely occur as primary magmatic REE-minerals; they are most abundant as substitutions in oxide, phosphate and carbonate minerals. There are three styles of REE mineralization associated with carbonatites: primary-magmatic, hydrothermal, and supergene.

Economically significant concentrations of primary-magmatic REE minerals are uniquely found at the Mountain Pass mine in California, USA (Mariano 1989). The Sulfide Queen ore-body at Mountain Pass is host to a deposit of over 20 MT grading 8.9% rare earth oxides; the primary source of REE's is bastnaesite-Ce (Castor 2008). With the exception of the Mountain Pass deposit, almost all other economically significant REE deposits related to carbonatites-are the product of either hydrothermal or supergene enrichment

Although rare earth elements are not commonly considered to be mobile in aqueous systems, there is substantial evidence to suggest that LREE's can become mobile in magmatic-fluids by forming neutral fluorine complexes (Andersen 1986). This mobility is a key feature in hydrothermal deposits of REE's related to fluids released by crystallizing carbonatite bodies. The most common rare earth minerals which form hydrothermally are monazite, ancylite, parisite, britholite, synchysite and xenotime; these minerals generally form in veinlets or interstitial fillings surrounding carbonatite intrusions (Mariano 1989). Arguably, these veinlets and interstitial fillings precipitated from high-temperature and high-salinity magmatic fluids as a result of changes in fluid pressures and temperatures, fluid mixing, and fluid interaction with wall-rock (Gieré 1996).

Supergene enrichment of rare earth elements from carbonatite and alkaline rocks involves chemical weathering and formation of enriched laterite deposits. At Araxa, Brazil, this process has resulted in enormous laterite deposits with average grades of 13.5 wt% rare earth oxides (Mariano

1989). Supergene enrichment occurs in tropical environments where extensive chemical weathering is possible. During weathering, carbonates and apatites are dissolved and calcium and magnesium are easily mobilized, leaving residual REE's and PO_4^{3-} to form secondary monazite (Mariano 1989). These laterite deposits can become significantly enriched in secondary REE minerals.

1.5.2. Niobium

Niobium production worldwide comes exclusively from carbonatites; pyrochlore is the primary host mineral in most active production deposits, with ferrocolumbite being targeted in many advanced niobium exploration projects (Mariano 1989). Niobium mineralization is characteristic of most carbonatite deposits; ore minerals of niobium include pyrochlore, ferrocolumbite, fersmite, niocalite, and wohlerite. Pyrochlore in carbonatites occurs as both a primary magmatic phase, and as a hydrothermal phase (Mariano 1989). Ferrocolumbite in many complexes occurs as a primary mineral which may be seen in association with, intergrown with, but not replacing pyrochlore (Mariano 1989). Fersmite is interpreted to form as an alteration product from pyrochlore, in most cases (Mariano 1989). The remaining two niobates niocalite and wohlerite both occur as primary magmatic minerals but are undesirable as a source of niobium owing to their low concentrations (<19 wt% Nb_2O_5) (Mariano 1989).

1.5.3. Phosphorus

Phosphates are the most valuable commodity ($/lb.) mined from carbonatites, with apatite being the source for all carbonatite-derived phosphate products (Mariano 1989). Apatite is considered to be one of the most abundant primary accessory minerals in carbonatites, at times constituting as much as 50 volume per cent (Mariano 1989).

1.5.4. Uranium and Thorium

Uranium and thorium in carbonatites show concentrations higher than the average crustal abundance. However, despite high concentrations of uranium in pyrochlores from Blue River, Fen and

Ngualla, these deposits are not considered economically significant sources of uranium (Mariano 1989). The main ore minerals for uranium and thorium are perovskite, thorite, pyrochlore, and REE minerals, with thorium and uranium usually substituting for sodium and calcium (thorite being an exception) (Mariano 1989).

1.5.5. Fenitization related to carbonatites

An interesting feature of most carbonatite complexes is the frequent presence of an aureole of alteration that develops in the host rock surrounding carbonatite intrusions bodies. This highly alkaline aureole had led to the description of a rock type called a fenite, a name originating from fenite descriptions at the Fen complex in Norway. Fenitization, refers to the process of alkali metasomatism associated with alkaline silicate and carbonatite magmatism (Le Bas 2008). While carbonatites generally contain very little alkali content, they are believed to inherently contain high concentrations of mantle derived alkalis which are lost as a fluid phase during crystallization (Le Bas 2008). There are two recognized types of fenitization: sodic, and potassic (Le Bas 2008).

1.5.6. Potassic Fenites

Potassic fenites are most commonly observed associated with sovite intrusions. The aureole surrounding the intrusion consists of a rock dominated by potassium feldspar, most commonly orthoclase (Le Bas 2008). Field observations show that these fenites form as a result of the earliest intrusive phases of the carbonatite body, whereas later magmatic pulses tend to cause brecciation without the influx of alkaline fluids (Le Bas 2008). During metasomatism, an intense influx of potassic fluids causes recrystallization to form a rock which may be almost entirely composed of potassium feldspar, regardless of the protolith composition (Le Bas 2008). In some complexes, a variety of potassic fenite called a pseudo trachyte has been documented. The pseudo- prefix denotes that these rocks are not magmatic and thus are not true trachytes, despite the nearly similar textures (Le Bas 2008).

A pseudo trachyte consists of small fragments of potassium feldspar which have been mobilized and recrystallized to form parallel aligned laths (Le Bas 2008). They are interpreted to form through melting of high-grade fenite, resulting from the heat of a rising carbonatite magmatic body; this melt becomes mobilized and is emplaced as dikes, sills and plugs within the potassic fenite surrounding the carbonatite body (Le Bas 2008).

1.5.7. Sodic Fenites

The development of sodic fenite is less well documented than potassic fenites. The sodic fenites are generally characterized by the presence of albite, sodic-amphiboles, and sodic-pyroxenes (Le Bas 2008). The sodic fenites of the Silai Patti, North West Frontier Province in Pakistan, contain veins of sovite which cross-cut potassic fenites, containg abundant aegirine and albite; this has been interpreted to mean that potassium fenitization pre-dated the release of sodic fluids, which crystalize albite and aegirine in veins developed along fractures (Le Bas 2008).

Chapter 2: Geological Setting

2.1 Geological History of Southern Africa

The geological history of of southern Africa began in the Archean with the stabilization of four cratonic nuclei: the Zimbabwe, Kaapvaal, Congo, and Kalahari cratons (*Figure 2.1*). From the Paleoarchean to the Mesoproterozoic, sedimentation and subsequent volcanism and metamorphism in basins along the margins of the Zimbabwe and Kaapvaal cratons produced the Limpopo, Namqua-Natal, Zambezi and Mozambique mobile belts (Schneider, 2008). These mobile belts connected the Congo and Kalahari cratons in western South Afrcia to the previously stabilized land mass of eastern South Afrcia (Schneider, 2008). The end of the Mesoproterozoic marks the approximate time of formation of the supercontinent Rodinia (1 Ga).

Rodinia remained stable until about 900 Ma when it began to break apart. In the early Neoproterozoic, rifting occurred between the Kalahari and Congo cratons to form a number of ocean basins, including the Damaran ocean basin (Schneider, 2008). This was accompanied by sedimentation and magmatism along the margins of the rift basin, including the intrusion of carbonatite and associated alkaline bodies of the Lofdal Carbonatite Complex. Following the generation of the Damaran ocean basin, subduction was initiated beneath the Congo craton, which began the process of closing the basin, culminating in the collision of the Congo and Kalahari cratons and the formation of the Gondwana supercontinent (Schneider, 2008). The formation of Gondwana included collisional orogenesis which accreted the Damara, Gariep, and Mozambique mobile belts to the stable cratons (Schneider, 2008). This time period spanning from the early Neoproterozoic to the early Cambrian, which included the Damaran Orogen, is called the Pan-African metamorphic event; it was also responsible for large-scale metamorphism of the entire African continent (Schneider, 2008).

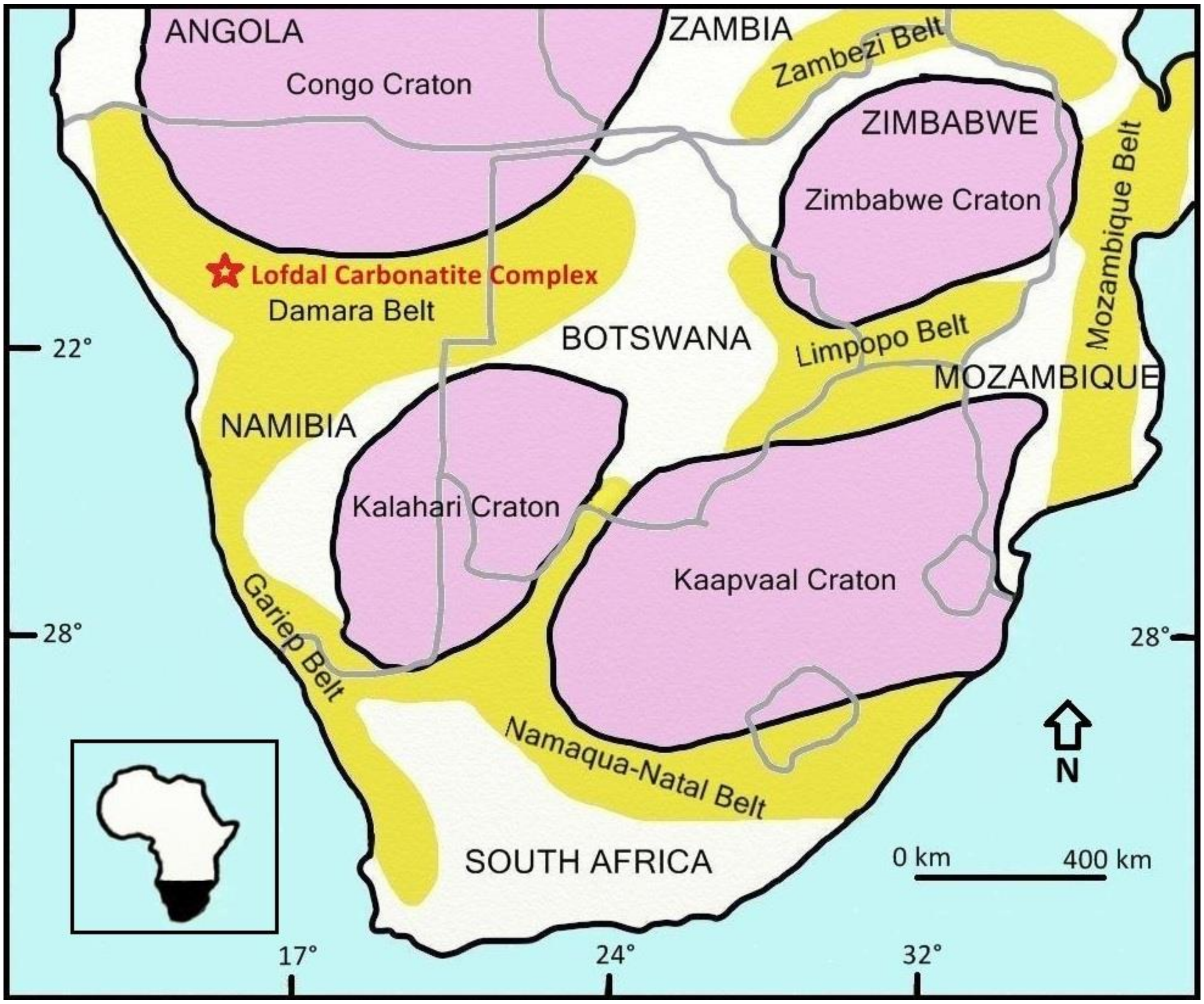

***Figure* 2.1 – Southern Africa is composed of four Archean aged Cratons. These cratons are interconnected by a number of mobile belts formed between the Paleoarchean to the Mesoproterozoic. The Lofdal Carbonatite Complex is located within the Welwitschia Inlier of the Damara Belt, deposited during rifting associated with the break up of Rodinia. (After Schneider, 2008)**

Once established, depression of the Gondwana continental crust induced massive sedimentation which blanketed large portions of the continent from the late Carboniferous to the early Jurassic (Schneider, 2008). After Pangea began to break up around 150 Ma, the modern continent of Afrcia had been stabilized and emerged as it's own plate. Since the break up of Pangea most of the geological activity in Africa has been erosion related sedimentation, to which is owed the Kalari, Karoo, and Namib deserts.

2.2 District Geology of the Welwitschia Inlier, Damara Belt

The southernmost extent of the Congo Craton is exposed at three inliers in the Damara Belt: the Kamenjab, Welwitschia, and Braklaagte inliers (Schneider, 2008). These inliers expose Paleoproterozoic basement rocks of the Congo craton and are structurally overlain by the younger volcanic and sedimentary rocks of the Damaran orogenic suite (Schneider, 2008). The project area of the Lofdal carbonatite complex is located within the Welwitschia Inlier (*Figure 2.2*)

2.3 The Huab Metamorphic Complex

The rocks of the Huab Metamorphic Complex (HMC) comprise the basement of the Welwitschia inlier; they consist mainly of a highly deformed and metamorphosed suite of leucogranitic gneiss, banded paragneiss, quartzite, amphibolite and mica/chlorite schist (*Figure 2.4*) (Frets, 1969). The HMC is interpreted to have originated as a volcano-sedimentary succession and represents the leading edge of the Congo craton in this area (Frets 1969).

2.4 The Damaran Orogenic Suite

The Damaran Orogenic Suite represents a complete *Wilson Cycle* of intracontinental rifting, mid-ocean ridge development, subduction and finally continental collision between the Congo and Kalahari cratons, beginning in the early Neoproterozoic and ending in the early Cambrian (Schneider, 2008). Different volcanic and sedimentary units deposited unconformably atop the HMC are associated with four different stages of this Wilson cycle (*Figure 2.3*).

During the early stages of the breakup of Rodinia (900 Ma), a rift basin developed between the Kalahari and Congo cratons (Schneider, 2008). Sedimentary deposits of quartzite, arkose, conglomerate, phyllite, calc-silicate and limestone (*Figure 2.3A*) were deposited near rift margins (Schneider, 2008). In addition, some local ignimbrites and associated hypabyssal units were intruded between 820 – 730 Ma

(Schneider, 2008). These units are locally assigned to the Nauuwpoort Formation, and collectively incorporated in the Nosib Group sedimentary rocks, and the Nosib Group volcanics (Schneider, 2008).

Beginning around 760 Ma, concurrent with the extrusion of the Nauuwpoort formation, a series of alkali silicate and carbonatitic intrusions were locally emplaced within the Huab metamorphic complex in the Lofdal area, shown in *Figure 2.3A* (Schneider, 2008). These include the Oas quartz-hornblende syenite, and a variety of lithologies assigned to the Lofdal carbonatite complex including nepheline syenites, and carbonatites, each of which will be discussed in *Section 2.5* (Schneider, 2008).

In the mid Neoproterozoic (740 Ma) the rift margin developed into an ocean basin, which brought about a transition in sedimentary deposit types (Schneider, 2008). Clastic and carbonate deposition was dominant during this period along marginal shelf-regions (*Figure 2.3B*). These deposits are referred to as the Swakop group (Schneider, 2008). A number of other interesting units were deposited during this time period, including banded iron formations, schist, basic lavas and even glacial deposits (Schneider, 2008). As the ocean basin continued to grow, it eventually led to the development of a mid-ocean ridge, where submarine basalts erupted (*Figure 2.3C*) (Schneider, 2008).

In the mid to late Neoproterozoic, the extensional regime shifted to a compressional regime as subduction was initiated beneath the Congo craton, eventually leading to continental collision and formation of the Damaran mountain belt (*Figure 2.3D*)(Schneider, 2008). In the mid to late Neoproterozoic (650 Ma) erosion of the Damaran mountain belt began, which resulted in the deposition of shallow marine sandstones, shales and conglomerates, in what is known as the Mulden group (Schneider, 2008).

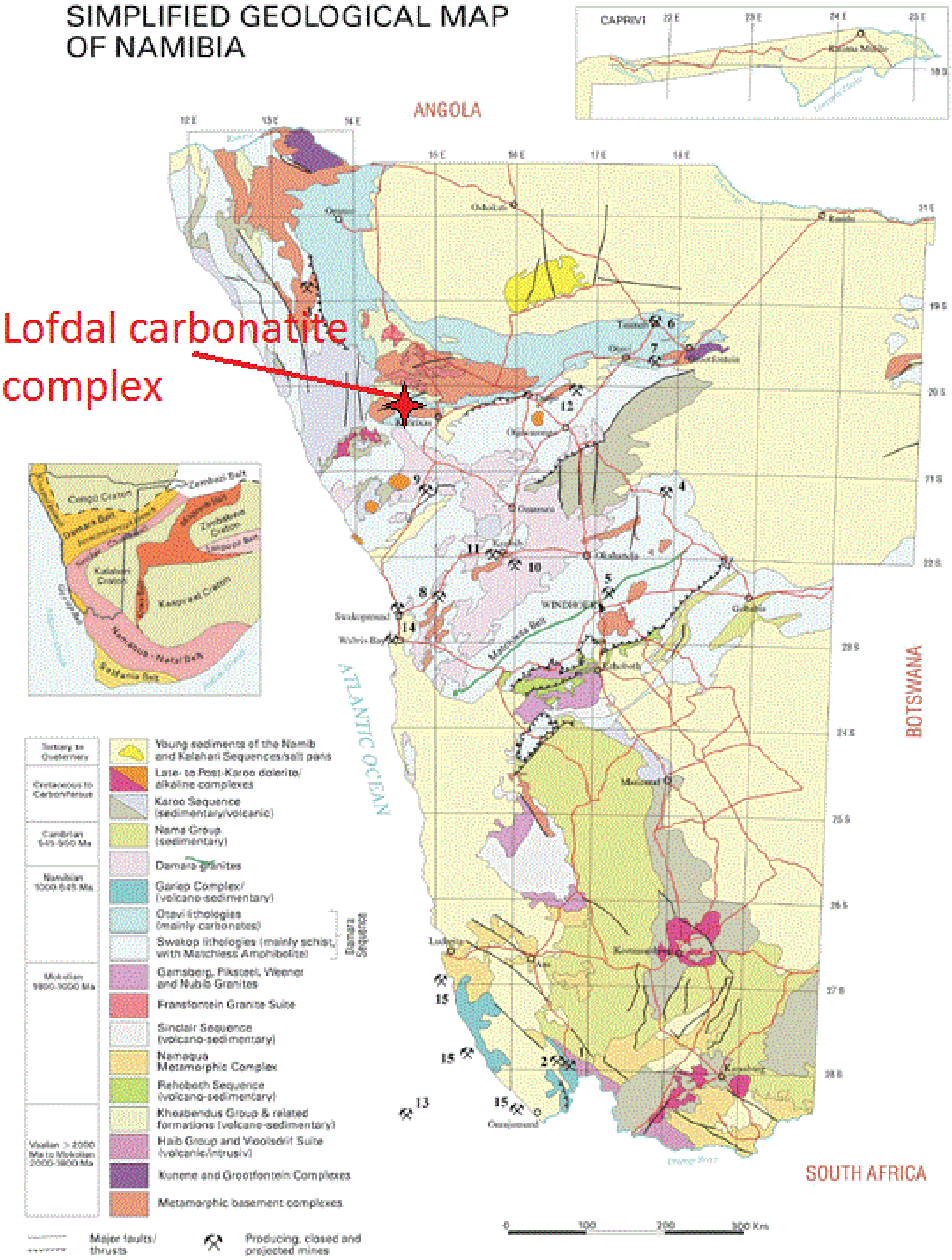

Figure 2.2 – Simplified geological map of Namibia showing the location of the Lofdal carbonatite complex within the Welwitschia inlier (Geological Survey of Namibia, 2002).

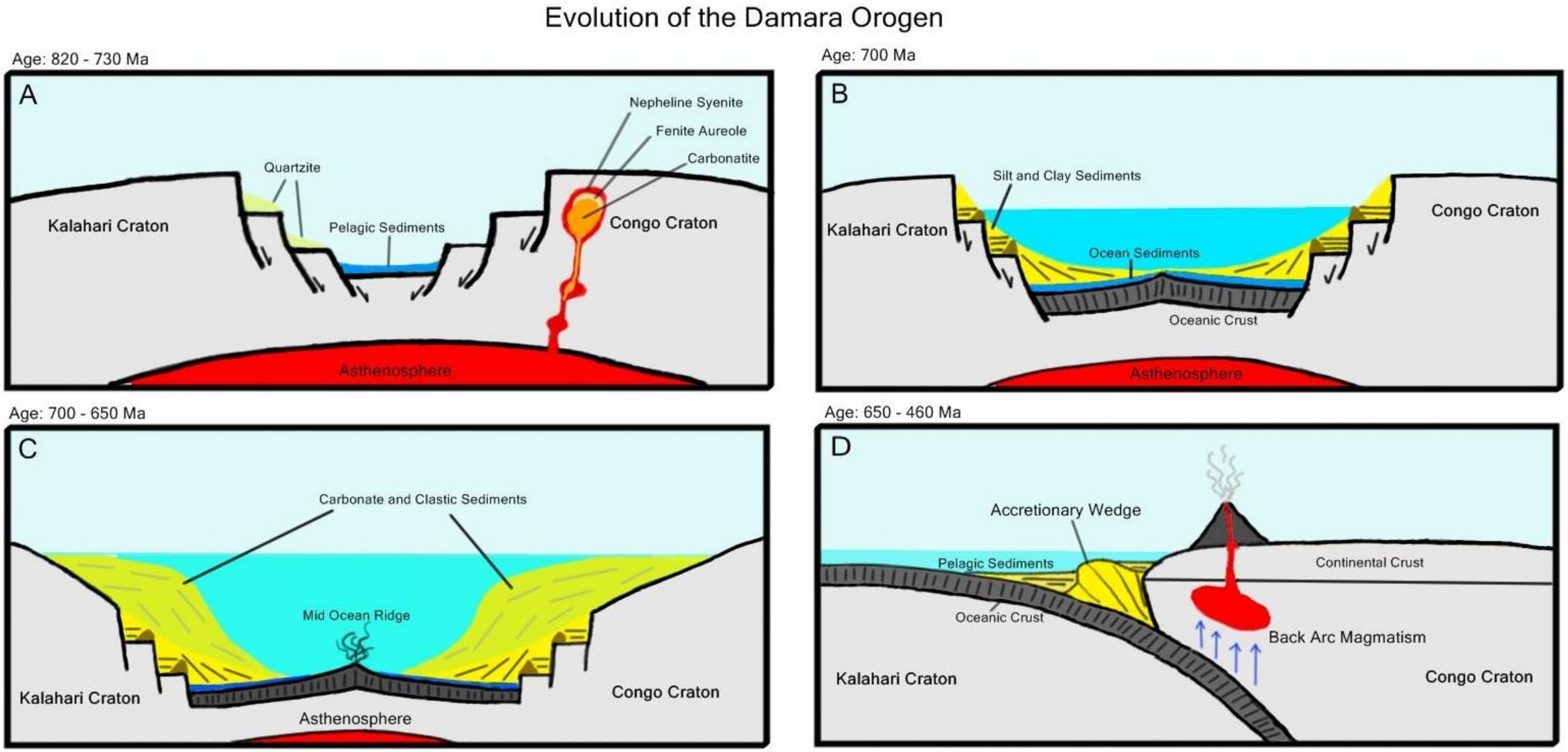

***Figure* 2.3 – The Evolution of the Damara Orogen. (A) Rifting initiated between the Kalahari and Congo cratons, followed by the deposition of sediments, and intrusions of carbonatitic and alkaline silicate bodies. (B) Development of an ocean basin and deposition of shallow marine sediments. (C) Formation of a mid-ocean ridge and eruption of shallow marine basalts. (D) Subduction initiation beneath the Congo craton resulting in closing of the Damaran Ocean basin and Continental collision between the Congo and Kalahari cratons (Image modified after Schneider, 2008).**

2.5 The Lofdal Carbonatite Complex

The Lofdal carbonatite complex (*Figure 2.4*) consists of several nepheline syenite plugs, diatreme breccias, and carbonatite plugs which intrude into the HMC host rocks. These intrusive units are also related to a widespread area of phonolite and carbonatite dyking (over an area of nearly 200 km^2), and hydrothermal alteration (Swinden and Siegfried, 2011). Contact relationships indicate that the intrusion of several plugs of nepheline syenite and phonolite dykes marked the initial stages of magmatism; this was followed by over-pressuring of the syenitic magmas which led to brecciation of syenites and basement rocks of the HMC (Swinden and Siegfried, 2011). The later stages of magmatism involved the intrusion of two plugs of carbonatite into the nepheline syenite bodies; this was accompanied by carbonatite dyking which is found adjacent to or overprinting phonolite dykes (Swinden and Siegfried, 2011). Following the magmatic intrusions, was a period of metasomatic alteration associated with the cooling of the carbonatite magmas, which affected the entire area but is particularly well concentrated along dykes and contact margins between carbonatite and syenite bodies (Swinden and Siegfried, 2011).

2.5.1 Oas Syenite

The Oas Syenite occupies an area of 20 km^2 immediately to the south of the Lofdal project area. It is the largest alkali silicate body associated with the Lofdal silicate/carbonatite intrusive suite. The mineralogy of the Oas Syenite was first described by Frets (1969) as being a dominantly coarse-grained, alkali feldspar, sodium plagioclase, hornblende and quartz syenite with apatite and sphene as important accessory minerals. The Oas syenite has been dated at 757 +/- 2 Ma (Hoffman et al., 1996), and 758 +/- 4 Ma (Jung et al., 2007).

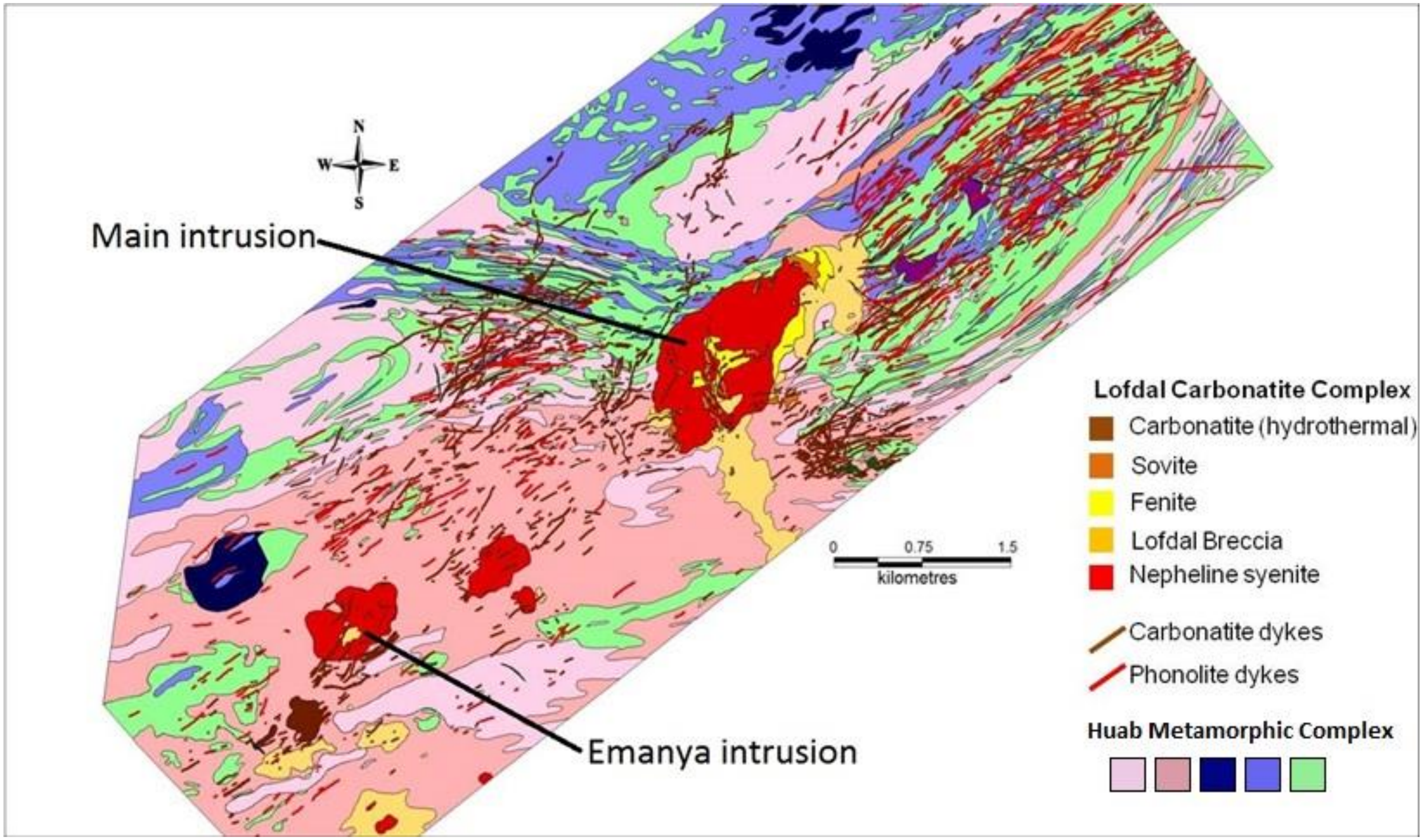

Figure 2.4 – Regional geological map of the Lofdal project area. The Huab complex consists of a highly deformed and metamorphosed suite of leucogranitic gneiss, banded paragneiss, quartzite, amphibolite and mica/chlorite schist, shown by blues, greens and pinks. The Lofdal carbonatite complex includes nepheline syenite and carbonatite plugs, phonolite and carbonatite dykes, fenites, and Lofdal breccias (Namibia Rare Earths, 2011).

2.5.2 Nepheline Syenites

The Main intrusion of the Lofdal Carbonatite Complex was originally mapped by Frets (1969). Recent mapping has shown that there are several other satellite intrusions of nepheline syenite within the project area. These intrusions have been dated using U/Pb in magmatic titanite as 754 +/- 8 Ma (Jung et al., 2007).

The nepheline syenites at Lofdal have been described by O'Connor (2010). Their typical mineralogy includes coarse-grained or interstitial matrix filling alkali feldspar, sericite, biotite plagioclase, and cancrinite, as a pseudomorph replacing nepheline. Some nepheline syenites may include apatite, aegirine, titanite, magnetite, sodalite, fluorite, amphibole, and carbonates.

Cross cutting relationships indicate that the emplacement of these bodies pre-dated dyking, brecciation, and carbonatite intrusion, thus they represent the earliest component of the alkaline magmatic series (Swinden and Siegfried, 2011).

2.5.3 Phonolite dykes

Phonolite dykes, shown in *Figure 2.5A*, are closely spatially associated with carbonatite dykes in the Lofdal complex. They cover an area of approximately 200km^2 and follow a strong northeast-southwest trend (Swinden and Siegfried, 2011). Their mineralogy is described by O'Connor (2010) as 10-15 mm phenocrysts of alkali feldspar, plagioclase, nepheline, cancrinite and sericite in a very fine-grained matrix (of a similar mineral assemblage). Samples may also include aegirine, magnetite, biotite, apatite, sodalite, fluorite, amphibole, and carbonates (O'Connor, 2010). Phonolite at Lofdal is typically undeformed but may be locally sheared (Swinden and Siegfried, 2011). Phonolite dykes are interpreted to have a co-magmatic relationship with the nepheline syenites (Swinden and Siegfried, 2011).

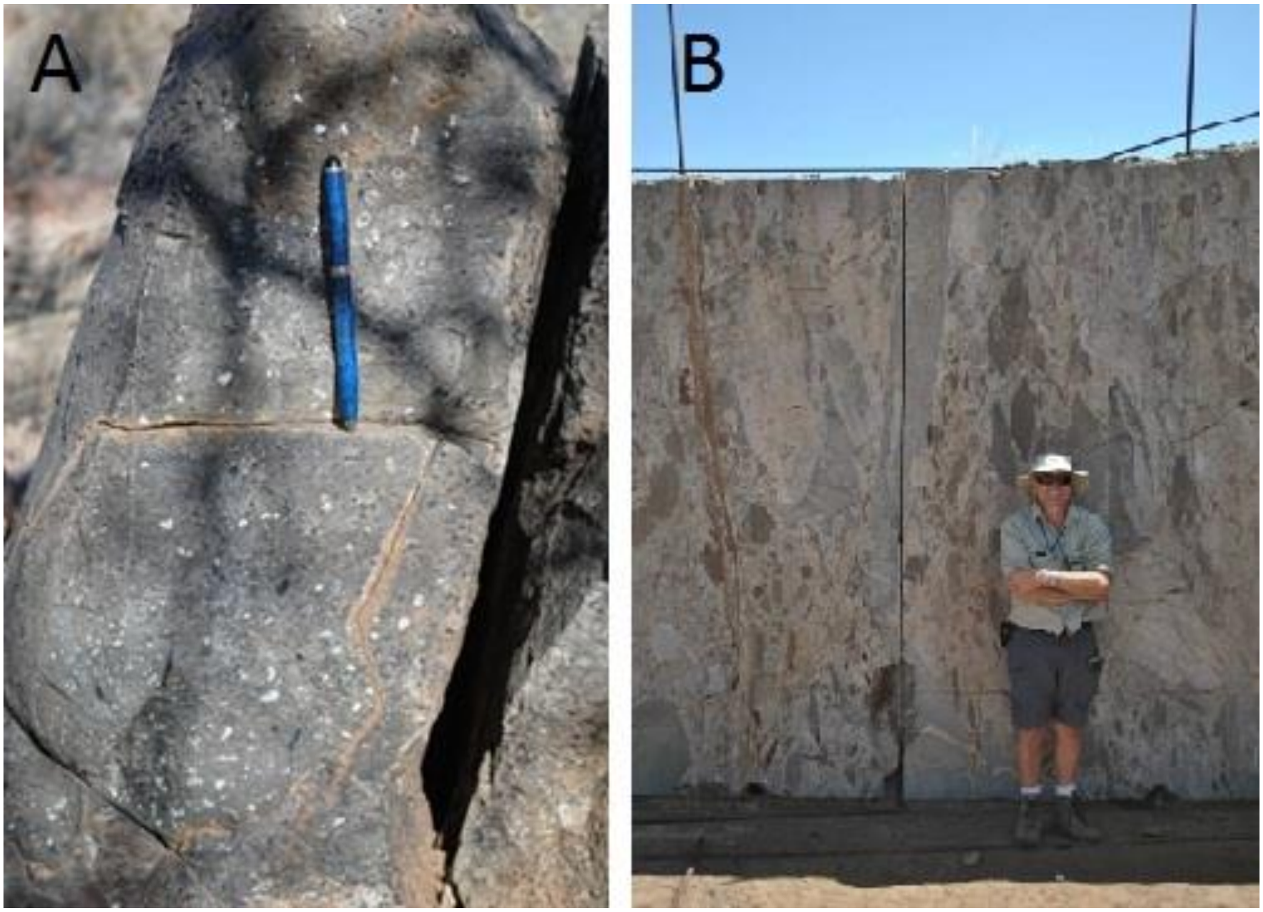

***Figure* 2.5 – (A) Lofdal phonolite dykes. (B) Lofdal breccia (Swinden and Siegfried, 2011).**

2.5.4 Lofdal breccia

Lofdal Breccia, shown in *Figure 2.5B*, is closely associated with syenite and carbonatite intrusive plugs. They are interpreted to have formed through overpressuring of the syenite magma chamber during ascent of the carbonatite magma (Swinden and Siegfried, 2011). Their composition is dominantly HMC country rocks (polylithic breccia) but there are local syenite breccias (monolithic breccia). They are described by Swinden and Siegfried (2011) as being chaotic, poorly sorted and angular.

2.5.5 Carbonatites

Three bodies of carbonatite are present at the Lofdal complex: the Main intrusion, the Emanya intrusion, and the hundreds of carbonatite dykes spread throughout the property (*Figure 2.4*). Each occurrence displays similar mineralogy but quite variable volatile enrichment profiles.

The Emanya intrusion is much smaller than the Main intrusion, with a surface exposure diameter of approximately 350 m. It is surrounded by several smaller satellite plugs of sovite. The Emanya intrusion consists of fine-grained sovite with abundant iron oxides and fluorite-rich veins; it shows relatively strong enrichment in LREE's with almost no HREE enrichment (Swinden and Siegfried, 2011).

The numerous carbonatite dykes in the Lofdal project area show a strong trend of Northeast-strike and steep-south dip, following the structural grain of the basement rocks (Swinden and Siegfried, 2011). They range in size from 10 cm to 10's of meters, and display a variety of discolouration from white and gray, to brown yellow and red (Swinden and Siegfried, 2011). The carbonatite dykes have a very close spatial association with the phonolite dykes and when present in the same dyke, they occur as the later phase of injection (Swinden and Siegfried, 2011). The carbonatite dykes cross cut all other units in the Lofdal complex, including the nepheline syenites, diatreme breccia's and basement rocks of the Huab metamorphic complex. They show good LREE enrichment, and variably strong HREE enrichment (Swinden and Siegfried, 2011).

The Main intrusion is the largest body of carbonatite in the project area (surface exposure 1.5 km^2) and it displays particularly strong uranium and niobium enrichment. Understanding this enrichment, as well as the geological relationships between the carbonatites, fenites and nepheline syenites at the Main intrusion, is the principal focus of this study.

2.5.5.1 The Main intrusion – Previous Work

Sampling and reverse circulation (RC) drilling on the Main intrusion began in 2008, carried out by Namibia Rare Earths (NRE), while attempting to assess the REE potential of the sovite bodies. Approximately 170 grab samples were analyzed for major elements as well as a suite of trace elements which included REE's, uranium, thorium, zircon, and niobium. The analyses returned relatively low REE values, but uranium values were greater than 100 ppm (Swinden, 2012). RC drilling along the Main intrusion produced 5 m composite chip samples; the analysis of which served to complement uranium/niobium enrichment data from the grab sample program. The RC holes demonstrate that mineralization occurs at depth, but provide no structural information about the subsurface.

In 2010, an Airborne Radiometric Survey was conducted over the entire property which identified two significant uranium anomalies at the Main intrusion. This survey was followed up by a 300 m line grab sample collection from outcrops, at 25 m intervals, along the main uranium anomaly. Analyses of these samples averaged 500 ppm uranium and 5000 ppm niobium, with a strong positive correlation between the two values across the sample set (Swinden, 2012).

2.5.5.2 The Main intrusion –Geological Mapping

Recent regional mapping, which included the Main intrusion, was performed by Remote Exploration Services (RES) in early 2011 through outcrop mapping combined with airborne hyperspectral imaging (a high resolution technique which identifies material based on spectral signatures). The study shows that surface exposure at the Main intrusion is dominated by nepheline syenite, while NNW-SSE trending outcrops of sovite correlate with uranium anomalies. A number of smaller bodies of sovite were identified proximal to the intrusive core, a unit of intense fenite alteration was identified (originally mapped as albitite but now considered to be potassic fenite), and the distribution of breccia bodies was better constrained.

Subsequent detailed mapping of the Main intrusion was carried out by NRE in late 2011 to better define the distribution and geological relationships between the different lithologies. The results of this mapping allows for the interpretation of a continuous body of sovite which is overlain by a carapace of nepheline syenite. Contacts between the sovite and overlying nepheline syenite are quite irregular and the presence of subsidiary bodies of carbonatite near the core of the intrusion indicates a high degree of complexity in the subsurface.

2.5.5.3 The Main intrusion – Alteration

As a part of the late 2011 detailed mapping campaign by NRE, two distinct alteration profiles were identified in relation to the carbonatite. These were originally called felsic and mafic fenites, but in accordance with the results of this study, have been re-named and are henceforth referred to as potassic fenite and siliciocarbonatite, respectively (Swinden, 2012).

Potassic fenites occur in the syenite and syenite breccia forming an irregular halo around the carbonatite contact. They are the rocks mapped as “albitites” identified by RES. Although the distribution of potassic fenites reflects their association with the carbonatite-syenite contact margins, they are far less localized than the siliciocarbonatites. This style of fenitization produces a red and rubbly rock which has been almost completely replaced by potassium feldspar (Swinden, 2012). They produce a radioactive signature generally lower than siliciocarbonatites.

Siliciocarbonatites were described as occurring at the syenite-carbonatite contacts within a 2 m buffer zone. Their typical mineralogy is described by Swinden (2012) as very coarse-grained aegirine inter-grown with calcite and microcline. These lithologies produce a strongly elevated radioactive signature. Although originally interpreted by Swinden (2012) as a possible contact alteration phase, these lithologies have been reinterpreted based on the present study as more probably magmatic in origin.

Chapter 3: Methods

In July of 2012, 22 representative end member samples of lithologies that characterize the contact between carbonatite and syenite/syenite breccia (NLOFR8821 – NLOFR8845 including duplicates) were collected from the Main intrusion (*Figure 3.1*). These samples were collected from surface outcrops that were believed to be representative of each of the lithologies in this environment as determined by previous field mapping studies. Two samples were collected at each location; one was submitted for whole rock geochemical analyses, while the other was sent to Dalhousie University for polished thin section preparation.

3.1 Petrography

Preparation of polished thin sections was based on examination of cut surfaces of the collected samples, selecting the most interesting areas. One or two polished thin sections were produced for each sample at the Dalhousie University thin section laboratory operated by Gordon Brown.

Polished thin sections were described using both transmitted and reflected light microscopy, first to identify all rock-forming minerals (RFM's) and subsequently to identify and record all unknown phases for further examination using electron dispersive spectroscopy on the electron probe micro-analyzer at Dalhousie University. Samples were classified based on the rock type. The results of modal mineralogy and accessory mineralogy were provided for each sample. However, individual petrographic descriptions for each sample are not provided. Rather, petrographic descriptions for similar samples are combined to provide overall mineralogical and textural descriptions for each of the sample categories: nepheline syenite, potassic fenite, carbonatite and siliciocarbonatite.

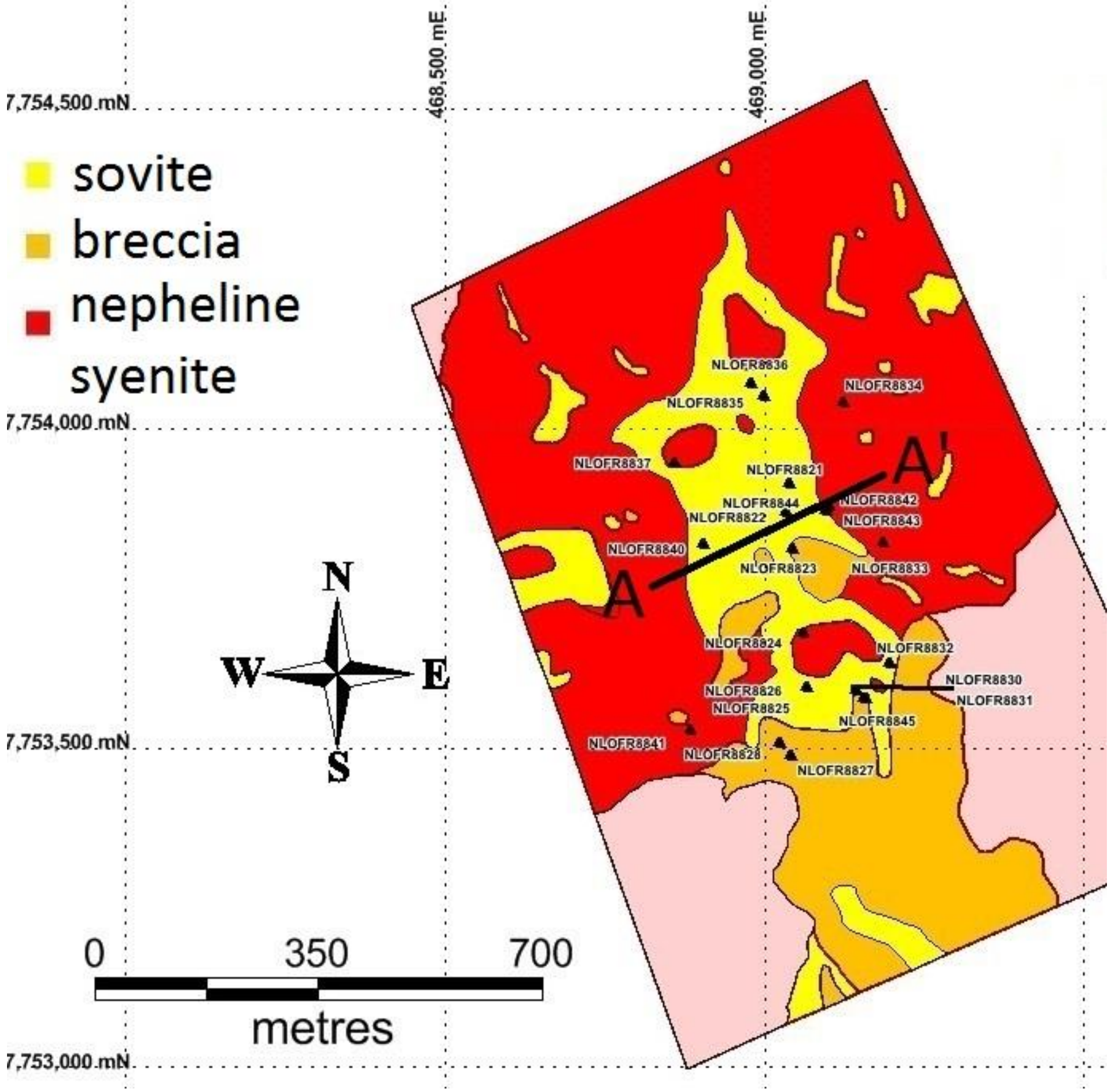

Figure **3.1 – Geological Map of the Main intrusion with sample locations (after Swinden, 2012). The Huab basement gneiss is shown in pink. Cross section A-A' is illustrated in *Figure 5.1*.**

3.2 Mineral Composition Data

Mineral composition data for RFM's and accessory minerals were obtained using energy dispersive spectroscopy (EDS), wavelength dispersive spectroscopy (WDS), and element X-ray compositional mapping, on the JEOL Superprobe (JXA-8200 WD/ED combined microanalyzer) at

Dalhousie University. The JEOL Superprobe was set to run at a beam size 1um with a current of 20 nA. For felsic mineral analyses the following standards were used: sanidine (K, Al, Si), chromite (Cr), jadeite (Na), pyrolusite (Mn), kaersutite (Ca, Ti, Mg), garnet (Fe), and barite (Ba). For pyrochlore analyses the following standards were used: kaersutite (Ca, Ti, Mg), monazite-La (La), monazite-U (U), monazite-Y (Y), monazite-REE (Pr), monazite-Ce (Ce), fluorapatite (F), jadeite (Na), sanidine (Si), monazite-Nd (Nd), magnetite (Fe), tantalite (Ta), monazite-Th (Th), pyrolusite (Mn), columbite (Nb), zirconolite (Zr). EDS was primarily used to confirm petrographic mineral identification, while WDS was used to obtain quantitative mineral data for mineral formula calculation. Element X-ray compositional maps were produced for pyrochlore crystals with oscillatory zoning and growth rims to assist in pyrochlore interpretation.

3.2.1 The Electron Probe Micro-analyzer

The electron probe micro-analyzer (EPMA), shown in *Figure 3.2*, works by bombarding a sample with a focused beam of high energy electrons to produce secondary electrons, backscattered electrons, diffracted backscattered electrons, X-rays, photons, visible light, and heat (Goodge, 2012a). EPMA's are outfitted with advanced detectors which provide precise quantitative analyses of sample phases. In this study, backscattered electrons (BSE's) were used to generate BSE images, allowing sample navigation to perform EDS and WDS analyses. BSE images illustrate minerals on a grey-scale on the basis of their chemical composition. Minerals which are composed of elements with high atomic weights will appear very light gray to white, while minerals composed of elements with low atomic weights will appear medium to dark gray.

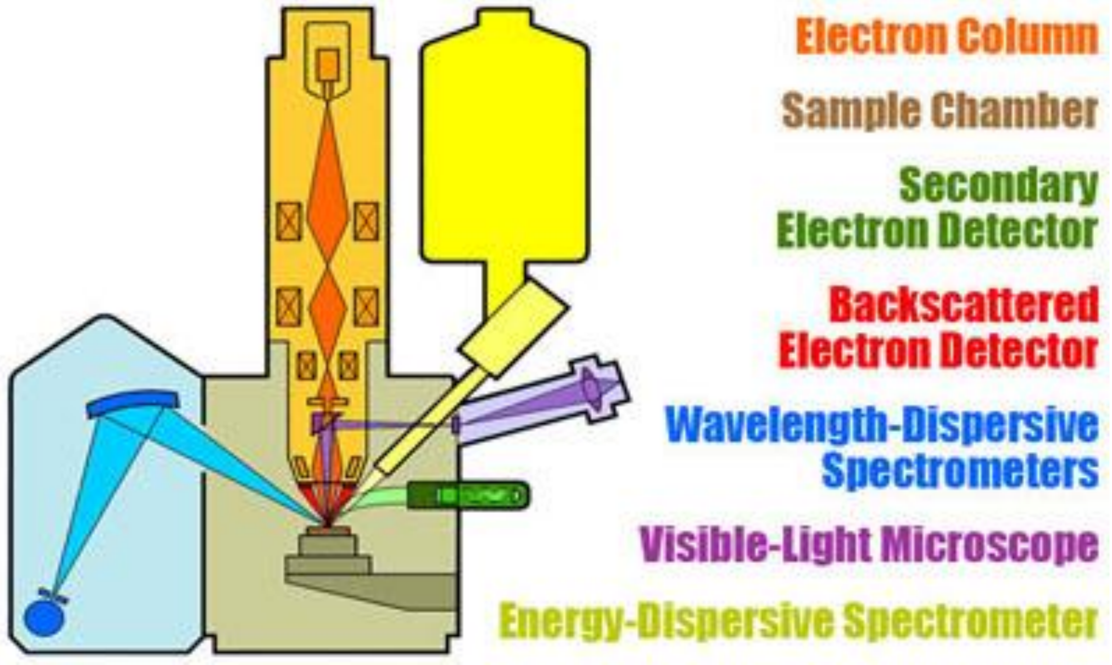

***Figure* 3.2 – An illustration of the various components of an electron probe micro-analyzer (Goodge, 2012b)**

3.2.3 Energy Dispersive Spectroscopy

An EDS system consists of an X-ray detector, a cooling system and software which is used to resolve energy spectrum collected from X-rays produced by electron beam-sample interaction (Goodge, 2012b). X-rays are absorbed by a detector crystal through ionization, which produces an electric voltage. The voltage produced is proportional to the X-ray being absorbed, which means it is diagnostic of a given element. EDS software analyzes these voltages to determine which elements are present in the phase being analyzed, and display a chemical spectrum. EDS detectors can be used in “spot-mode” which will produce a chemical spectrum from a spot analysis in a matter of only seconds. It is therefore a highly useful technique for rapidly identifying phase compositions. There are however, some limitations of EDS analyses. The lightest elements (H, He and LI) cannot be detected by EDS unless the detector is equipped with a polymer-based thin window instead of a Be-window (Goodge, 2012b). Spectrum analysis software used in EDS systems are unable to resolve energy peaks where peak overlap of more than one element may be possible.

3.2.2 Wavelength Dispersive Spectroscopy

A WDS system is similar to an EDS system, but provides much higher precision, and offers much lower detection limits. An EDS system analyzes the relative energy of emitted X-rays, whereas a WDS system will analyze the wavelength and intensity of X-ray emissions. WDS analysis is the preferred method for precise chemical analysis, at the cost of longer analysis times. In order to reduce analysis time, many EMPA's are outfitted with five or six WDS spectrometers which, when used in conjunction, are able to analyze for multiple elements at the same time. A WDS system works by bombarding a crystal surface with a sufficiently high energy beam of electrons, to produce element derived X-rays (Goodge and Henry, 2012). These X-rays are filtered for a specific element of interest using an analytical crystal and application of Bragg's law (Goodge and Henry, 2012). The resulting X-rays that reflect from the analytical crystal will contain one single wavelength, which is passed on to the detector (*Figure 3.3*).

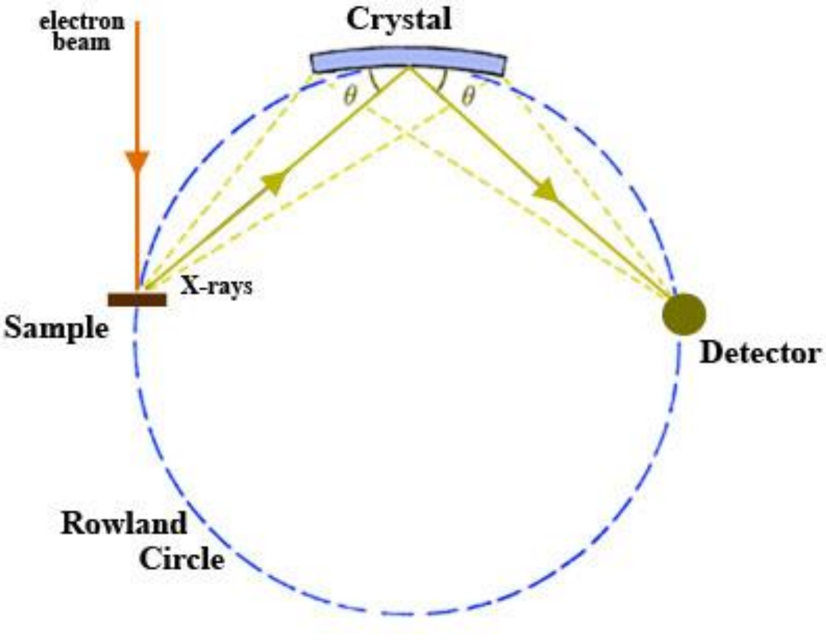

***Figure* 3.3 – Schematic representation of a WDS system. An electron beam bombards the sample producing X-rays characteristic of the elements in a sample. These X-rays are filtered down to X-rays of a single specific wavelength by an analytical crystal and application of Bragg's law. X-rays which reflect off the analytical crystal arrive at the detector to be "counted" (Goodge and Henry, 2012)**

The interaction of X-rays with the analytical crystal is an integral component in WDS analyses. The application of Bragg's law in X-ray- analytical crystal interactions is the key to ensuring that only X-rays of a specified element are reflected to the detector. *Figure 3.4* defines the relationship between the order (n) and wavelength of incident X-rays (λ) which pass through an analytical crystal of known crystal lattice spacing (d) at an incident and diffracted angle (Θ). Diffracted X-rays which are passed on to the detector are the result of constructive interference between scattered X-rays (Goodge et al., 2012). This constructive interference will only occur when the difference in total travel path lengths between rays ABC and A'B'C is an integer multiple (n) of the ray wavelength (λ) (Goodge et al., 2012). In other words, the difference in travel path lengths must be a wavelength multiple which equals 2dsin (Θ). Depending on the element of interest, specific wavelengths which correspond to particular elements of interest may only reach the detector by changing the position of the analytical crystal (Goodge et al., 2012). Additionally, particular analytical crystals are only able to accommodate for a specific range of wavelengths. For this reason, EMPA systems are equipped with between five and six WDS detectors, each with an analytical crystal of variable crystal lattice spacing (d) to accommodate for all possible elements. This same principal it utilized in both X-ray diffraction (XRD) and X-ray fluorescence (XRF) analysis. These two methods utilize incident X-rays of known wavelengths, to determine crystal lattice spacing of a particular sample, to identify the exact mineral structure and composition (Goodge and Henry, 2012).

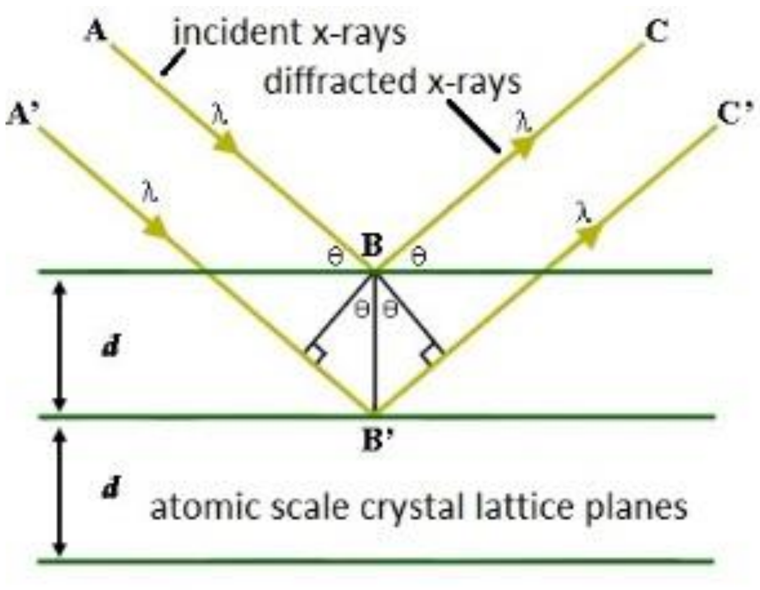

$$n \lambda = 2 d \sin\theta$$

Figure **3.4 – Schematic of the application of Bragg's Law (Goodge et al., 2012)**

X-rays arriving at the detector, pass through a collimator and thin window before moving into a gas-proportional counter chamber. This gas absorbs X-rays and emits a photoelectron that induces an electrical pulse when it comes into contact with a central wire. The amplitude of the electrical signal produced is proportional to the energy of the X-ray which entered the detector. The "intensity" then of this electrical signal corresponds to the abundance of the element of interest, interpreted as a total count. Finally, the count rate is compared to count rates in known standards in order to compute a ZAF correction. ZAF corrections take into account the effects of the atomic number (z), the effects of absorption (A), and the effects of fluorescence (F) through comparison of analysis counts to standard counts. The ZAF correction is applied by WDS system software, which then displays the final analysis results in weight percent oxide for the element suite selected. WDS is the preferred method for crystal chemical analysis, with better peak resolution, and lower detection limits compared to EDS analysis; the trade-off is longer analysis times. Similar limitations exist as in EDS systems, valence states, isotope ratios, and the presence of H, Li and Be are not within the detection capabilities of this analytical technique.

3.2.3 Element Mapping

X-ray composition element mapping is a very powerful technique in imaging compositional zoning and thus chemical distribution. X-ray maps can be made using either EDS or WDS systems, by rastering the electron beam in a grid pattern designed to encompass the entire sample of interest with pixel resolution determined by beam size (Goodge, 2012c). EDS systems are able to produce X-ray composition maps much faster than WDS systems. However, WDS based maps provide higher resolution and lower detection limits. X-ray maps often provide more distribution information than a WDS line traverse, but the information is qualitative not quantitative. Ideally, the combination of X-ray maps overlain with high resolution WDS line traverses will optimize the available information about chemical distribution in a sample.

3.3 Whole Rock Geochemistry

Whole rock geochemical analysis of the NLOFR88xx series samples was arranged by Namibia Rare Earths Ltd. as part of their ongoing geochemical sampling program at Lofdal. Samples were prepared for analysis at the Actlabs laboratory in Windhoek, Namibia. Samples were first crushed in a jaw crusher to obtain 90% passing 2mm, passed through a riffle splitter to obtain a 250g split for pulverization. Splits were pulverized with a swing mill in hardened steel bowls to 95% passing 105 microns. Samples were then homogenized in a stainless steel riffle splitter and a 15g sample was drawn from the splitter for analysis.

Pulp samples were analysed for major element oxides, rare earth elements and trace elements at the Actlabs analytical laboratory in Ancaster, Ontario, using their code 8 REE Assay Package which involves a lithium metaborate fusion and multi-acid digestion. Inductively Coupled Plasma Analyses –

Optical Emission Spectroscopy (ICP – OES) finish was employed for major element oxides, scandium, beryllium, vanadium, strontium, yttrium and zirconium. An ICP-Mass Spectrometry (ICP-MS) finish was used for other trace elements including the rare earth elements. Nb_2O_5 and ZrO_2 were determined by sample fusion and standard XRF methods for samples with >0.3% P_2O_5.

Actlabs demonstrates excellence in quality assurance and quality control, including the analysis of certified reference materials, blanks and duplicates. These QA/QC procedures were monitored be NRE for all sample batches. Additionally, NRE inserts certified reference materials, blanks and laboratory duplicates each at a frequency of 5% into sample batches prior to submission to Actlabs. NRE also submitted 5% of the total samples to ALS laboratories in North Vancouver as an additional check on data quality. All QAQC data for samples analysed with the present sample set were within tolerances and the geochemical analyses of these samples are considered to be of appropriate quality for use in this study.

Chapter 4: Results

4.1 Petrography

Samples from the Lofdal carbonatite complex are classified in four rock types: nepheline syenite, potassic fenite, carbonatite and siliciocarbonatite. A comprehensive table of modal mineralogy (modal %) and accessory mineralogy of each sample, classified by rock type, can be found in *Appendix C*. This section presents a combined summary of typical minerals and textures for each rock type, not specific to any one sample. During the course of petrographic analysis, any minerals that were considered too ambiguous to be determined optically were determined compositionally using electron dispersive spectroscopy. As a caution to the reader, many of the polished thin sections used in this study were 2-3x thicker than the usual 30um. As a result, most of the XPL *Figure*s in the following sections will show mineral birefringence colours 2-3 orders of magnitude higher than normal.

4.1.1 Nepheline Syenites

Samples of nepheline syenite include: NLOFR8832, NLOFR8834, and NLOFR8841 (*Appendix C)*. In hand sample, these rocks are medium gray to brownish gray on the weathered surface, and medium to light gray on the fresh surface. The typical mineralogy includes: coarse-grained potassium feldspar, with lesser albite, nepheline, cancrinite, biotite, and magnetite, and trace amounts of apatite, calcite, zircon and very rare pyrochlore (*Figure 4.1*).

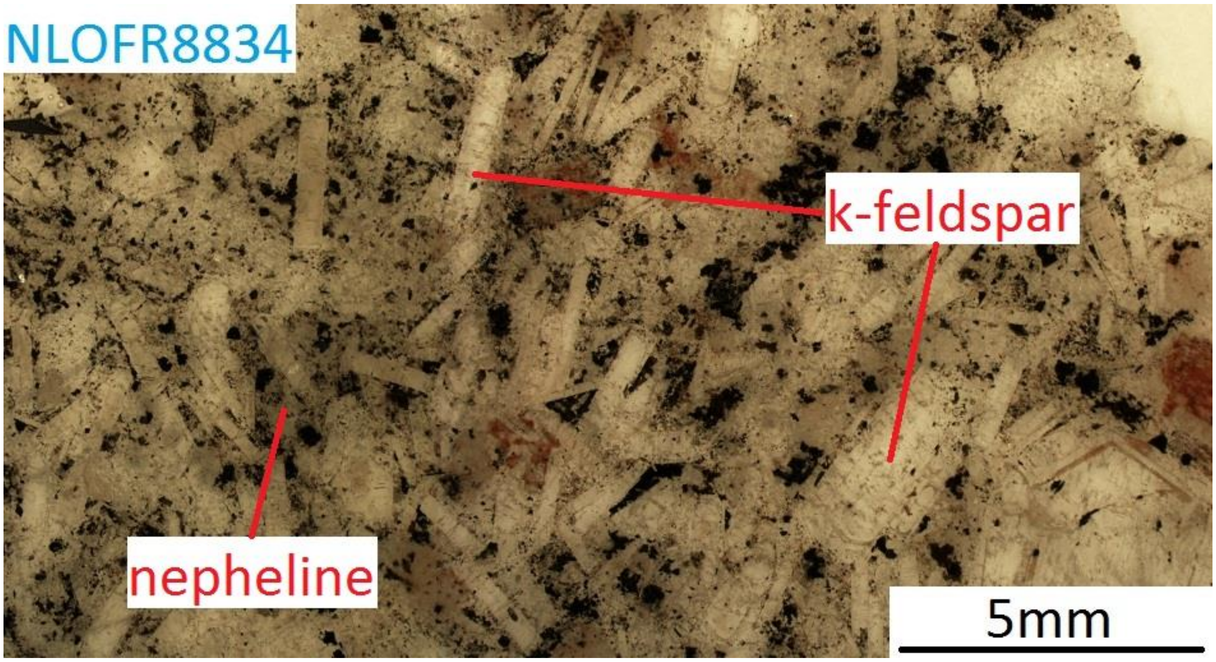

Figure **4.1 – Porphyritic potassium feldspar and nepheline in a matrix of mainly cancrinite with subsidiary biotite and magnetite.**

Feldspars in these rocks constitute approximately 30% - 40% of the modal mineral percentage, with an estimated 5% margin of error. The most abundant feldspar is microcline, accounting for about 25-35% of the modal mineral percentage, with grain sizes ranging from 1 to 3 mm and showing either subhedral or euhedral crystal shape. In plane polarized light (PPL), they display a dirty brownish-gray colour, a common characteristic of these minerals throughout the sample suite. The less common variety (1% modally) of potassium feldspar is orthoclase, occurring as 1-2 mm crystals with anhedral crystal shape, but commonly displaying simple twinning. Albite is present in these samples as a perthitic exsolution in potassium feldspar, but also as euhedral grains approximately 1 mm in size. Albite accounts for approximately 5% of the modal percentage.

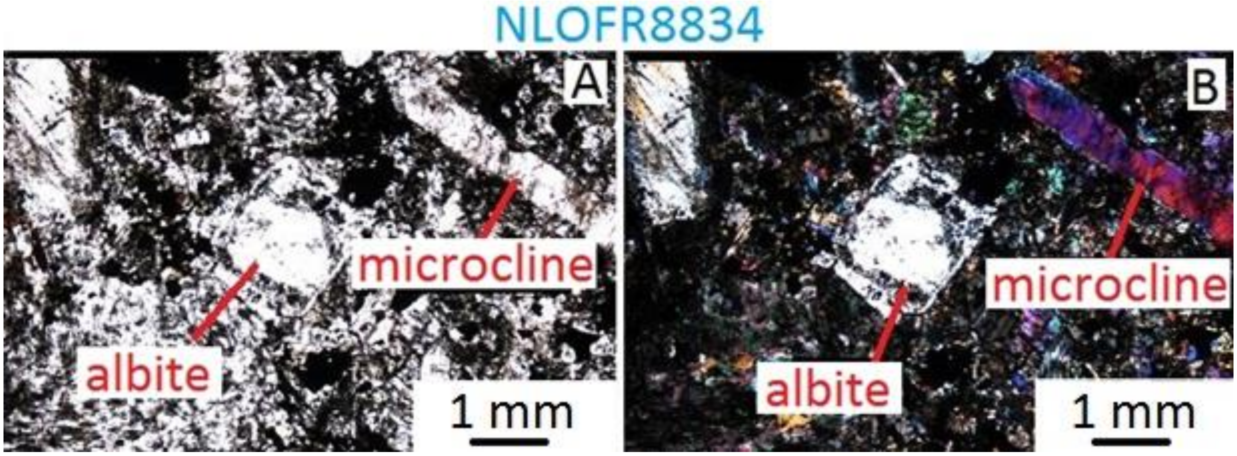

***Figure* 4.2 – Sample NLOFR8834 showing microcline, orthoclase, and albite. (A) Albite and microcline in a matrix composed of mainly cancrinite with minor nepheline (PPL). (B) Image A in cross-polarized light.**

Nepheline and its alteration product cancrinite, account for between 35% and 50% modally, with cancrinite accounting for between 30% and 40%. Nepheline is anhedral, with approximately 1 mm grain sizes, and in PPL it is fairly white, highly fractured, and very cloudy looking (*Figure4.3 A*). In some areas, the outline of an originally euhedral nepheline grain can be identified by the euhedral faces of the remaining anhedral fragments. **Cancrinite** occurs as very fine-grained anhedral masses, more heavily concentrated around nepheline grains, but occurring throughout the sample surrounding the larger feldspars (*Figure 4.3 B*). In PPL it is colourless, and in cross polarized light (XPL) it shows anomalous interference with no visible extinction.

Biotite in these samples accounts for approximately 1% - 8% modally, with a grain size of approximately 0.5 mm and typically an anhedral crystal shape. Light brown to dark brown pleochroism and good cleavage in one direction are characteristic. These grains typically contain inclusions of euhedral to subhedral magnetite (*Figure 4.4*); magnetite is also commonly seen along the edges of the grain.

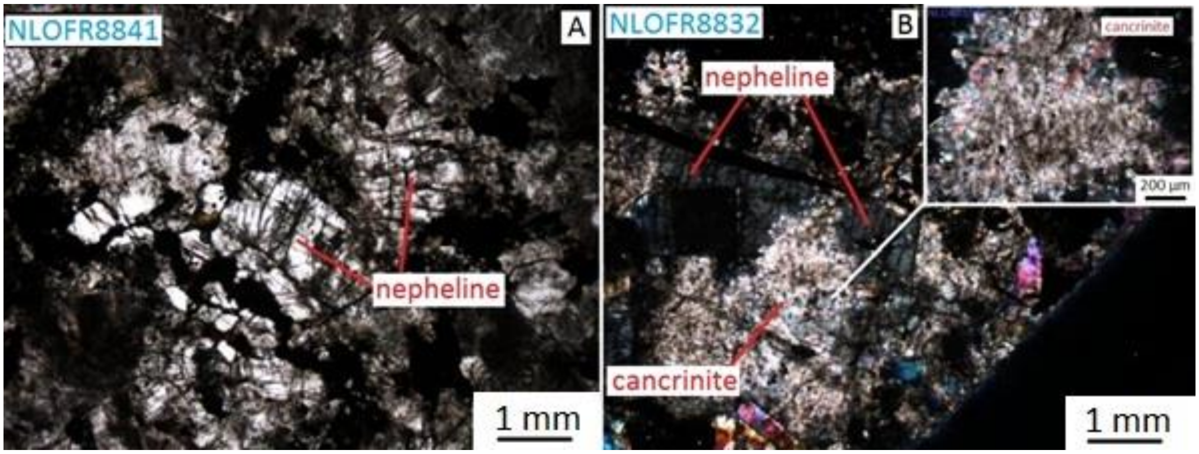

***Figure* 4.3 – (A) White-cloudy nepheline in PPL. (B) Nepheline extinct in XPL, surrounding by a fine grained matrix of cancrinite'. Also visible (top right corner) is a higher magnification image of the massive cancrinite.**

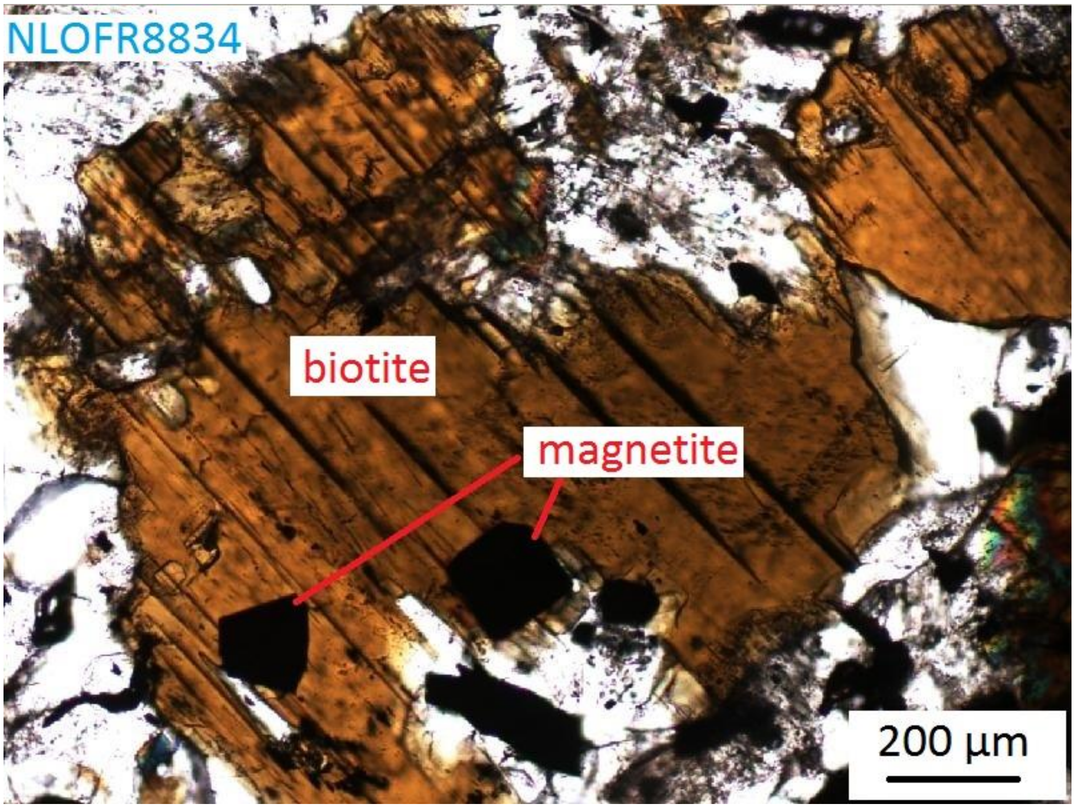

***Figure* 4.4 – Sample NLOFR8834 shows anhedral biotite with good cleavage in one direction, with inclusions of magnetite.**

Magnetite accounts for 3% - 5% modally, occurring as 0.5 mm subhedral and rare euhedral grains, with common inclusions and/or exsolution of hematite (*Figure 4.5 B*). Similarly, zircon occurs in trace quantities as anhedral grains (<0.1 mm) and may contain inclusions of a niobium-rich iron oxide, possibly Fe-columbite. **Apatite** is present in trace quantities, occurring as <0.5 mm anhedral to subhedral single crystals. Rare crystals of **pyrochlore** have also been identified within these samples (*Figure 4.5 A*), occurring as <0.1 mm highly altered grains with some euhedral crystal faces, showing strong compositional zoning. These grains are observed to occur with spatially associated carbonate, albite, magnetite and zircon.

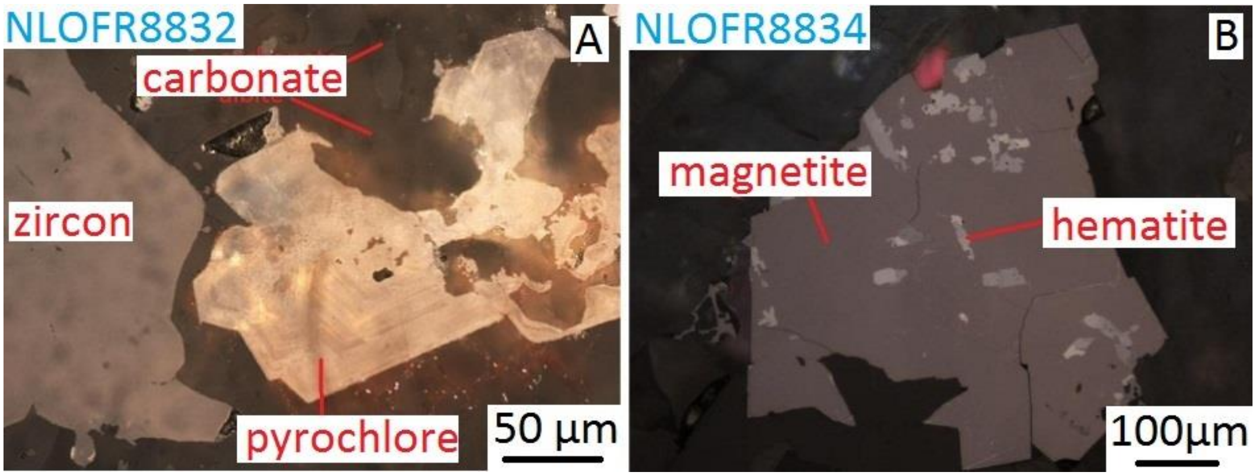

***Figure* 4.5 – (A) Oscillatory zoned pyrochlore next to zircon in a matrix of fine-grained albite and carbonate. (B) Magnetite grains, with inclusions and at times exsolution of hematite.**

4.1.2 Carbonatites

Carbonatite samples in this section are classified as either carbonatite, or siliciocarbonatite. The first refers to carbonatite samples which meet the IUGS classification criteria that samples contain more than 50% carbonate minerals. Siliciocarbonatite refers to samples which contain appreciable quantities of additional minerals including sodic-pyroxene, phosphates, and feldspars; these samples generally have between 10 and 35 wt% SiO_2. It is important to note that siliciocarbonatites are interpreted to have a magmatic origin, and are different from sodic or potassic fenite samples which may have up to 10% carbonate minerals modally, and a metasomatic origin.

4.1.2.1 Carbonatite

Samples which are classified as carbonatite include: NLOFR8822, NLOFR8827, NLOFR8831, NLOFR8837 and NLOFR8842. In hand sample on the weathered surface, these rocks are white with grayish pink and green patches, and often have a reddish brown rusty colour due to fracturing and staining. They may either be medium-grained or fine-grained, with a granular texture (*Figure 4.6*). Some samples contain appreciable amounts of linear bands of fine-grained sulfide, while others contain "bands" of aegirine. On the fresh surface, these rocks appear much whiter, and the sulfide-silicate banding is easily distinguishable. The typical mineralogy of these samples is dominantly calcite (NLOFR8822 is mostly dolomite), along with minor quantities of apatite, aegirine (rare riebeckite), magnetite, trace feldspars, and rare pyrochlore. Sample NLOFR8831 is the only sample that contains a significant amount of sulfide mineralization, including chalcopyrite, pyrite, and pyrrhotite.

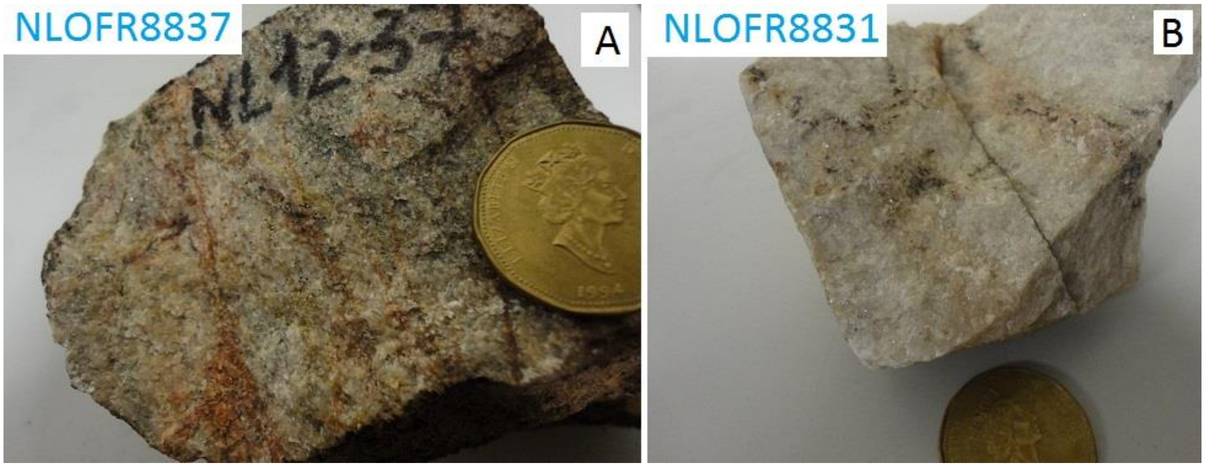

***Figure* 4.6 – Hand sample speciments of carbonatite: (A) Sample 37 shows characteristic fracturing and staining, (B) Sample 31 shows very white colour with good sulfidation,**

Almost all of the carbonate in these samples is calcite, with the exception of sample NLOFR8822 which is almost pure dolomite. **Calcite** accounts for between 90-95% of the modal mineralogy of these samples. It is typically anhedral, fine to medium-grained, and occurs in equigranular masses (*Figure 4.7*). It is also found occurring as inclusions in aegirine. Additionally, in the proximity of any other silicate minerals, the grain size becomes much smaller.

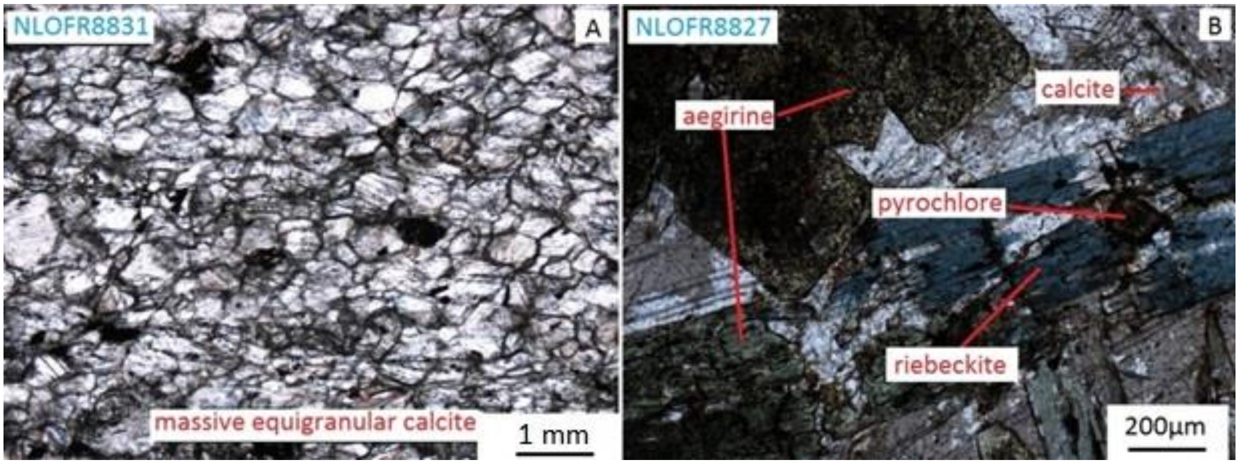

***Figure* 4.7 – (A) equigranular massive calcite with mixed sulfides. (B) Subhedral aegirine, partly altered to riebeckite, with an inclusion of pyrochlore, all hosted in calcite.**

Aegirine accounts for between 3 and 10% of the modal mineralogy in carbonatite samples. It is typically very fine-grained <1 mm, especially when compared with the much coarser aegirine grains found in the siliciocarbonatite. It shows variable iron content as its pleochroism varies between a dark to medium green, and a lighter greenish brown colour in iron poor varieties. It generally has a subhedral to euhedral crystal shape, and contains abundant inclusions of mainly calcite, but also minor apatite and quartz. In sample NLOFR8827, aegirine is altered to **riebeckite**, a more hydrous and slightly less sodic mineral, with light to medium blue pleochroism (*Figure 4.7*).

Both **K-feldspar** and **apatite** are present in these samples, accounting for around 2% modally. Commonly the two occur in a single grain, and while some grains appear to show albite rims on Kfeldspar, most often the texture is insufficient to suggest replacement. Crystals are commonly 1-2 mm, with anhedral crystal shape, and usually occurring in small clusters of two or three grains. Both feldspars show similar PPL-colour compared to nepheline syenites. The potassium feldspars appear very dirty or cloudy with a grayish colour, while albites tend to be much whiter.

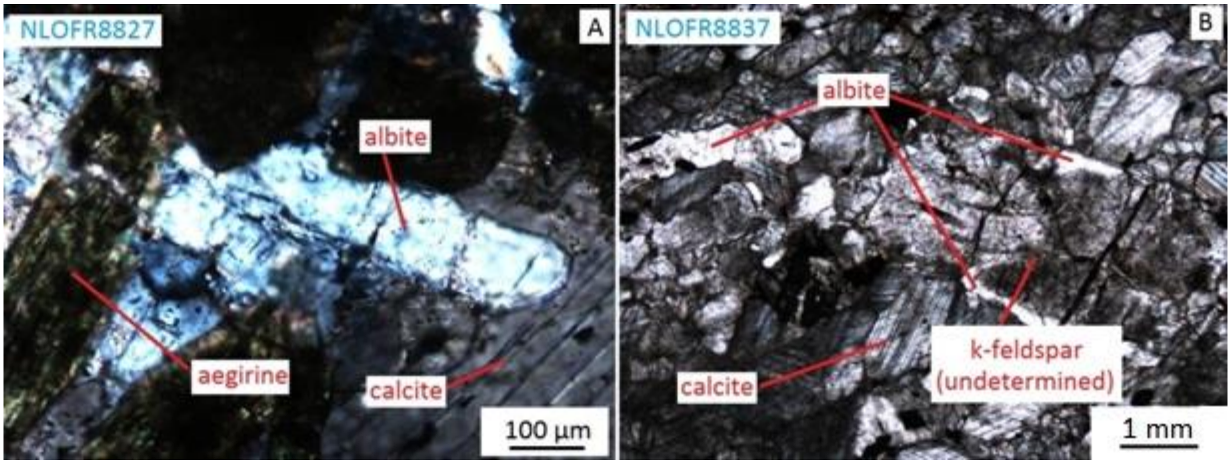

***Figure* 4.8 – (A) Aegirine and apatite (with diagnostic crystal shape) hosted in calcite. (B) Coarse grain of K-feldspar with albite rims, adjacent to an albite grain, both hosted in calcite.**

The accessory minerals in these carbonatite samples account for between 5 and 10% modally. Apatite is very fine-grained <0.5 mm, and subhedral, with elongate diagnostic crystal shape, but poorly defined crystal faces. It is most commonly found spatially associated with aegirine rich “bands”. This spatial association with aegirine applies to **pyrochlore** occurrences as well. They are observed in sample NLOFR8827 as both inclusions in, and situated next to aegirine grains. The pyrochlores have subhedral and sometimes euhedral crystal shape, metamict texture, and well defined oscillatory zoning. They are dark brown to nearly opaque in PPL, with a grain size of <0.5 mm. In cross-polarized reflected light they show characteristic abundant yellow internal reflections.

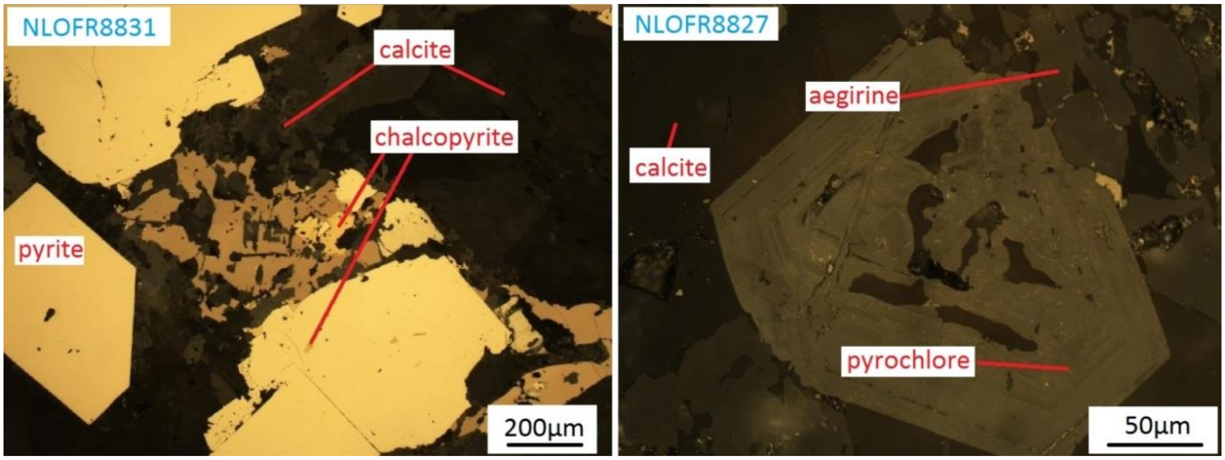

***Figure* 4.9 – (A) Pyrite and pyrrhotite which share mutual grain boundaries, and host inclusions of chalcopyrite. (B) Pyrochlore in reflected light XPL with yellow IR, hosted in calcite and aegirine.**

Sulfide minerals are abundant in NLOFR8831, with **pyrite** occurring in trace quantities in other carbonatite samples. These sulfides generally appear to form very thin veins through the carbonatite. Pyrite has euhedral crystal shape with diagnostic medium reflectance and no anisotropy, with inclusions of mainly **chalcopyrite**. **Pyrrhotite** is anhedral, riddled with inclusions of silica and chalcopyrite, and rare inclusions of barite and celestine, which cannot be seen optically. The pyrite and pyrrhotite show mutual grain boundaries, indicating synchronous growth.

4.1.2.2 Siliciocarbonatite

Samples of siliciocarbonatite include: NLOFR8825b, NLOFR8826, NLOFR8843, NLOFR8844, and NLOFR8845. In hand sample on the weathered surface, these rocks have a reddish brown to pink colour. On the fresh surface they are characteristically whitish pink and green with patches of coarse-grained aegirine, calcite, feldspar and clusters of apatite, and magnetite, with lesser phlogopite and pyrochlore (*Figure 4.10*)

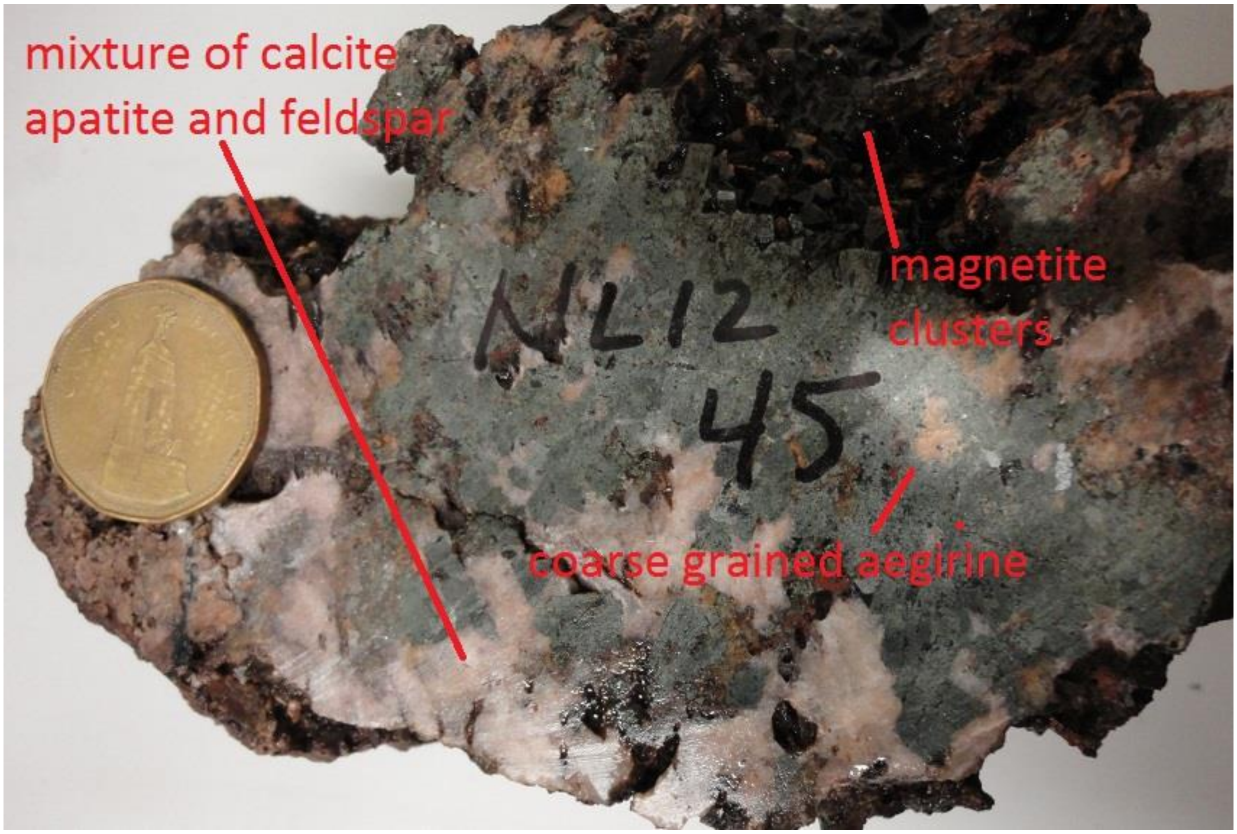

Figure **4.10 – Pegmatitic siliciocarbonatite with coarse-grained aegirine and massive calcite and feldspar, with clusters of apatite and magnetite**

Aegirine accounts for between 20 and 30% of the modal mineralogy. It is typically coarse-grained (2-3 mm) with subhedral to euhedral crystal shape and often has abundant inclusions of very fine-grained carbonate (*Figure 4.11*). Aegirine in sample NLOFR8845 shows very minor hydrous alteration to **riebeckite** (<1% modally).

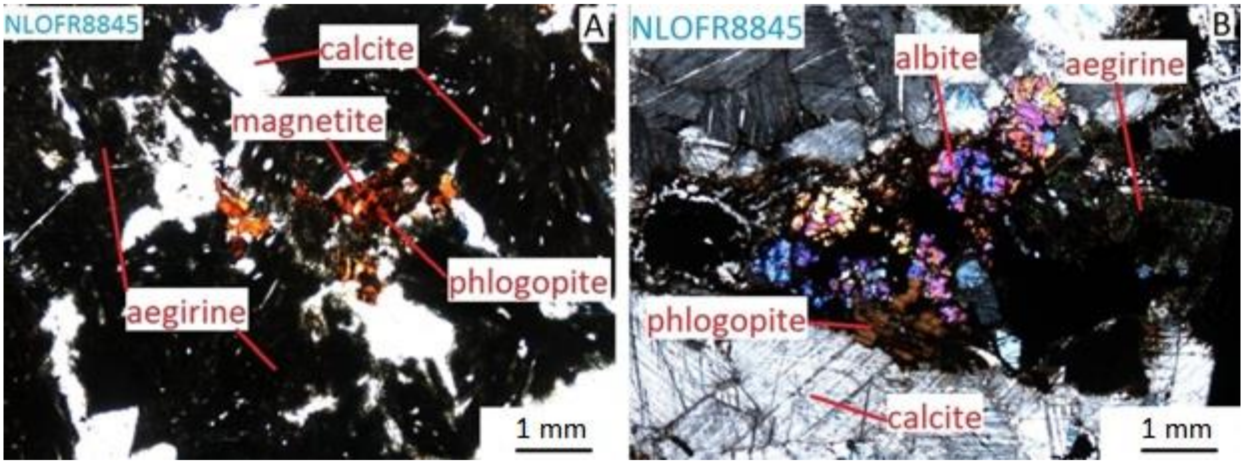

***Figure* 4.11 – (A) Coarse-grained aegirine and calcite, with phlogopite and associated magnetite (PPL). Aegirine shows abundant inclusions of carbonate. (B) coarse-grained equigranular calcite with a cluster of aegirine, phlogopite and albite (XPL).**

Calcite is the only carbonate mineral in the siliciocarbonatite samples. It accounts for approximately 15-35% of the modal mineralogy. Crystals occur as equigranular masses that are typically subhedral, medium-grained (2-3 mm), with visible 60°-120° cleavage. Similarly to aegirine, calcite tends to occur in clusters rather than sporadically.

Apatite is abundant in these samples, accounting for between 10 and 25% modally. It occurs as both euhedral inclusions in medium-grained calcite (*Figure 4.12A*), and as subhedral aggregates 5-10 mm across (*Figure 4.12B*). Apatite crystals which occur as inclusions in calcite are typically much smaller than those which occur in aggregates.

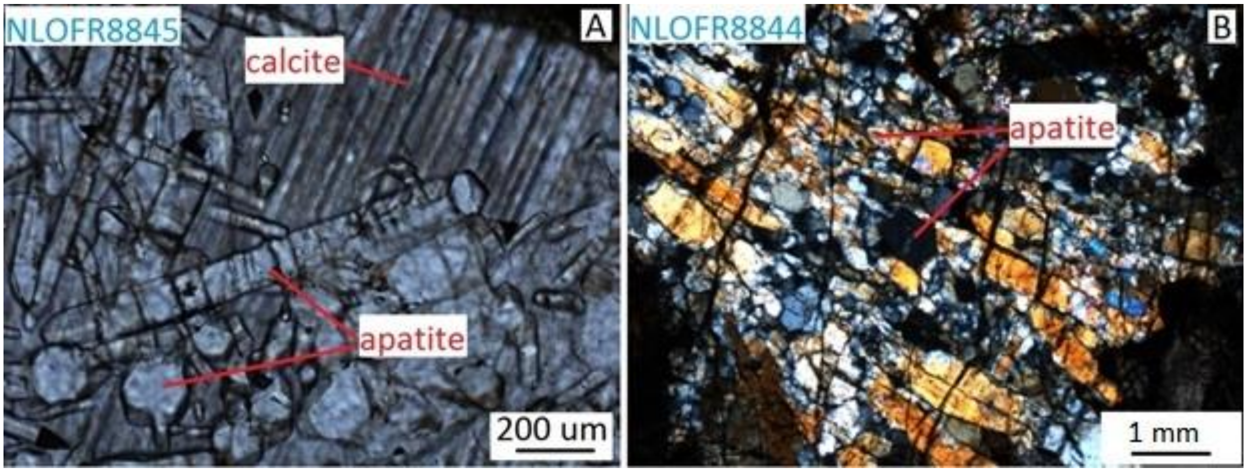

***Figure* 4.12 (A) euhedral apatites as inclusions in calcite (PPL). (B) subhedral aggregate clusters of apatite (XPL). Clusters measure approximately 5-10mm across**

Both **albite** and **orthoclase** are present in some of these samples, accounting for approximately 20% modally. Orthoclase grains are very coarse, 5-8 mm in length, and have subhedral crystal shape commonly with interstitial medium-grained calcite. Albite is commonly anhedral and fine-grained (<1 mm) occurring in clusters associated with phlogopite and aegirine.

Accessory minerals include **phlogopite**, **magnetite** and **pyrochlore**. Both phlogopite and magnetite occur associated with these clusters of feldspar grains (*Figure 4.13 A,B*). Phlogopite contains abundant inclusions of magnetite, as well as magnetite rims. It generally shows anhedral crystal shape and light to medium brown pleochroism. Cleavage in one direction is visible in some specimens. Magnetite is very abundant in these samples and tends to occur in massive clusters of euhedral 2 mm wide crystals (*Figure 4.10*). Pyrochlore, while still occurring in minor quantities, is fairly abundant in these samples. Pyrochlore shows euhedral to subhedral crystal shape, ranging in grain size from 0.2 mm – 1 mm, and zoning is not a characteristic feature of these specimens. Two general compositions are evident (*Figure 4.13 A,B*). The first type of pyrochlore (*Figure 4.13A*) shows an inner grain of euhedral oscillatory zoned pyrochlore, with an outer rim composition with syneresis cracks and a metamict texture. The contact between the outer and inner grains appears smooth and parallel to the inner crystal face with little evidence of dissolution. The second type of pyrochlore (*Figure 4.13B*) shows a euhdral pyrochlore grain with dissolution texture in the inner crystal. The inner portions of the crystal show fractures, and the contact between the two compositions is highly irregular.

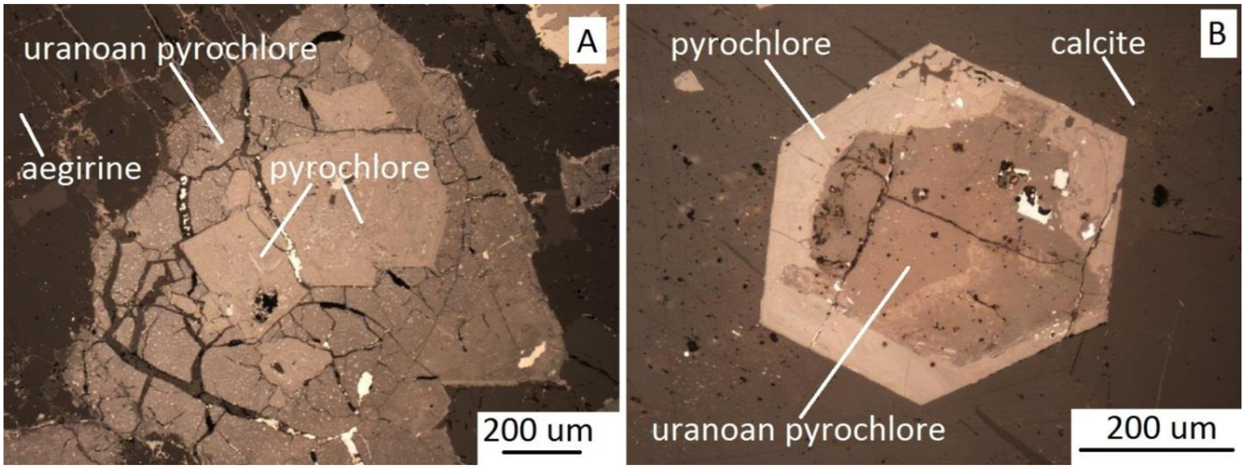

***Figure* 4.13 – (A) Inner euhedral oscillatory zoned pyrochlore with a large outer growth rim characterized by syneresis cracks and a metamict texture (reflected light PPL). (B) Euhedral pyrochlore which shows dissolution texture within the inner potions of the crystal along irregular contacts (reflected light PPL).**

4.1.3 Potassic Fenites

Samples of potassic fenite include: NLOFR8821, NLOFR8823, NLOFR8824, NLOFR8825a, NLOFR8828, NLOFR8830 and NLOFR8835. These samples are characterized by an almost complete recrystallization to potassium feldspar, most commonly microcline. In many samples a pseudo trachytic texture is predominant, displayed by the parallel alignment of microcline (*Figure 4.16*). The general mineralogy of these samples includes microcline, with lesser albite, orthoclase, calcite, aegirine, magnetite, pyrolusite, zircon, zirconolite, titanite, ilmenite, pyrochlore and trace ferrocolumbite. In hand sample these rocks commonly show an intensely weathered rind, with only coarse potassium feldspar crystals remaining, that persists 1-2 cm into the sample. On the weathered surface they are pink and brown with visible coarse-grained feldspar, while on the fresh surface they are whitish gray and pink (*Figure 4.16*).

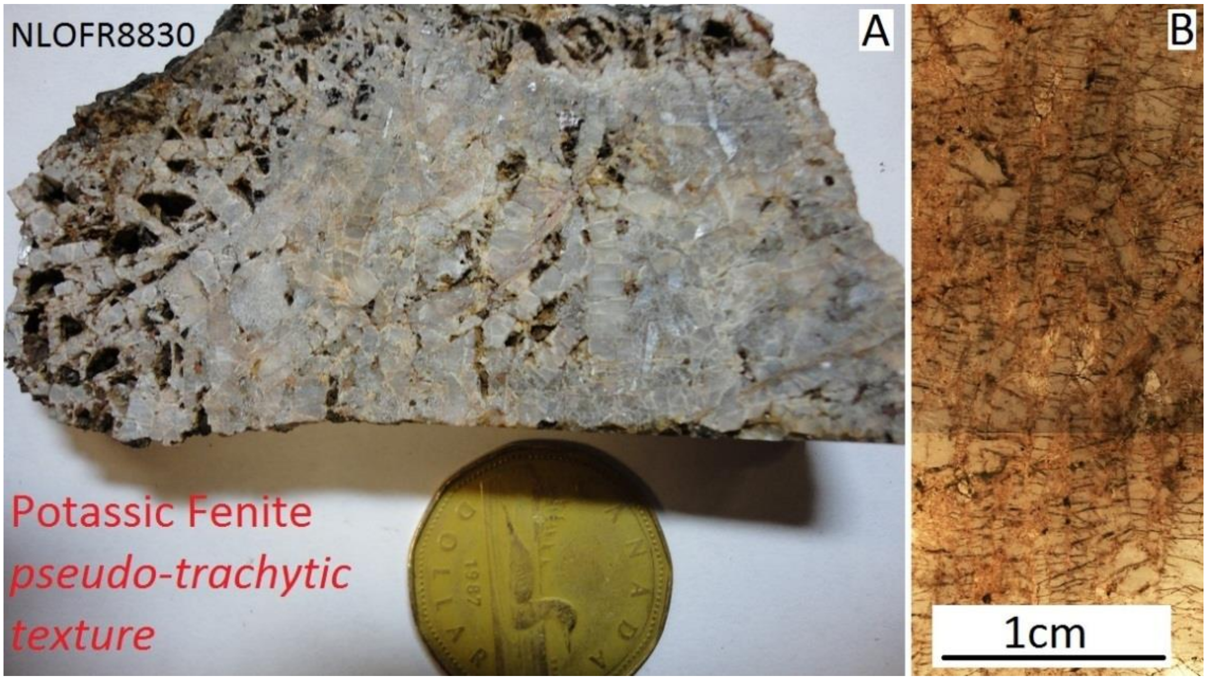

***Figure* 4.14 – (A) Potassic Fenite dominantly composed of aligned potassium feldspar crystals displaying pseudo trachytic texture. (B) Slightly enlarged high contrast image to better illustrate texture**

Feldspar in these samples ranges in grain size from 1 to 3 mm with subhedral to euhedral crystal shape. Crystals typically show a preferred parallel orientation (*Figure 4.16 B*), although a slightly more chaotic alignment is also observed (*Figure 4.16 A*). Some samples show potassium feldspar grains which are offset slightly along a fracture plane, which appears to offset the potassium feldspar crystals as well as the aergirine, carbonate and albite veins which cross-cut the feldspars (*Figure 4.17 A*). Albite is far less common in these samples, and usually occurs associated with fractures and may result as a sodic alteration of potassium feldspar (*Figure 4.17 B*).

Aegirine and **calcite** both occur within fractures, and as fine-grained (~1 mm) crystals. The larger aegirine crystals are anhedral, with a grain size of approximately 1mm. They are interconnected by smaller aegirine filled fractures and appear to show an interstitial texture, with grain boundaries controlled by the surrounding potassium feldspar (*Figure 4.17 C*). Similarly, the larger anhedral calcite crystals, also with an approximately 1 mm grain size, show an interstitial growth texture controlled by the surrounding potassium feldspar crystals. These calcite crystals appear heavily stained brown along visible cleavage planes (*Figure 4.17 D*).

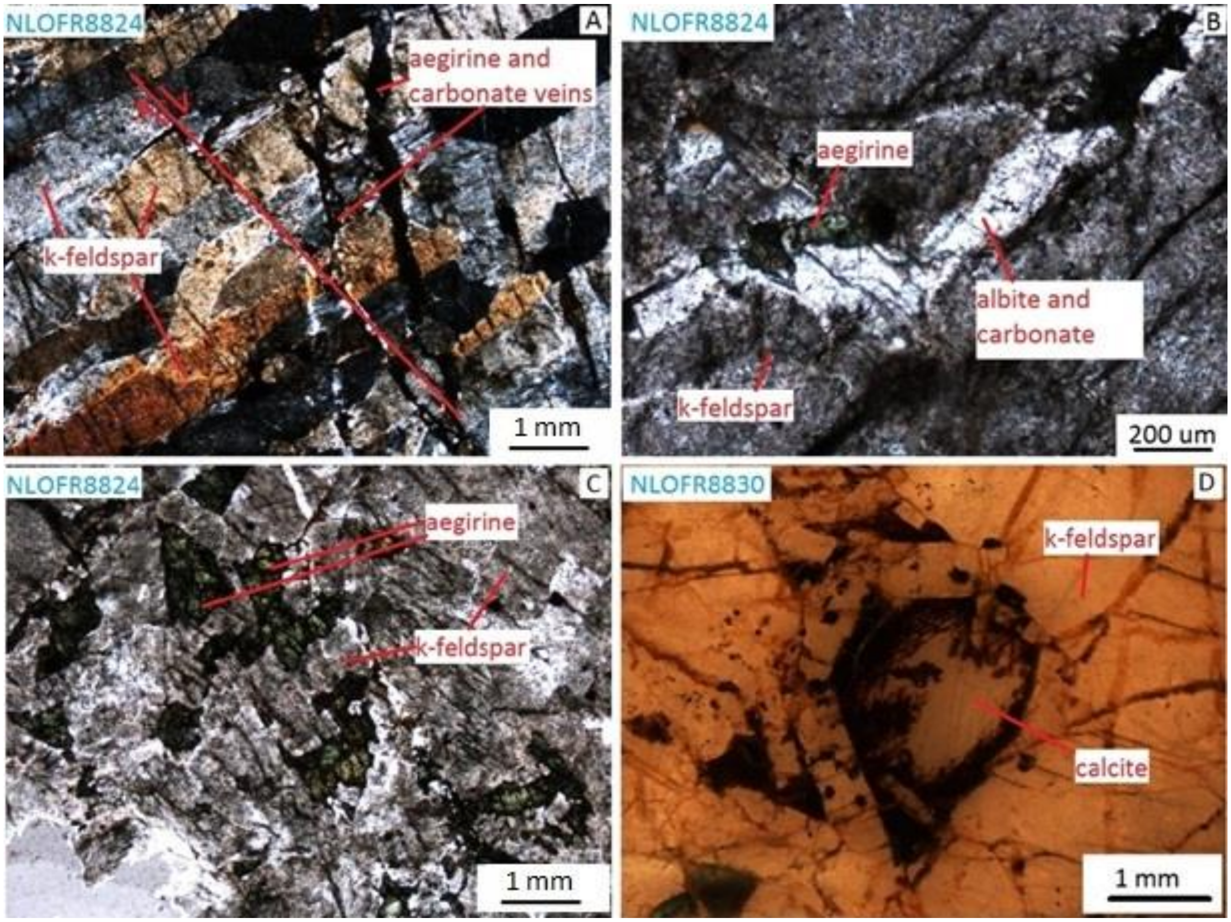

***Figure* 4.15 – (A) Potassium feldspar cross-cut by veins of aegirine and carbonate, both of which show minor offset (XPL). (B) Aegirine, albite and carbonate in a vein which crosscuts potassium feldspar (PPL). (C) Fine-grained aegirine showing space-filling texture, crystals are connected by small veinlets (PPL). (D) Fine-grained calcite showing space filling texture between potassium feldspar grains. Iron staining is abundant along cleavage planes (high resolution photo).**

The accessory minerals in potassic fenites include **zircon**, **zirconolite**, **titanite**, **ilmenite**, **pyrolusite**, **ferrocolumbite** and **pyrochlore**. Zirconolite is brownish gray in PPL with a grain size of 0.5-1.0 mm and anhedral crystal shape. It is commonly associated with titanite, and these phases seem to be commonly associated with fractures (*Figure* 4.18 A). Zircon grains often occur in small clusters as very fine-grained (~0.1mm) rounded inclusions, most often in potassium feldspar (*Figure* 4.18 B). Magnetite and pyrolusite are the dominant opaque minerals. They occur abundantly in mineralized fractures as 50-100 um clusters. Pyrolusite shows a creamy whitish colour with distinct bireflectance and very strong anisotropy (*Figure 4.18 C/D).*

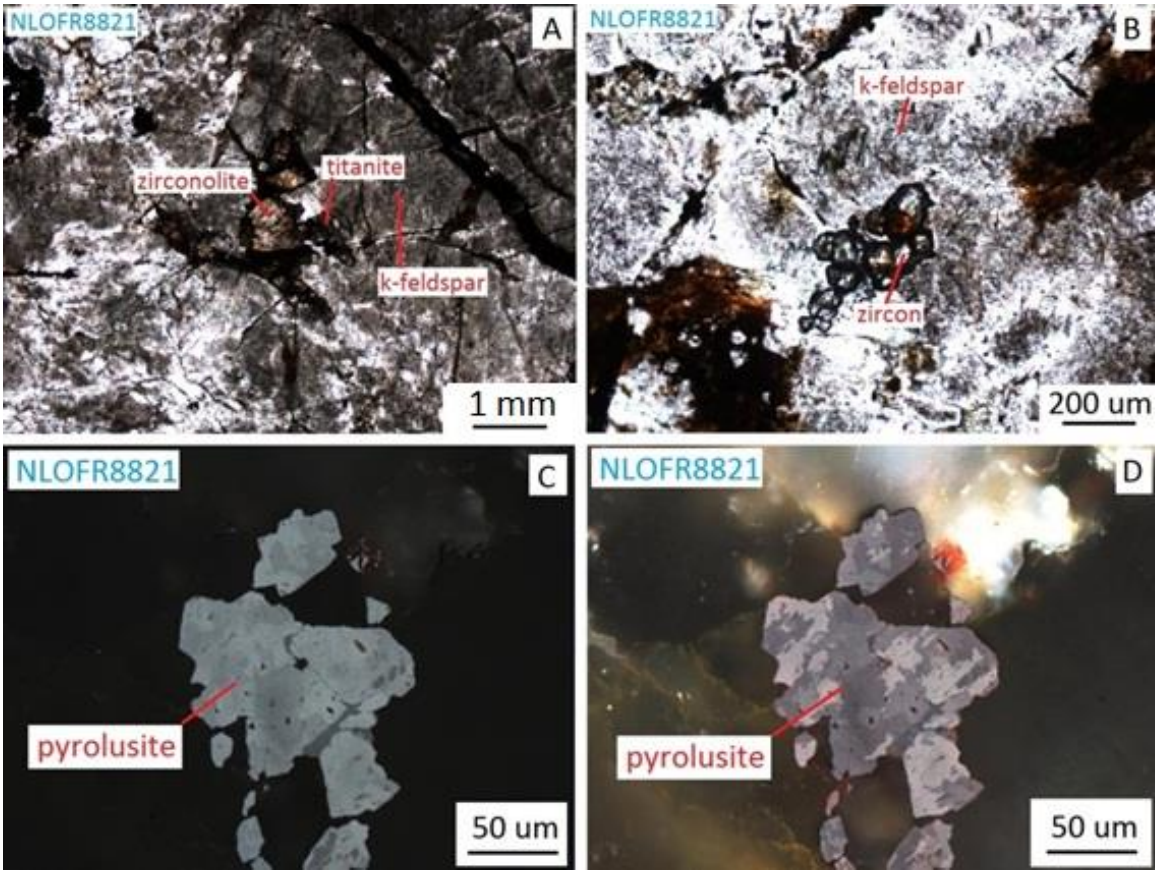

***Figure* 4.16 – (A) Zirconolite with minor titanite hosted in potassium feldspar, and occurring along a fracture (PPL). (B) Clustered zircon grains hosted in potassium feldspar (PPL). (C) Pyrolusite showing distinct bireflectance in reflected light (PPL). (D) The same pyrolusite grain showing distinct anisotropy in reflected light (XPL).**

Pyrochlore is fairly common in potassic fenites, and occurs in two styles of mineralization. Very fine-grained (1-10 µm) crystals of pyrochlore are abundant in sample 28 (*Figure 4.17 B*), hosted as inclusions in both 1 mm subhedral albite grains, but are also equally abundant in the surrounding groundmass of very fine-grained potassium feldspar and calcite. The more common type of pyrochlore observed in potassic fenites, occurs interstitially with zircon and magnetite (*Figure 4.17A*). This type of pyrochlore is most commonly observed along fractures and veinlets. This style of pyrochlore mineralization is significantly finer-grained than the subhedral pyrochlore seen in NLOFR8828.

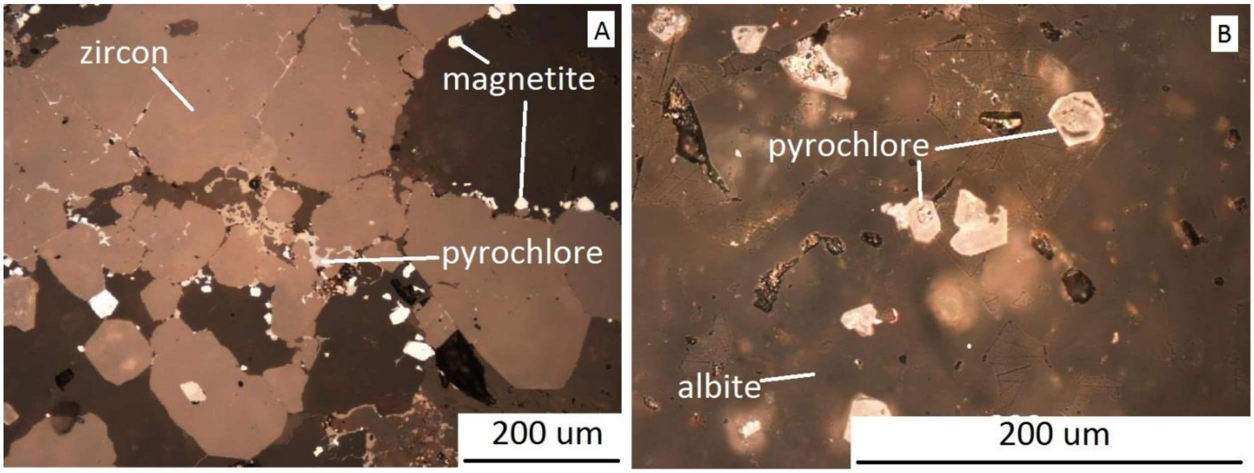

***Figure* 4.17 – (A) pyrochlore occurring interstitially between larger grains of magnetite and zircon (reflected light PPL) (B) Disseminated crystals of pyrochlore hosted as inclusions in both 1mm albite crystals, as well as the microscopic groundmass of potassium feldspar and carbonate (reflected light PPL).**

4.2 Mineral Chemistry

Identification and composition of minerals in 22 samples from the Lofdal complex were confirmed using EDS. Detailed WDS analyses were obtained for pyrochlore and feldspar specimens using the EMPA at Dalhousie University's microprobe facility. The following sections summarize the results of both types of analyses for felsic minerals, mafic minerals and a separate section is dedicated to the analyses of pyrochlores.

4.2.1 Felsic Minerals

Felsic minerals observed in the studied samples from the Lofdal complex include: potassium feldspars, albite, nepheline and cancrinite, apatite, and calcite. In general the mineral assemblages of albite, potassium feldspar, nepheline and cancrinite with minor apatite and calcite are characteristic of nepheline syenites and potassic fenites. For the carbonatite and siliciocarbonatite samples, the characteristic felsic mineral assemblage includes abundant calcite and apatite, with lesser albite and potassium feldspar. Nepheline and cancrinite are exclusively found in nepheline syenite samples.

Feldspars are a major rock forming mineral in this sample set. Potassium feldspars appear to be the most abundant, with albite generally being a more minor constituent in all samples. In almost all cases, potassium feldspars are easily identified by their cloudy/dirty grayish white appearance in PPL, while albite tends to be a clear white colour in PPL. Both albite and potassium feldspar are more abundant in potassic fenites, than in nepheline syenites. *Figure 4.18* shows the results of EMP data collected for feldspars in three samples, two potassic fenites and one nepheline syenite, NLOFR8821b, NLOFR8828, and NLOFR8834 respectively. Detailed tables of original WDS data and mineral formula calculations for feldspars are presented in *Appendix A-1* and *Appendix A-2* respectively.

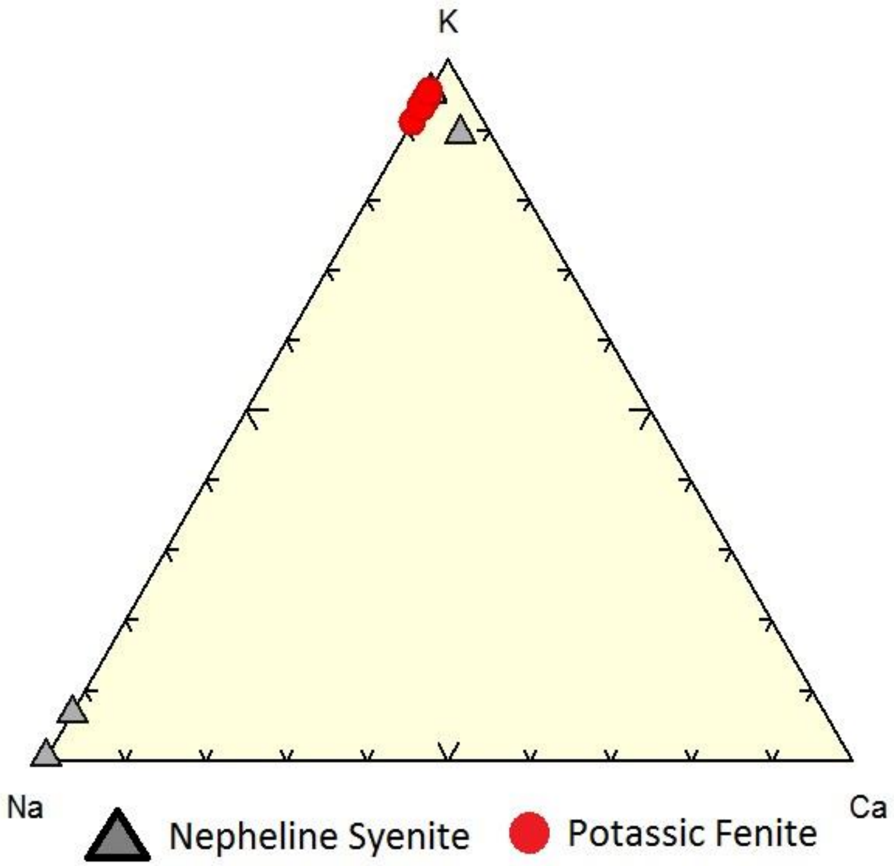

***Figure* 4.18 – EMP analyses of feldspars (albite and k-feldspar), normalized to a percentage ratio of atoms per formula unit. There is little variation observed between compositions of potassium feldspars between nepheline syenites and potassic fenites. Albite is typically present in the nepheline syenites.**

Nepheline was mainly identified through optical petrography as a cloudy white mineral in PPL which very commonly produced a clear uniaxial interference figure. Nepheline was confirmed using EDS (*Figure 4.19*) having a spectrum similar to albite, but with much lower silica content. Nepheline commonly appears to break down into a very fine-grained aggregate of cancrinite.

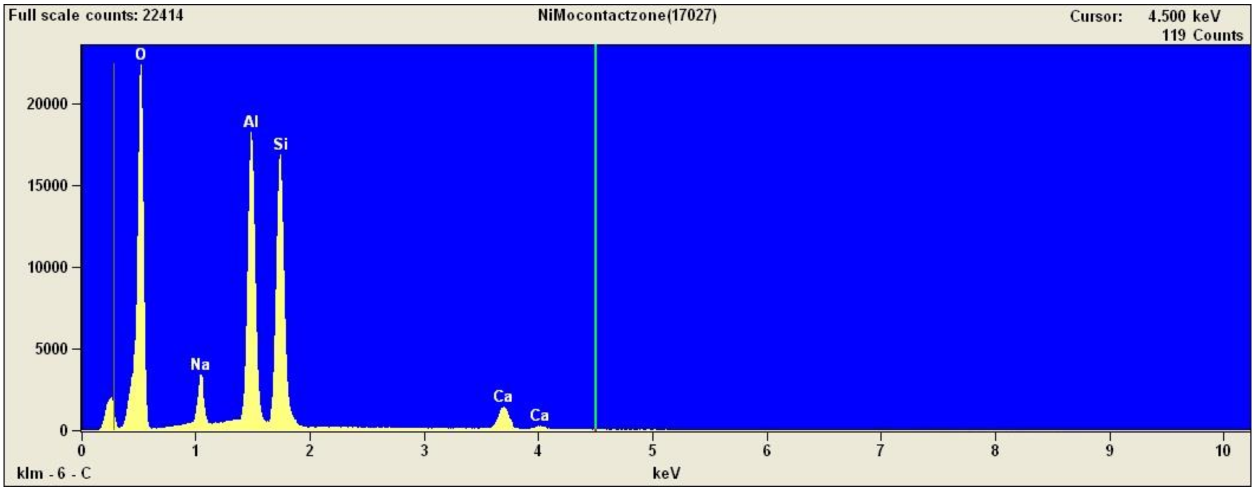

***Figure* 4.19 – EDS spectrum for nepheline in nepheline syenites (NLOFR8834). Nepheline is characteristically very deficient in silica.**

Carbonate is a major rock forming mineral in carbonatites and siliciocarbonatites, and plays an accessory role in potassic fenites, and to a lesser extent in nepheline syenites. Only in sample NLOFR8822 was the major carbonate mineral dolomite, in all other cases calcite is the only carbonate mineral present. Routine analyses of carbonate minerals during EDS work showed no REE's hosted in calcite.

Apatite is a major rock forming mineral in siliciocarbonatites and carbonatites, occurring as massive aggregates, as well as inclusions within calcite. Large aggregates of apatite appear to be distinct feature of siliciocarbonatites, which may contain as much as 25% apatite modally. In contrast, apatite is an accessory phase in both nepheline syenites and potassic fenites, occurring as isolated single crystals. EDS analyses of apatite shows that almost all apatites are of the fluorapatite variety (*Figure 4.20*).

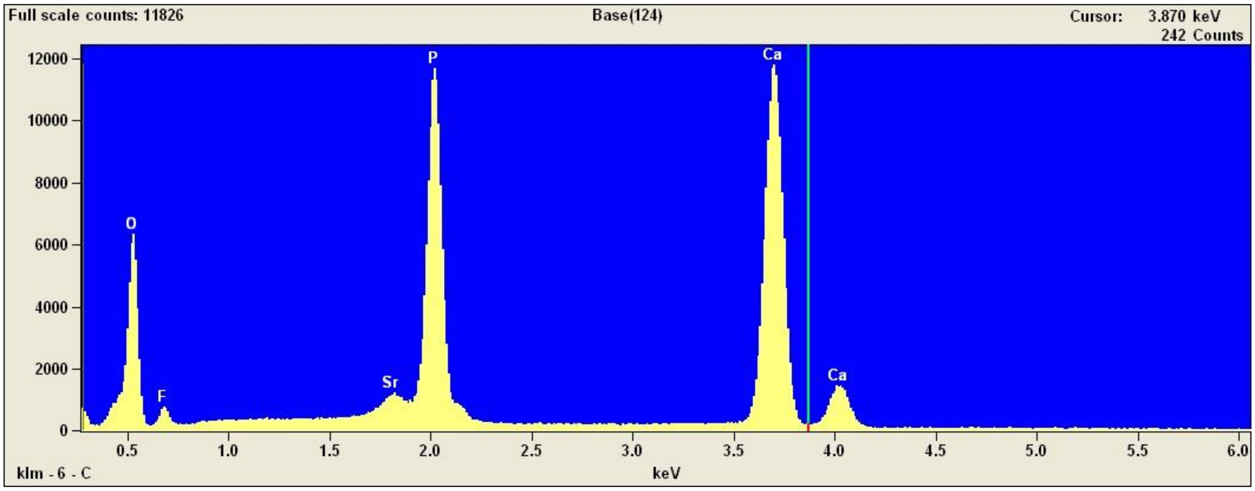

***Figure* 4.20 – EDS spectrum for fluorapatite (NLOFR8845).**

4.2.2 Mafic Minerals

There are two mafic minerals observed in the studied samples: biotite and aegirine. Biotite is a fairly common phase encountered mainly in samples of nepheline syenite and siliciocarbonatite, and to a lesser extent in potassic fenites and infrequently in carbonatite. Aegirine is a very abundant phase in samples of siliciocarbonatite, and may be found in certain samples of carbonatite and potassic fenite. Aegirine was not observed in any of the samples of nepheline syenite.

Biotite shows very little chemical variation between different sample types. Although biotite samples analyzed from siliciocarbonatites have visible iron exsolution lamellae visible only through the use of backscatter electron imaging (*Figure 4.21*). Aegirine similarly shows very little compositional variation between different rock types**. Aegirine** in carbonatites is only present in one sample as very fine-grained euhedral crystals, in contrast to the coarse-grained euhedral crystals which dominate samples of siliciocarbonatite. Aegirine found in potassic fenites most commonly forms as very fine-grained sheaves which develop within fractures; or less commonly, as anhedral medium-grained interstitial growths. A characteristic EDS spectrum for aegirine is shown in *Figure 4.22*. Calcium and magnesium seen in EDS spectrum for aegirine are due to the presence of carbonate inclusions, which are abundant.

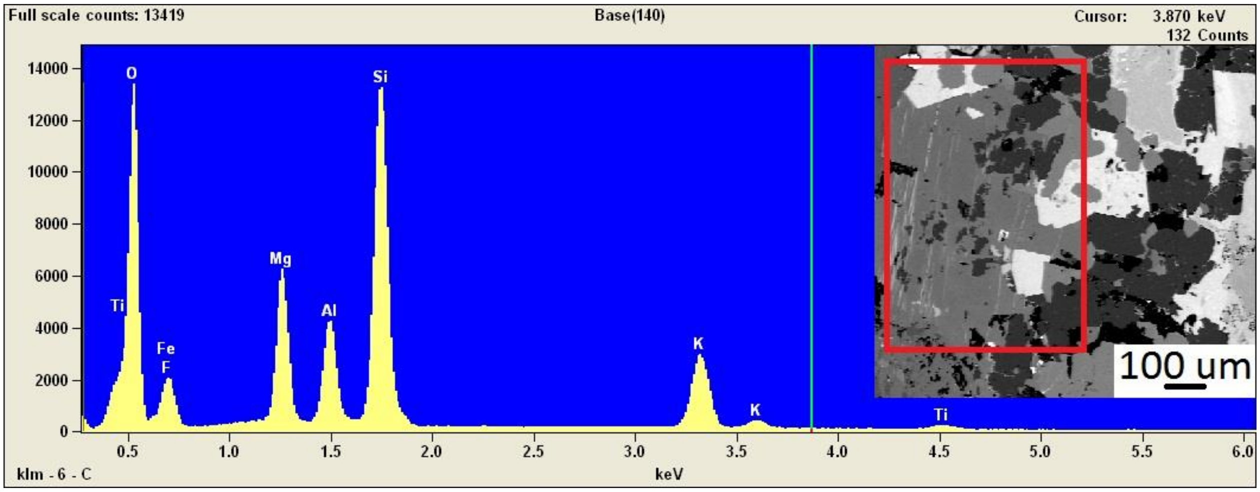

***Figure* 4.21 – EDS spectrum for biotite (NLOFR8845). Biotite in siliciocarbonatite was observed to contain iron rich exsolution lamellae as seen in the backscatter electron image above.**

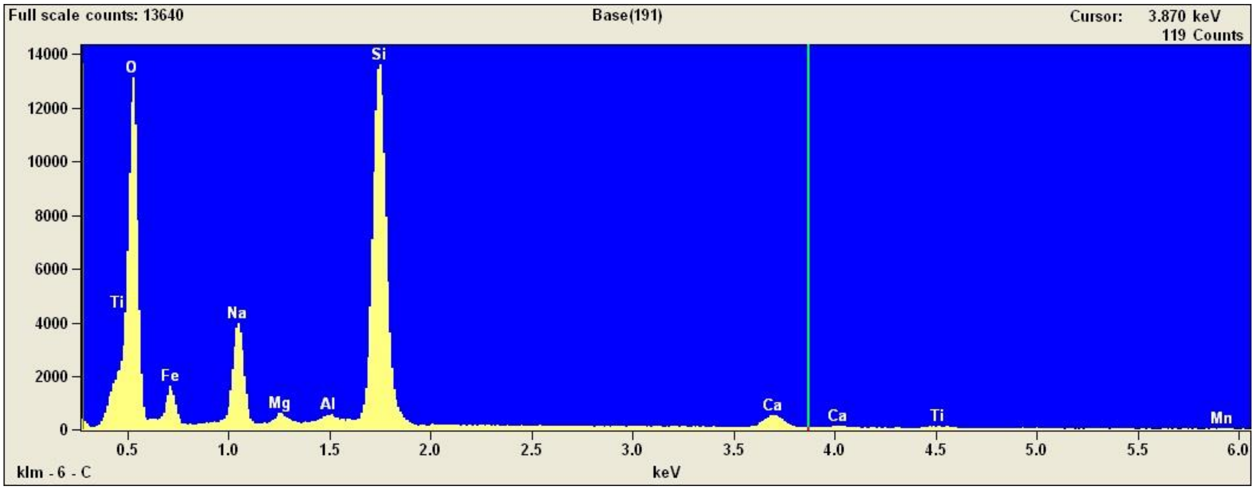

***Figure* 4.22 – EDS spectrum for aegirine (NLOFR8845).**

4.2.3 Pyrochlore

The pyrochlore supergroup contains three subgroups of cubic Nb-Ta-Ti oxides: betafite, microlite, and pyrochlore (Hogarth, 1989). These minerals follow the general chemical formula $A_2B_2O_6Z$ (Hogarth, 1989). The A-site is generally dominated by large cations in 8-fold coordination including Na, Ca, Sr, Pb, Sn, Sb, Y, U and less commonly Ag, Mn, Ba, Fe^{2+}, Bi^{3+}, Ce, Sc, and Th (Atencio et al., 2010). The B-site is generally dominated by smaller high field strength cations in 6-fold coordination including: Nb, Ti, Ta and less commonly Sb, W, V, Sn, Zr, Hf, Fe^{3+}, Mg, Al, and Si (Atencio et al., 2010). The Z-site is generally occupied by an anion of F, OH, O, and less commonly H_2O, K, Ca and Rb (Atencio et al., 2010). The ideal crystal structure of pyrochlore is shown in *Figure 4.23*, with A-site cations in red, B-site cations in blue contained as BO_6 octahedra, and Z-site anions in orange.

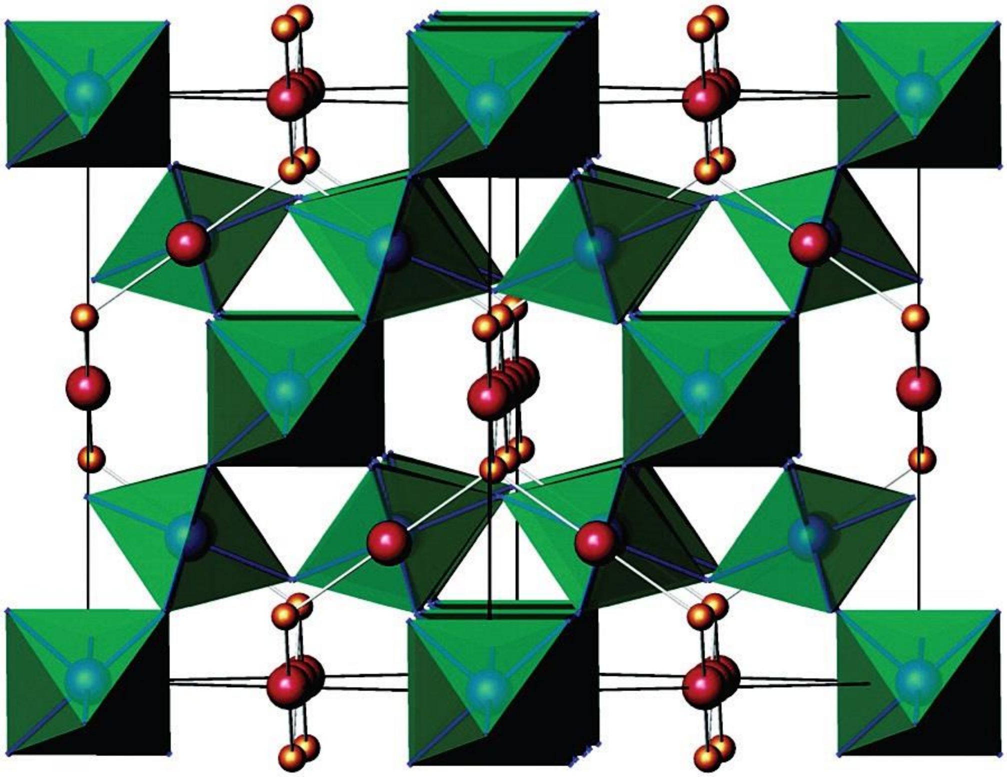

Figure **4.23 – idealized crystal structure of pyrochlore with A-site cations shown in red, B-site cations shown in blue, bounded as BO_6 octahedra, and Z-site anions in orange (Hendersen et al 2007).**

Further classification of pyrochlore types within each of the three subgroups is determined on the basis of the dominant A-site cation after Hogarth (1989). For specimens with atomic proportions of Na + Ca greater above 20% of the total A-site atoms, the subgroup name is used (pyrochlore, microlite, betafite). For specimens with atomic proportions of an atom other than Na or Ca above 20% of the total A-site atoms, a prefix is derived from that element as shown in *Table 4.1(A)*. Finally, following the classifications used by Mitchell and Zurevinski (2004), samples which contain a particularly abundant A-site cation other than Na or Ca, which does not have an atomic proportion above 20% of the total A-site cations, are given a separate prefix as denoted in *Table 4.1(B)*.

Table 4.1 – Pyrochlore nomenclature conventions after (Hogarth 1989) and (Mitchell et al., 2004)

Pyrochlore Nomenclature: *Pyrochlore subgroup*		
Dominant A-site Cation	(A) <20% a.p.f.u	(B) 5 – 20 % a.p.f.u
Na + Ca	Pyrochlore	
K	Kalipyrochlore	
Ba	Bariopyrochlore	
REE w/ LREE>HREE	Ceriopyrochlore	Ceroan pyrochlore
REE w/ LREE<HREE	Yttriopyrochlore	
Pb	Plumbopyrochlore	
U	Uranpyrochlore	Uranoan Pyrochlore
Th	(un-named)	Thorio pyrochlore

All occurrences of pyrochlore observed during petrographic analysis were analysed using WDS, the results of which are located in *Appendix B-1*. The results of cation recalculations have been plotted on the pyrochlore subgrouping ternary diagram *Figure 4.24* proposed by Hogarth (1989). All pyrochlores fall under the pyrochlore subgroup. Furthermore, using both previously mentioned classification schemes, all specimens are classified as pyrochlore, uranoan pyrochlore, and uranpyrochlore, from most to least abundant. There were no observed varieties of pyrochlore which show strong enrichment of any of the other A-site cations besides Na, Ca and U.

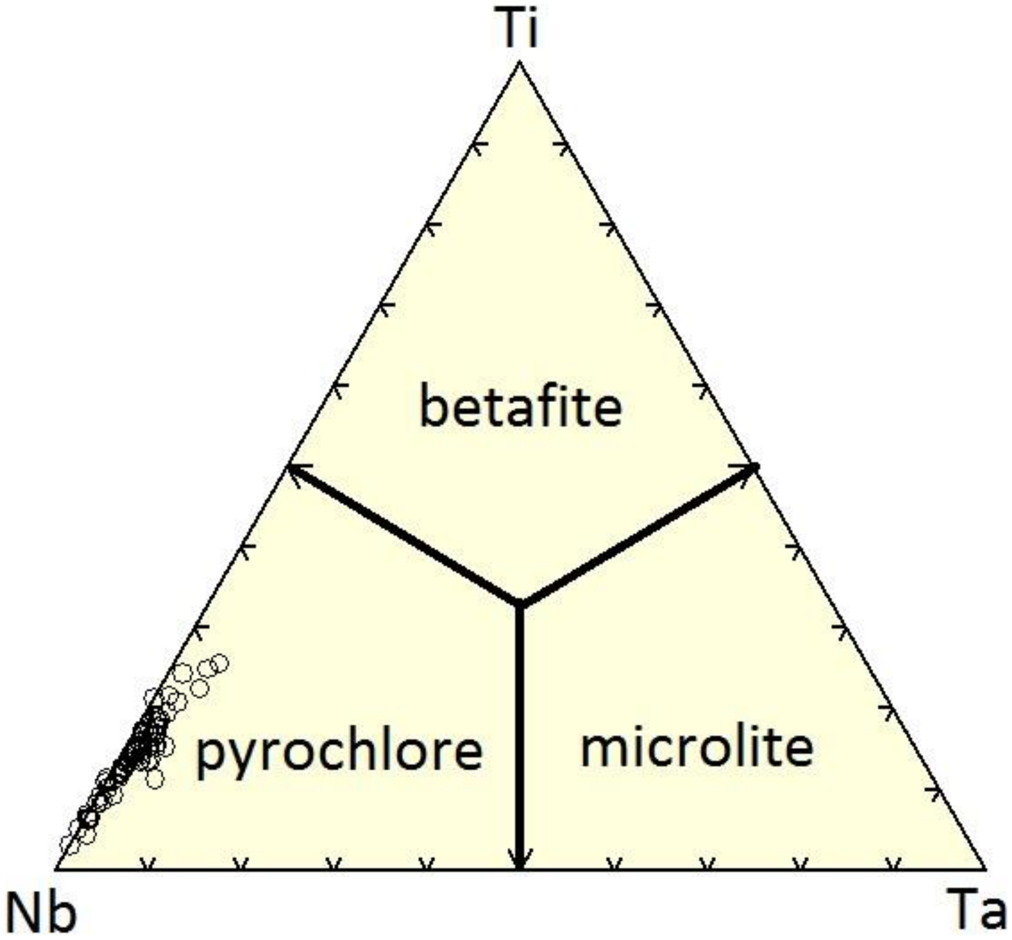

***Figure* 4.24 – WDS pyrochlore compositions, plotted by pyrochlore sub-groups: betafite, microlite and pyrochlore**

These different end members of pyrochlore occur in a number of different textural styles, indicative of various growth and alteration events. There are approximately five styles of pyrochlore mineralization, with each rock type having one or two diagnostic varieties. An example of each is shown in *Figure 4.25*.

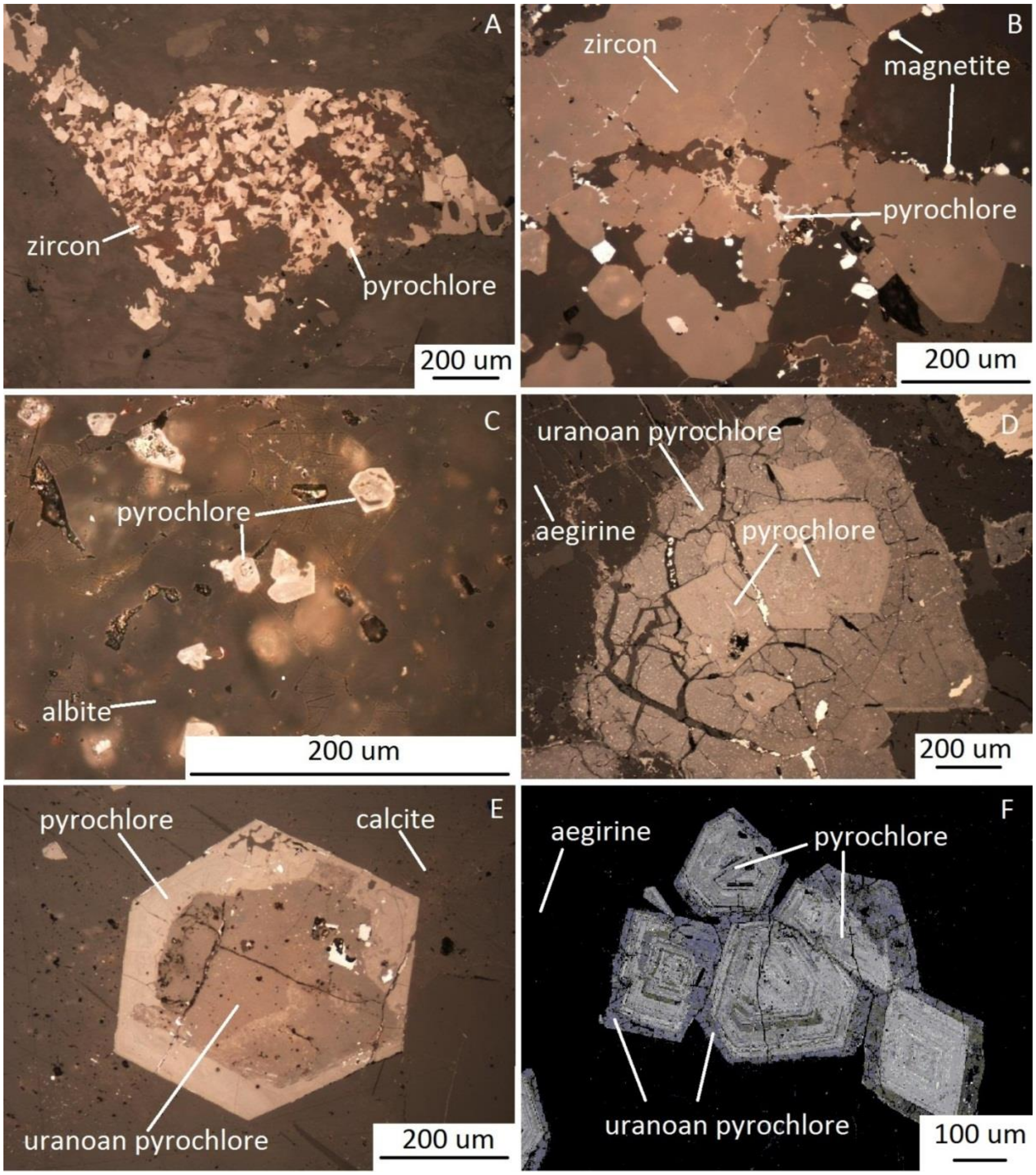

***Figure* 4.25 – (A) Pyrochlore in nepheline syenite. (B & C) Pyrochlore in potassic fenite. (D, E & F) Pyrochlore in siliciocarbonatites**

Pyrochlore occurring in nepheline syenite (*Figure 4.25A*) is quite rare and is strongly associated with the presence of zircon. Compositionally this mineralization is classified as simple pyrochlore with Na and Ca as the dominant A-site cation. Pyrochlore occurring in potassic fenites has two distinct mineralization styles (*Figure 4.25 B, C*). The first variety (B) occurs as an anhedral fracture-controlled bleb associated with magnetite and zircon. The composition of this pyrochlore also falls under the basic pyrochlore classification. The second (C) occurs as very small subhedral disseminated grains of simple pyrochlore hosted as inclusions in feldspars. Between the nepheline syenites and potassic fenites there appears to be very little compositional variety in pyrochlore specimens. However, it might be noted that the second most abundant cation (although not at all abundant in absolute terms) is cerium, which seems to occur in trace amounts in specimens from both rock types, slightly more prevalent in nepheline syenites. It is notable that Ce is very rarely observed in pyrochlores from any of the other samples.

Pyrochlore is abundant in siliciocarbonatite, and generally shows the largest grain size of all occurrences. There are two characteristic varieties for these samples (*Figure 4.25 D,E*). The first (D) shows an inner grain of euhedral pyrochlore with distinct oscillatory zoning. This zoning is characterized by smooth rapidly alternating compositions which form parallel to the {111} crystal face. The outer portion of these minerals is dominated by a third pyrochlore composition. The texture of this third composition is somewhat unclear, as some samples show a smooth contact to the inner crystal, while other crystals show this rim cross-cutting the inner crystal. The second variety observed in the siliciocarbonatites (E) is very similar to the previous variety, but the compositions appear to be inverted. The inner portions of these crystals do not display zoning, and appear strongly metamict. The rims of these crystals are distinctly cleaner looking, and some samples show a few short compositional zones.

Since pyrochlores found in siliciocarbonatite samples are the largest, and provide overall significant Nb and U enrichment to these samples, a more detailed investigation of these compositions and textures was warranted. A small cluster of grains found in sample NLOFR8825b (*Figure 4.25 F*) was chosen as a specimen for WDS element distribution X-ray mapping using the EMPA facility at Dalhousie University. The resulting images show relative levels of enrichment of a specific element using a colour scale: blue and black are very low concentrations, yellow and red are very high concentrations, and greens and yellows indicate mid concentration levels. This analysis is qualitative, and does not provide absolute enrichment values. In *Figure 4.26* the element distribution maps for Ca, Na and Nb are shown. These elements are presented together because they show a paired fluctuation through the oscillatory zoning, and are all strongly depleted in the outer rim. It is evident particularly looking at the maps for calcite and niobium that the outer rim composition is very different from the oscillatory zoning in the inner portions of the crystals.

The element distribution maps for U, Si, Ta and Ti are shown in *Figure 4.27*. The maps for U and Si both show elevated concentrations within the oscillatory zones characterized by low Ca, Na, and Nb. Similarly, they are particularly enriched in the outer rim, where the low concentrations of Ca, Na and Nb are most pronounced. The distribution of Ti within the oscillatory zones is fairly consistent, with only a minor contrast between zones; however, the outer rims appear to show some enrichment significantly higher than any of the inner compositions. The Ti distribution map also displays another important feature; the fracture which cuts through the middle of the grain shows a composition which closely matches the outer rim composition, this is also well defined in the Nb and Ca maps. The distribution of Ta appears to also be fairly consistent within the inner portions of the crystal and is very strongly enriched in the outer rim.

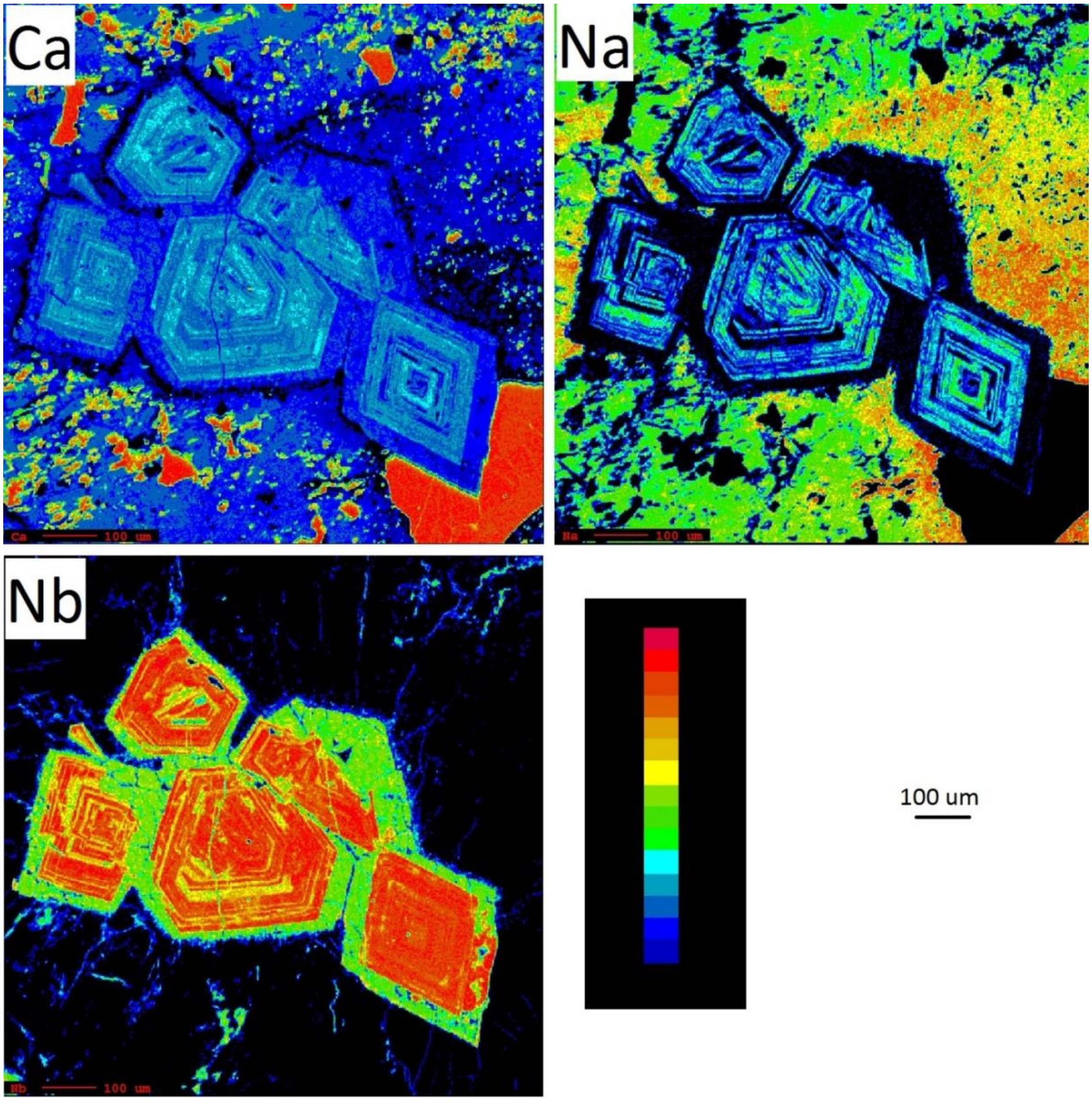

***Figure* 4.26 – Element distribution map (Ca, Na, Nb) for pyrochlore in sample NLOFR8825b. Calcium, sodium and niobium show paired distribution through oscillatory zoning, and are all depleted in the outer rim; the host mineral phase is aegirine.**

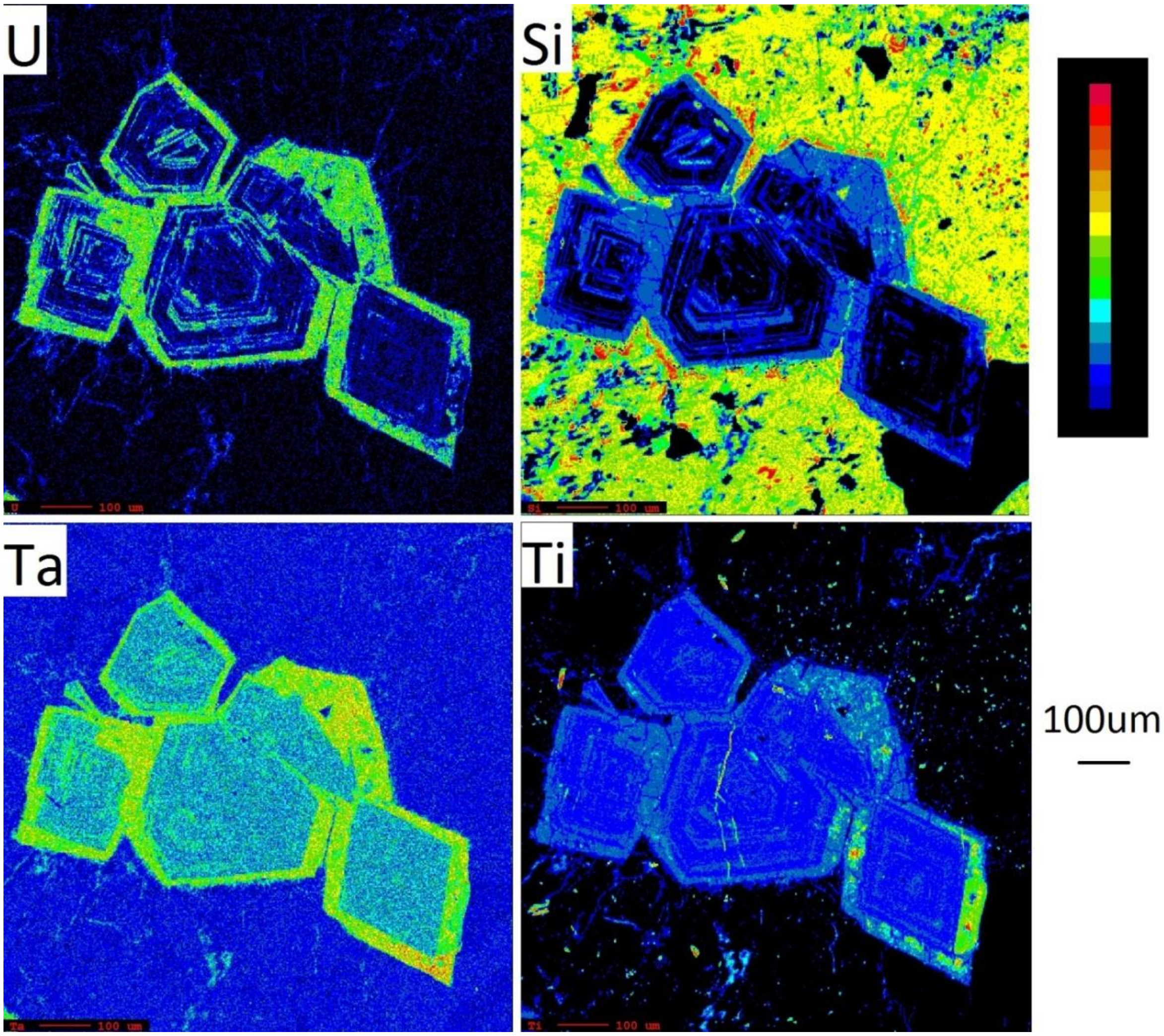

***Figure* 4.27 – Element distribution map (U, Si, Ta, Ti) for pyrochlore in sample NLOFR8825b. U and Si show a paired distribution with zones of enrichment correlating with zones depleted in Ca, Na and Nb. Ti seems to follow this trend but is less pronounced. The outer rim composition is strongly enriched in U, Si, Ta and Ti. The host mineral phase is aegirine.**

4.3 Whole Rock Geochemistry

Whole rock major and trace element data, along with rare earth element data were obtained for each of the 22 samples of the Lofdal carbonatite complex. Whole rock geochemistry results for major element oxide analyses are presented in *Appendix D-1*. Results for rare earth element analyses and trace element analyses are presented in *Appendix D-2* and *Appendix D-3* respectively. Following petrographic analyses, whole rock geochemistry results for each sample were classified by rock type. The plots which follow are intended to demonstrate trends both for the nepheline syenite to potassic fenite, and the carbonatite to siliciocarbonatite.

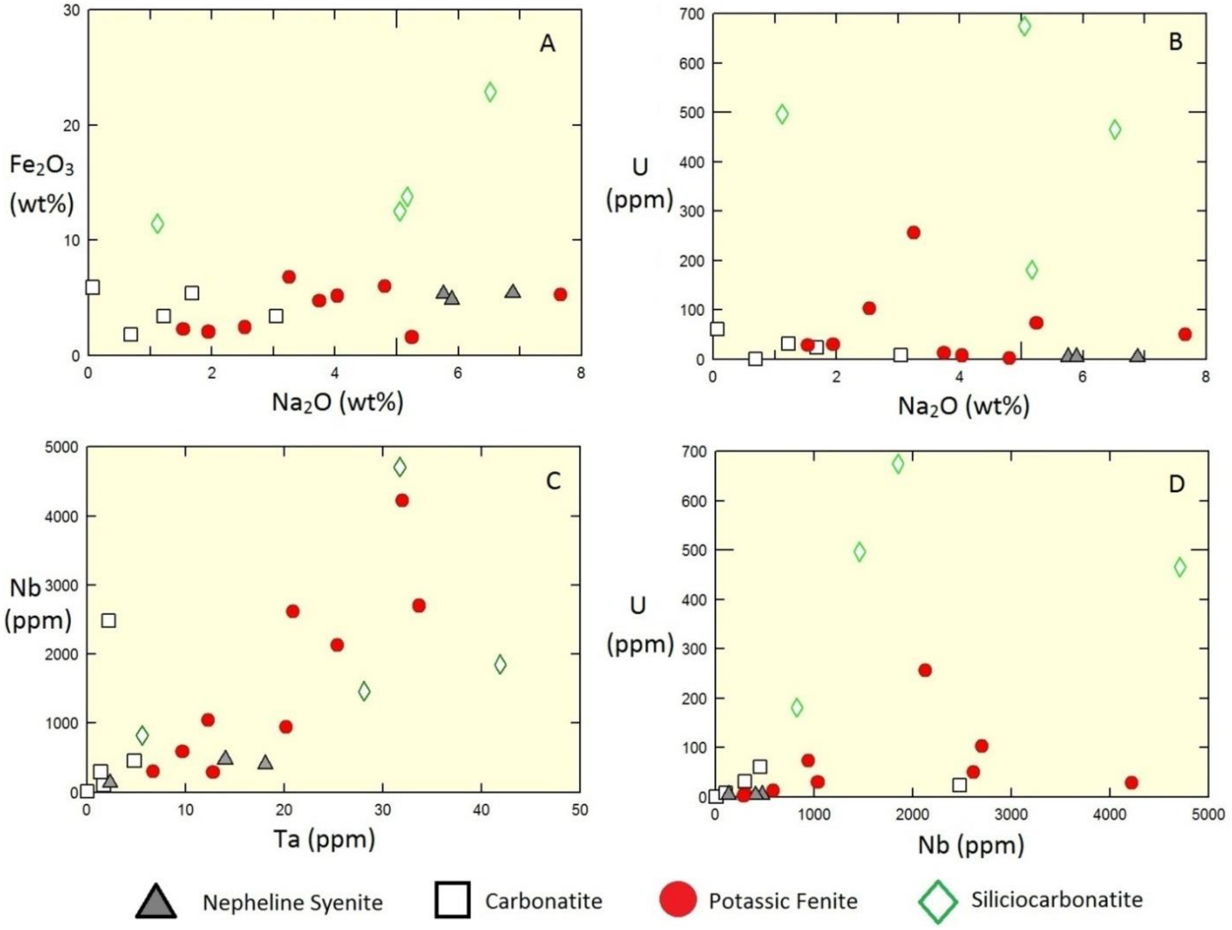

***Figure* 4.28 – (A) Fe_2O_3 vs. Na_2O. (B) U vs. Na_2O. (C) Nb vs. Ta. (D) U vs. Nb.**

The Fe_2O_3 versus Na_2O plot of *Figure 4.28 (A)* shows decreasing sodium content from the nepheline syenites to the potassic fenites with a possible very minor decrease in iron content as well. Inversely, the siliciocarbonatites show an increase in both iron and sodium content in comparison to the carbonatites. The U versus Na_2O plot of *Figure 4.28 (B)* shows a strong increase in uranium content for the siliciocarbonatite samples compared with the carbonatites, and a slight increase in uranium content for the potassic fenite samples compared the nepheline syenites. The Nb versus Ta plot of *Figure 4.28*

(C) shows a positive correlation between niobium and tantalum, reflecting their geochemical similarity and indicating of the presence of pyrochlore. It is evident that pyrochlore is abundant in both the potassic fenites and the siliciocarbonatites compared to the carbonatites and nepheline syenites. Pyrochlore does appear to be present in the nepheline syenites to some extent, and in one sample of carbonatite. The U versus Nb plot of *Figure 4.28 (D)* shows enrichment in uranium and the extent to which it is associated with the presence of pyrochlore. While there does appear to be a strong correlation, it is evident that the pyrochlore varieties enriched in uranium appear to be far more prevalent in the siliciocarbonatites than the potassic fenites.

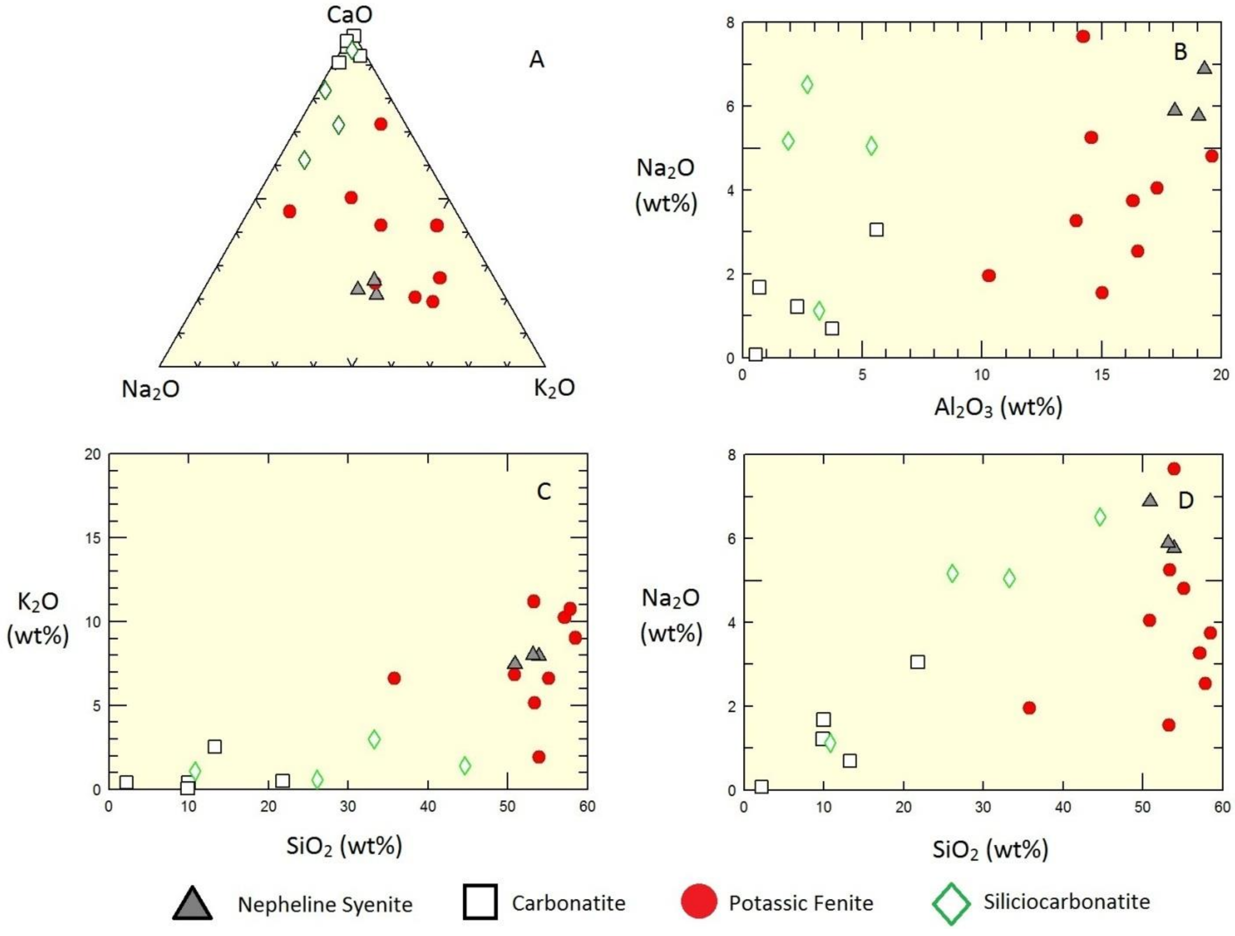

***Figure* 4.29 - (A) tri-plot CaO-Na_2O-K_2O. (B) Na_2O vs. Al_2O_3. (C) K_2O vs. SiO_2. (D) Na_2O vs. SiO_2.**

The CaO-Na_2O-K_2O ternary plot of *Figure 4.29 (A)* shows carbonatites becoming more sodium enriched in progressing toward the siliciocarbonatites, while the nepheline syenites become enriched in either sodium or calcium at the expense of the other in progressing toward the potassic fenites. The Na_2O versus Al_2O_3 plot of *Figure 4.29 (B)* illustrates a mild decrease in aluminum content coupled with decreasing sodium content from the nepheline syenites to the potassic fenites. The K_2O versus SiO_2 plot of *Figure 4.29 (C)* shows no definitive change in potassium content for either the siliciocarbonatites or potassic fenites. The Na_2O versus SiO_2 plot of *Figure 4.29 (D)* shows an increase in silica content from the carbonatite to siliciocarbonatite samples with no change in silica content for the potassic fenite samples.

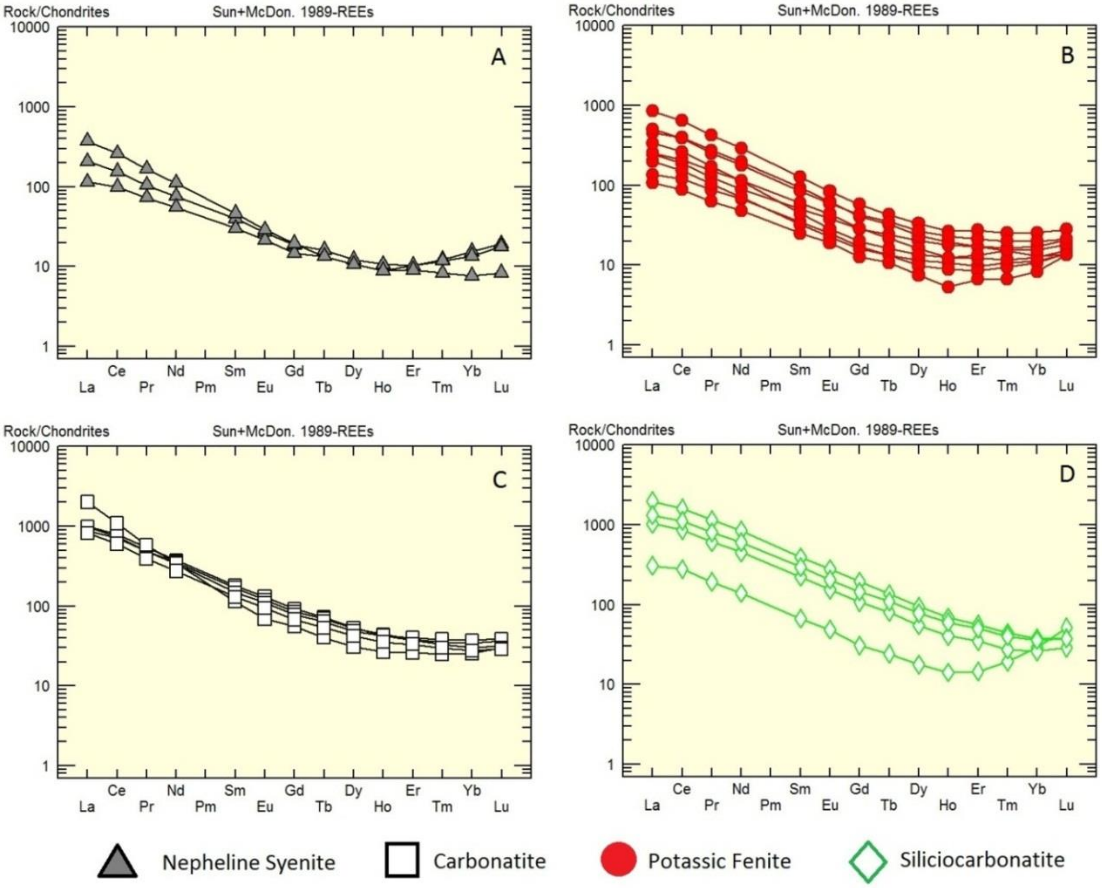

***Figure* 4.30 – REE distribution plots (after Sun and McDonough 1989).**

Rare earth element diagrams for all four rock types show a similar enrichment pattern with a negative slope that is steeper for the light rare earths than for the mid-rare earths (*Figure 4.30*). Certain samples within each rock type show heavy rare earth enrichment compared to the middle rare earths. Overall, nepheline syenites have one order of magnitude less rare earths than carbonatites. Potassic fenites are rare earth enriched compared to nepheline syenites, and siliciocarbonatites are rare earth enriched compared to carbonatites.

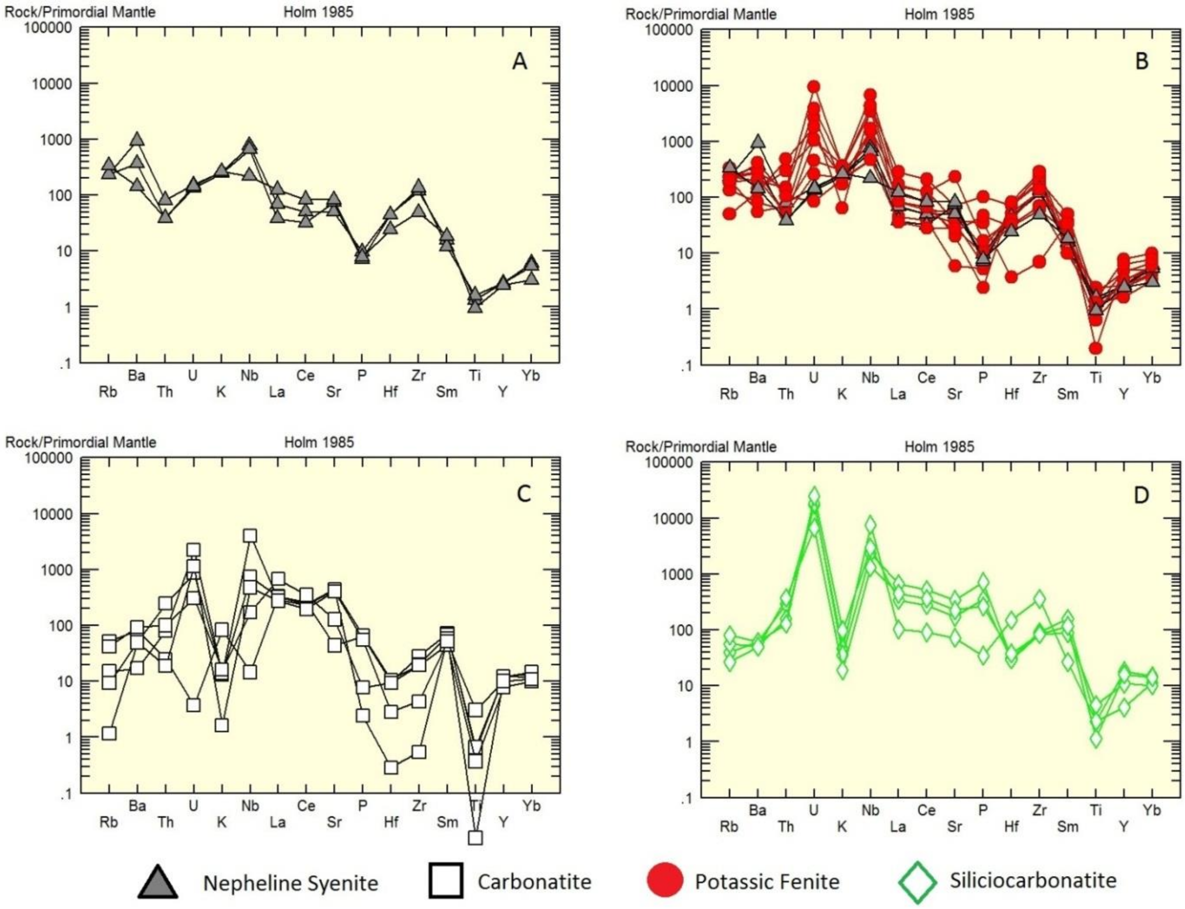

***Figure* 4.31 – Incompatibility diagrams normalized to Primordial Mantle (Holm 1985) for nepheline syenites, potassic fenites, carbonatites and siliciocarbonatites. Refer to text for descriptions.**

Spider-diagrams, with the elements plotted in order of increasing compatible behavior and normalized to primordial mantle (*Holm 1985*), are presented in *Figure 4.31*. The spider-diagram for nepheline syenites (*Figure 4.31 A*) show a general enrichment in incompatible elements, with notably strong enrichment of the large ion lithophile (LIL) elements Ba and Rb as well as Nb, a high field strength (HFS) element. The spider-diagram for potassic fenites (*Figure 4.31 B*) is overlain with plots for nepheline syenites in order to illustrate contrasts. There is a clear depletion in LIL elements Ba and Rb,and a strong enrichment in the HFS elements Nb and U in the fenites relative to the nepheline syenites. There is also significant enrichment in P. The incompatibility diagram for carbonatites (*Figure 4.31 C*) is characterized by low concentrations of the LIL elements Rb and Ba, and HFS elements Ti, Hf and Zr. They are distinctly enriched in the HFS elements U and Nb. The spider-diagram for siliciocarbonatites (*Figure 4.31 D*) display slightly higher enrichments of LIL elements Rb and Ba, as well as HFS elements Hf and Zr when compared with carbonatites. They also show a very significant enrichment in HFS elements U and Nb.

Chapter 5: Discussion

5.1 A Summary of Field Observations

The Main intrusion consists of a large composite body of nepheline syenite intruded by sovite, elliptical in plan with approximately 1.5km^2 of surface exposure (Swinden and Siegfried, 2011). At the contact between the carbonatite and nepheline syenite, there appear to be two distinct contact phases. The first is a large irregular but persistent halo of metasomatic alteration in the syenite and syenitic breccias surrounding the sovite body. The second is a coarse-grained aegirine rich siliciocarbonatite along the immediate contact between the sovite and nepheline syenite. The siliciocarbonatite is strongly enriched in niobium and uranium (*Figure 5.1*).

The Main intrusion is the larger of two carbonatite plugs in the Lofdal complex, which are accompanied by hundreds of phonolite and carbonatite dykes over an area of nearly 200km^2. The carbonatite dykes are variably enriched in light rare earths and heavy rare earths; these carbonatite intrusions appear to post-date, on the basis of cross-cutting relationships, the intrusion of a large body of nepheline syenite, and phonolite dykes. Both the phonolite and sovite dykes show a dominantly NE-SW orientation, consistent with the structural fabric of the Huab Metamorphic Complex (HMC).

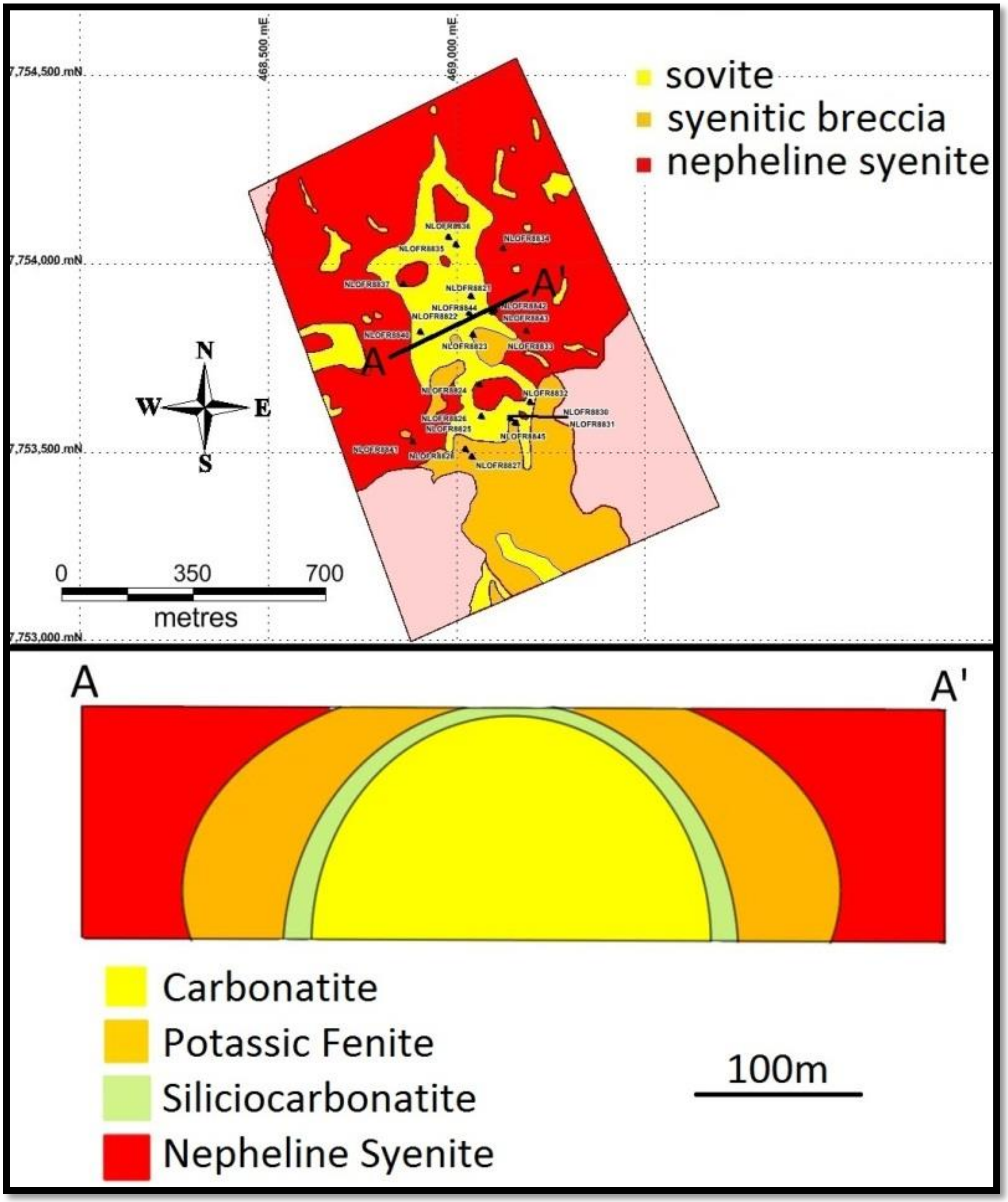

***Figure* 5.1 – The geology of the Main intrusion, with cross section A-A’ showing the proposed schematic model of carbonatite intrusion into nepheline syenite, and contact phases potassic fenite and siliciocarbonatite.**

Although exploration interest for rare earth elements is mainly centered on the dykes at the Lofdal property, there is also economic interest in the Main intrusion focused on uranium enrichment zones detected by airborne radiometric surveys. Grab sampling of outcrops in the area of these anomalies shows that anomalous uranium concentrations are also associated with niobium mineralization. The key objective of this study has been to conduct a detailed mineralogical, textural and geochemical study of the uranium and niobium mineralization. This allows for the development of a geological model which explains the nature and origin of the mineralization and provides strategies for exploration of the uranium and niobium potential in this area.

5.2 Genetic Relationship between Nepheline Syenite and Carbonatite

Isotopic studies to determine the genetic relationship between nepheline syenite and carbonatite of the Lofdal carbonatite complex were not performed for this study. Therefore any speculation about the genetic relationship between these two bodies is purely based on similarities between mantle signatures from whole rock geochemistry plots. As stated by Woolley and Kjarsgaard (2008), carbonatite which is genetically related to an associated nepheline syenite is expected to have formed through fractionation or through immiscible separation in the crust. It is implied that these bodies did not form independently at different depths in the mantle. Rare earth element distribution plots for nepheline syenite and carbonatite (*Figure 4.30*) show nearly identical signatures, with the carbonatite having slightly stronger overall REE enrichment. It is thus inferred that these two bodies are genetically related. However, no arguments in favour of either fractionation or immiscibility are offered as no textural evidence was encountered to support either possibility. Immiscibility seems to be the more likely of the two based on the similar relative volumes of the two bodies as determined by outcrop exposure. A more definitive argument for the genetic relationship between these two bodies might be afforded through examination of radiogenic isotopic signatures.

5.3 Nature of Contact Phases

There are two important contact phases present between the carbonatite and nepheline syenite that are unique to the contact area: potassic fenite and siliciocarbonatite. Interpretation of the origins of these two contact phases is integral in the development of a geological model for the Main intrusion and its associated mineralization.

5.3.1 Origin of the Potassic Fenite

Potassic fenites of the Lofdal complex are found in an irregular yet persistent aureole around the sovite plug of the Main intrusion and are believed to have resulted from metasomatism of the nepheline syenite by alkaline fluids released by the carbonatite body during the early intrusive phases. Potassic fenitization appears to affect both the nepheline syenites and syenitic breccias, indicating that fenitization post-dated brecciation.

Geochemically potassic fenites are characterized overall by a decrease in Al and Na, and to a much lesser extent Fe, and an increase in niobium and uranium compared to nepheline syenites. Curiously, the most diagnostic feature of potassic fenites should be an overall increase in K compared to the protolith. However, whole rock geochemistry for potassic fenites of the Main intrusion shows two distinct groups, one which shows an increase in K (group A), and one which shows a decrease in K (group B), when compared with nepheline syenites (*Figure 5.2*). Potassic fenites of group *(A)* show a significant decrease in Na (average decrease of 3.4 wt% Na_2O), and a significant increase in K (average increase of 2.5 wt% K_2O) compared to nepheline syenites with no significant change in total alkali content.

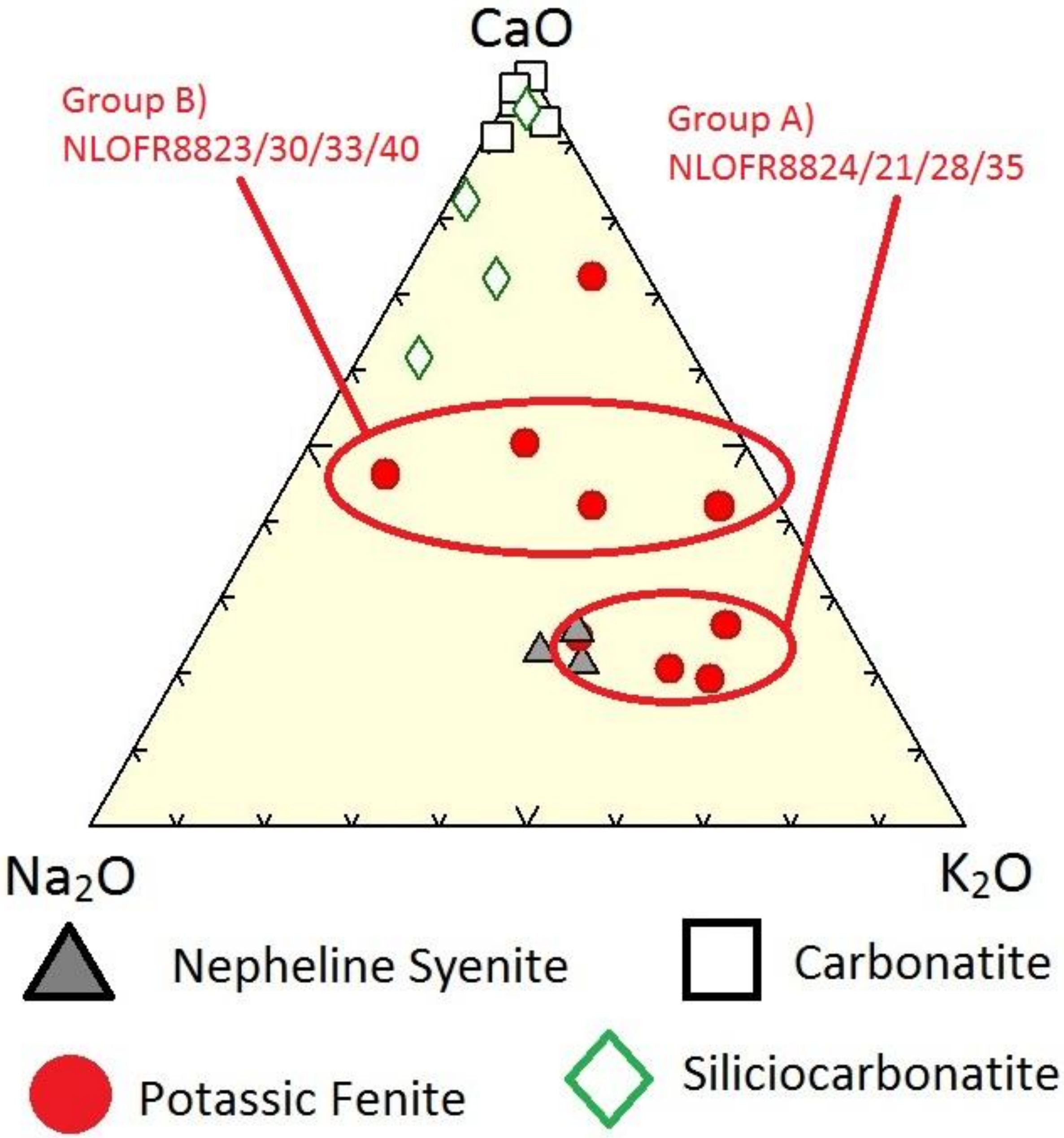

***Figure* 5.2 – Na-Ca-K Tri-plot showing two groups of potassic fenites. Group A shows overall potassium enrichment compared to nepheline syenite protoliths. Group B shows overall potassium depletion compared to nepheline syenite protoliths. Group B potassic fenites has an overall loss of total alkali's of 3.3wt% (K_2O + Na_2O) as well as 3.4wt CaO increase.**

Potassic fenites of group (B) show a slight decrease in Na (average decrease of 0.7 wt% Na_2O) and a slight decrease in K (average decrease of 2.7 wt% K_2O) compared to nepheline syenites. The total alkali content for group (*B*) shows an average decrease of 3.3 wt% Na_2O+K_2O. Additionally, potassic fenites of group (*B*) show an average increase of 3.4 wt% CaO compared to nepheline syenites.

On a textural basis, samples from both groups appear very similar, being dominantly composed of coarse-grained potassium feldspars. Therefore there are two possible explanations for the geochemical variation between these two groups. The first possibility is that the fenitization process was fairly inhomogeneous leaving certain areas pervasively affected by an influx of potassium, and other areas affected by an influx of calcium. The carbonate rich fluid may have leached alkalis from these samples causing an overall alkali reduction. The second possibility is that all samples were affected by an early potassic metasomatism which caused recystalization of nepheline syenites to potassium feldspar dominated fenites. A second alteration event resulting from a carbonate and sodium rich fluid may have reconverted many of the potassium feldspars to albite as a pseudomorph. This event would introduce calcium and sodium in exchange for potassium, and cause an overall reduction in alkali content.

The second possibility is arguably more likely, because of the significant textural similarities between samples from both groups. However, it is noted that carbonate and aegirine rich veins are also present in samples from group (*A*), indicating that the passage of sodium rich carbonate fluids through high K potassic fenites did not seem to cause alteration of potassium feldspar to albite. It appears that samples from group (*B*) contain more significant carbonate veining, and therefore it is possible that introduction of later sodium rich carbonate fluids may have been able to induce alteration more easily in areas where fracturing was more pervasive. In either case, a definitive explanation for the discrepancy between the two groups of potassic fenites cannot be determined on the basis of samples obtained for this study. Within each group of fenites, there are only four to five samples and each sample set has one or two outliers. Additionally the geochemical variation within these groups is much more significant than geochemical variation for nepheline syenites; this is likely attributable to the metasomatic nature of the potassic fenites, a process which does not typically produce homogeneous alteration. A larger sample set of potassic fenites using a grid sampling method will be required to comprehensively constrain the chemical changes related to the fenitization process at the Lofdal complex.

5.3.2 Origin of the Siliciocarbonatite

Siliciocarbonatites of the Lofdal complex are constrained to the contact between the sovite and nepheline syenite bodies. Unlike potassic fenites, the siliciocarbonatites do not exist in a large aureole, but instead occur only within meters of the contact zone, on the basis of outcrop observations. Siliciocarbonatites are composed of abundant coarse-grained euhedral to subhedral aegirine, calcite, fluorapatite, biotite, with minor magnetite, pyrochlore and uranpyrochlore. Feldspars are also observed in siliciocarbonatite samples, but textural evidence is indistinct to provide an argument for whether or not these feldspars crystallized from the carbonatite magma, or whether they represent xenoliths from the potassic fenites.

Geochemically the siliciocarbonatites show significantly higher concentrations of Fe, U, Nb, P, Na and Si, with a decreased concentration of Ca when compared to relatively pure carbonatite samples. Their trace element geochemistry shows a significant increase in the high field strength elements Zr and Hf.

It is inferred that the siliciocarbonatite is magmatic in origin, given the coarse-grained crystal size, euhedral crystal shapes and oscillatory zoning. Geochemically these rocks are very similar to pure carbonatites. One sample of pure carbonatite contains a band of aegirine and associated pyrochlore, this limited crystallization is interpreted to indicate that these minerals at least briefly occurred along the liquidus during carbonatite crystallization. Their greater abundance in siliciocarbonatites therefore suggests the elements required to crystallize aegirine and pyrochlore accumulated in the residual melt. Geochemical evidence also seems to support the hypothesis that siliciocarbonatites are late magmatic and not metasomatic, as the oxide plots demonstrate that siliciocarbonatite trends evolve from carbonatite and not nepheline syenite. The final line of evidence to support a magmatic origin for the siliciocarbonatites comes from detailed interpretation of pyrochlore and uranpyrochlore crystals, which are abundant in these rocks (*See Section 5.4*).

There are two possibilities to explain the origins of the siliciocarbonatite. The first and less likely possibility is that it is the result of sodic fenitization. In this case textural and geochemical similarities and evolutionary trends from nepheline syenite would be expected. The second and preferred possibility is that the siliciocarbonatite formed from a residual fluid-rich magma resulting from extended fractional crystallization of the carbonatite. In this case, residual magmatic silica and volatile-rich fluids from the carbonatite magma would migrate towards the margins of the intrusion during crystallization. Crystallization of silicate phases would be in the carbonate magma, but through progressive crystallization of carbonate, silicate phases would eventually begin to crystalize. This would be accompanied by the crystallization of fluorapatite (present at up to 25% modally in siliciocarbonatites). The rapid crystallization of fluorapatite would reduce the activities of P and F, which decreases the solubility of Nb, Ta, and U (Hogarth et al. 2000). This occurs because these elements often form fluorine and phosphate complexes, and as P and F are consumed through the crystallization of fluorapatite, the solubility of Nb, Ta and U decreases rapidly (Hogarth et al 2000). The rapid crystallization of fluorapatite would therefore likely be accompanied by rapid crystallization of uranpyrochlore.

5.4 Origin of Uranium and Niobium Mineralization

Detailed petrographic analysis and mineral composition data show that pyrochlore is the principal host for niobium and uranium in all rock types. The pyrochlore is not restricted to the carbonatite, but is present in all rock types. There are however, significant differences between the mineralization styles, and the relative abundance of pyrochlore between different rock types. Most significantly, uranium enrichment in pyrochlore appears to be best developed in siliciocarbonatite, and to a much lesser extent, the potassic fenites.

Sample NLOFR8825b is a siliciocarbonatite that contains clusters of pyrochlore with oscillatory zones of uranoan pyrochlore. These crystals contain abundant textural and geochemical evidence which provides relative insight into the mineralization environment in which they were formed. A very detailed study of primary zoning and secondary alteration features in pyrochlore was carried out on samples from ten different carbonatite complexes by Hogarth, Williams and Jones (2000). Their textural criteria are here applied to pyrochlore from the Lofdal complex.

Primary zonation in pyrochlore is characterized by a systematic compositional variation from core to rim, with the development of very narrow, smooth and well defined oscillatory zones parallel to the {111} crystal face (Hogarth et al., 2000). Secondary features which indicate low-temperature alteration include rims that are discoloured and of an irregular thickness, containing abundant microfractures, bleached zones, and commonly showing evidence of leaching of Na^+, F^- and Ca^{2+} with an associated increase in A-site vacancies (Hogarth et al., 2000). A third feature common among many samples of pyrochlore is metamict crystal structure, related to radioactive U and Th which produces syneresis cracks, and generates significant A and Z-site vacancies (Hogarth et al., 2000).

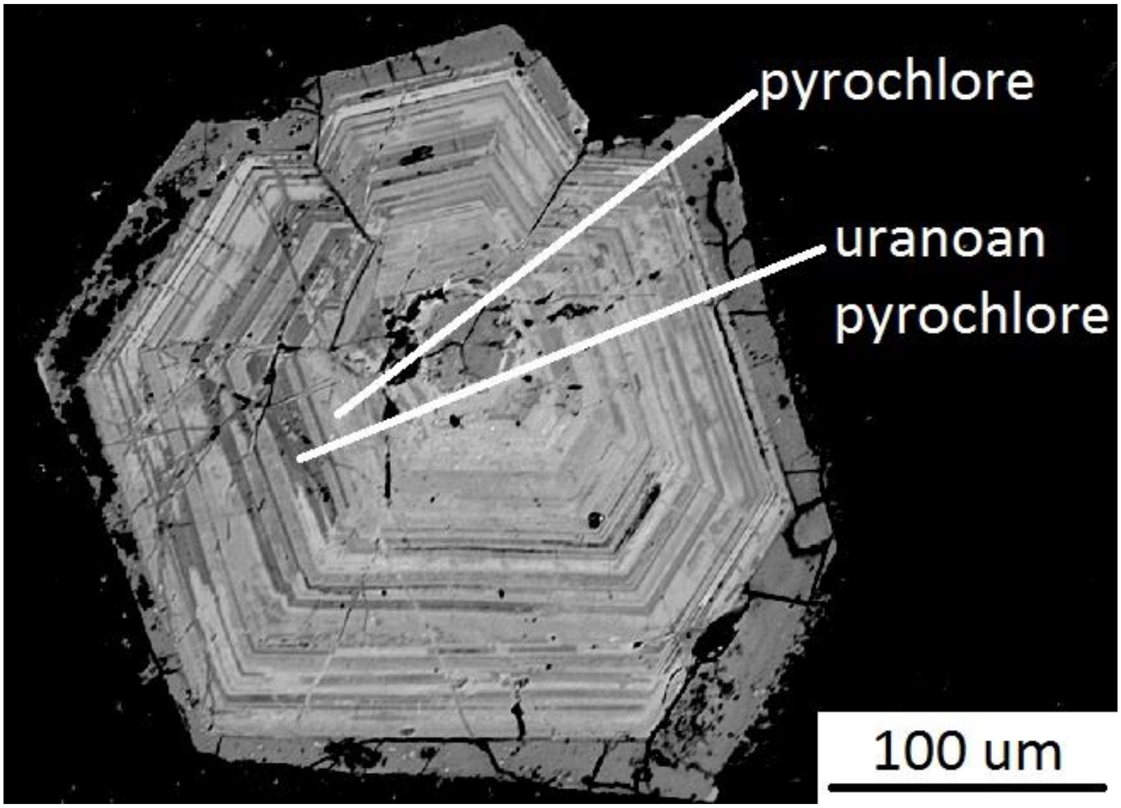

Figure 5.3 – Oscillatory zoned pyrochlore from sample NLOFR8825b. Textural evidence suggest that the smooth oscillatory zones formed from a magma in a tranquil environment, supersaturated in Nb, Ta, U and Si, with U and Si reaching periodic supersaturation. Lighter zones correspond to simple pyrochlore while darker zones correspond to uranoan pyrochlore.

Pyrochlore from sample NLOFR8825b (*Figure 5.3*) shows well defined, smooth, and narrow oscillatory zones parallel to the {111} crystal face. These zones are characterized by two compositions: pyrochlore and uranoan pyrochlore. Uranoan pyrochlore zones also contain elevated Si and Fe content. These narrow oscillatory zones are interpreted to suggest that the melt in which these crystals grew was tranquil, supersaturated with respect to Nb and Ta, and significantly enriched in U and Si. Periodically, supercritical saturation of U and Si was reached, and these elements were able to nucleate on existing pyrochlore grains (Hogarth et al 2000). It is therefore interpreted that the inner cores of nearly all pyrochlores in siliciocarbonatites are primary magmatic in origin.

The rims of many of these pyrochlore minerals appear quite different on the basis of both texture and composition. In *Figure 5.4*, crystals (C) and (D) show evidence of secondary processes, with compositionally distinct irregular outer grains that appear to cross-cut the oscillatory zones of the primary inner pyrochlore crystal. However, crystals (A) and (B) show an outer rim composition with irregular outer grain boundaries and abundant micro fractures, but with smooth inner grain boundaries which do not seem to alter the inner crystal structure.

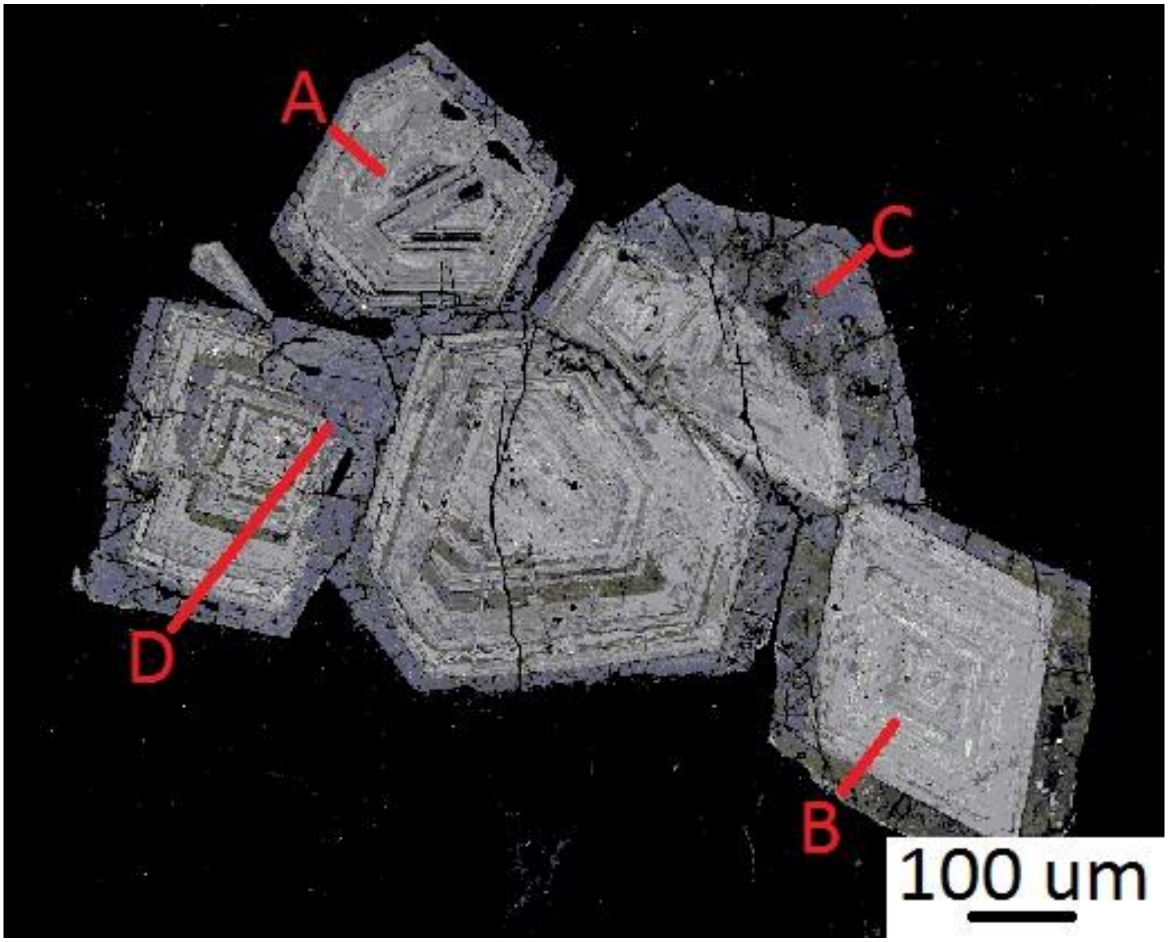

***Figure* 5.4 – Pyrochlore crystal cluster from sample NLOFR8825b from which element distribution X-ray maps were produced. Crystals A and B clearly indicate a primary magmatic inner crystal, with a second growth composition likely resulting from a late magmatic growth in a very volatile fluid rich environment. Crystals C and D show a similar texture with minor alteration texture, likely also the result of fluid interaction.**

For most pyrochlore occurrences in siliciocarbonatite, the outer rims seem to nucleate along the outer grain boundaries of pyrochlores without dissolution textures. However, although not the dominant texture, dissolution does appear to be present in some crystals. Clearly the crystallization conditions are different in situations that would allow nucleation, and situations that would cause resorption. More importantly, both conditions cannot have been present at the same time. It is therefore likely that between the primary magmatic growth stage and the rapid outer rim growth, equilibrium conditions were disturbed, causing partial resorption of the magmatic pyrochlore crystals. The cause of this change in equilibrium conditions appears to be a highly localized event affecting only a small portion of pyrochlore crystals in siliciocarbonatite. This phase of resorption also appears to have been very brief, affecting only a small portion of the outer crystal rims. It is likely that equilibrium conditions were quickly re-established allowing rapid nucleation of uranoan pyrochlore on pre-existing pyrochlore grains. For the majority of cases though, nucleation of uranoan pyrochlore along smooth euhedral pyrochlore is the norm. In some samples, these outer growth rims become quite large (*Figure 5.6*). This sample shows three or four small oscillatory zoned magmatic pyrochlore crystals in a cluster, all of which have been fully enveloped in an outer growth phase of uranoan pyrochlore. This outer pyrochlore composition matches that of the smaller rim growths observed in the previous sample NLOFR8825b. This uranoanpyrochlore shows a strongly metamict texture, and abundant syneresis cracks. Additionally, fractures in the surrounding aegirine can be seen containing infill of uranoan pyrochlore. The growth of this phase is likely attributable to late magmatic growth in a fluid and volatile rich environment. As the solubility of uranium and niobium rapidly decreased, these elements were forced to nucleate on pre-existing pyrochlore structures.

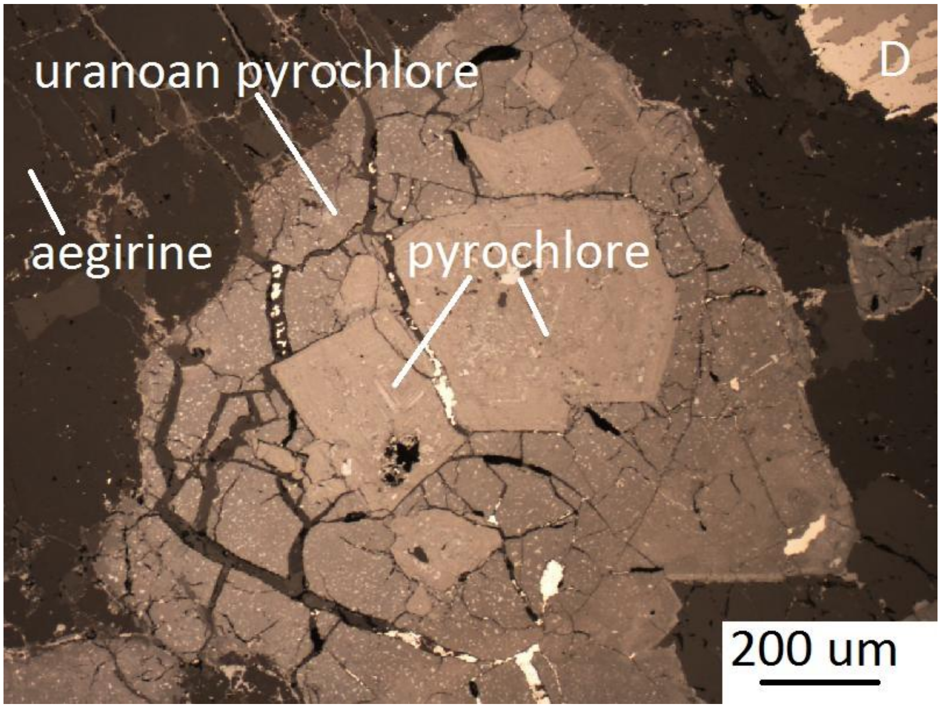

Figure **5.5 – Pyrochlore crystal cluster with extensive rim growth positioned along the margins of a mineralized fracture in sample NLOFR8825b. These rim compositions are strongly metamict and show syneresis cracks. These rims likely grew as a result of volatile precipitation from a CO_2 dominated fluid.**

The cause of this rapid decrease in solubility is likely attributable to a decrease in phosphate and fluoride complexing due to crystallization of fluorapatite as discussed in the previous section. The fact that these elements were forced to nucleate on pre-existing pyrochlore grains, then, is likely due to the presence of volatiles which inhibit growth of new crystals. The variability in primary magmatic pyrochlore growth, followed by this last phase of rapid volatile rich growth of defect pyrochlore, is consistent with siliciocarbonatite textural evidence, all of which suggest that these rocks, and these minerals, formed from a late, silica-rich residual melt in the presence of a fluid phase.

In a study by Mitchell and Zurevinski (2004) on pyrochlore variation from samples of the Oka carbonatite complex in Quebec, A-site vacancies were used to distinguish primary, hydrothermal and supergene pyrochlore. In accordance with textural criteria (Hogarth et al. 2000), A-site vacancies increase significantly from primary to hydrothermal pyrochlore, and increase further from hydrothermal to supergene pyrochlore. Hydrothermal pyrochlore is also characterized by significant leaching of Na and Ca. *Figure 5.6* shows the results of pyrochlore WDS analyses collected in this study, plotted on a tri-plot of (Na-Ca-A-vacancy). Only WDS analyses with totals between 97.5 % and 101.5 % were included, as totals which are too high or low severely affect the determination of A-site vacancies. Nearly all suitable pyrochlore analyses plot within the magmatic field, with only one outlier present. This outlier comes from a potassic fenite and occurs as an interstitial vein phase. The remaining analyses are a mixture of pyrochlore cores and rims from siliciocarbonatites and potassic fenites.

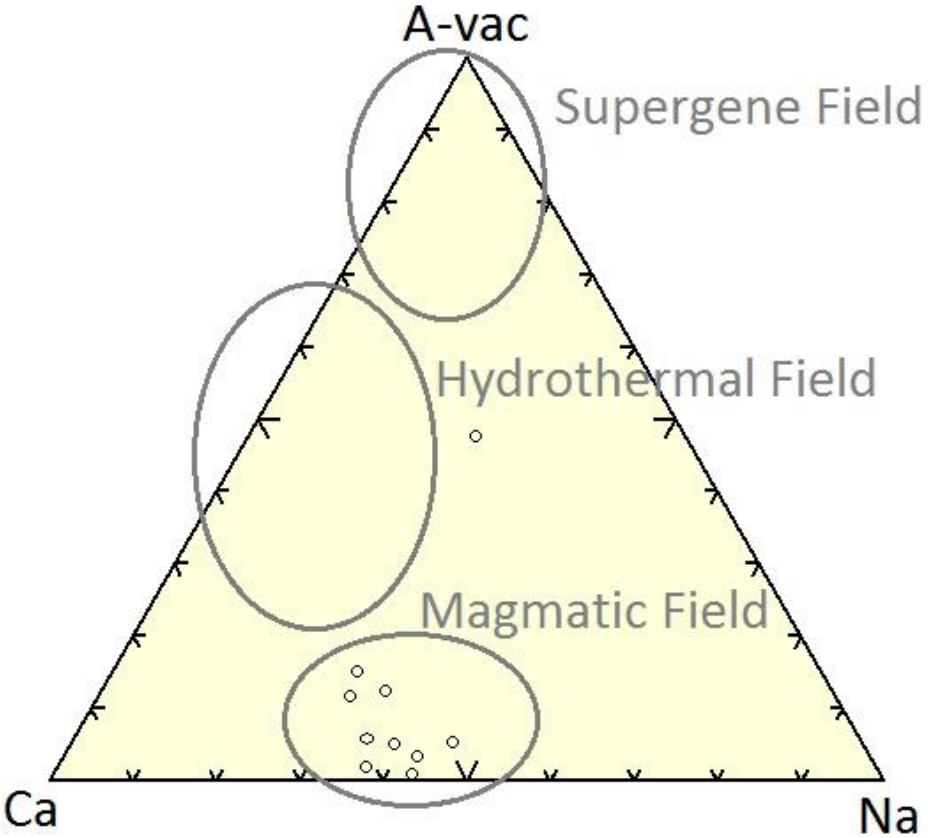

Figure 5.6 – Pyrochlore WDS analysis results plotted on a tri-plot of Na, Ca and A-vacancy distributed between magmatic, hydrothermal and supergene fields.

In order to quantify A-site vacancies, mineral formula calculations for pyrochlore were performed with the assumption that the B-site is always fully occupied according to the unit cell structure $A_2B_2O_6Z$ (Mitchell and Zurevinski 2004). A detailed table of calculations are reported in *Appendix B-2* showing atoms per formula unit normalized to a fully occupied B-site. This calculation provided a value for A-site occupancy which was used to calculate its vacancy. Atoms assigned to the A-site include Ca, Na, REE, U, Th, and Mg. Atoms assigned to the B-site include Ti, Si, Al, Ta, Nb, Zr. All iron is presumed to be present as Fe^{3+} and is also assigned to the B-site. Some A-site occupancy values were calculated to be above 2 (*Appendix B-2*), which is the maximum occupancy for this site. It is proposed that this is a result of overestimation of elemental abundance during WDS analysis, as many of these samples also show totals above 101% for analysis.

5.5 A Genetic Model for the Main intrusion

The following genetic model for the evolutionary history of the Main intrusion is offered on the basis of field observations, mineralogical and textural observations, whole rock geochemistry, and quantitative and qualitative mineral composition data.

During Neoproterozoic rifting between the Congo and Kalahari cratons different degrees of partial melting of a metasomatised HREE enriched mantle source produced a carbonated alkali melt. The primary magma began to ascend into the crust. At this point the two bodies separated into silicate and carbonatitic melt, either through fractionation or immiscibility. The emplacement of the nepheline syenite magma occurred first, forming three or four plugs, followed by extensive phonolite dyking. During the subsequent ascent of the carbonatite magma, brecciation affected nepheline syenites, as well as basement rocks of the HMC. This was followed by the emplacement of two carbonatite plugs and early magmatic release of potassium rich fluids which induced fenitization in an aureole of nepheline syenite surrounding the Main intrusion carbonatite body. The emplacement of carbonatite dykes is spatially very similar to the emplacement of phonolite dykes, and occurred after brecciation and fenitization on the basis of cross-cutting field relationships (*Swinden and Siegfried, 2011*). During crystallization of the carbonatite body, residual silica and volatile-rich magma, and CO_2-rich fluids may have migrated to the margins of the intrusion as evidenced by bands of very fine-grained aegirine and pyrochlore within relatively pure carbonatite. The carbonatite body was characteristically enriched in Nb and U, as evidenced by the presence of these elements in potassic fenites, as well as within oscillatory zones of primary magmatic pyrochlore. However, substantial concentrations of these elements were present within the siliciocarbonatite samples. This suggests that these elements were strongly enriched within the residual melt from which the siliciocarbonatite crystallized. The magmatic history of the Main intrusion appears to have ended with the crystallization of the siliciocarbonatite marginal phase.

5.6 Guidelines for Further Exploration

The exploration strategies for niobium and uranium are slightly different, and as such, exploration recommendations for each will be considered separately. Niobium concentrations in potassic fenites are significant, and in most cases appear to show equal or better enrichment than in siliciocarbonatites. From the limited sample set of potassic fenites in this study, it would appear that a majority of the niobium seems to be mineralized along fractures and grew interstitially with zircon and magnetite. This may pose metallurgical issues as mechanical separation will prove significantly more difficult than if the niobium were crystalized as larger crystals. However, a more complete and detailed study of the fenitization process at the Main intrusion may reveal further controls on niobium mineralization which would allow for more specific targeting techniques. Targeting siliciocarbonatite for niobium may also prove viable, particularly if uranium is desired. Removal of uranium through leaching will be necessary for producing ferroniobate either way, but if uranium is a desired product this will prove more profitable than costly. Targeting of Uranium should be focused on siliciocarbonatite. It appears that uranoan pyrochlore mineralization is always accompanied by abundant aegirine and phosphate, which are the characteristic rock forming minerals of silciocarbonatite. That being said, the siliciocarbonatite may not actually be purely a contact phase with potassic fenites. It is more than likely that the sovite plug of the Main intrusion will not be pure sovite at depth, but rather a significantly complex carbonatite composite. Therefore, strongly aegirine-and apatite-rich zones within drill core will provide high potential targets for sampling. With increased drill holes within the Main intrusion, better structural constraints will be available in support or disproval of the notion of immiscible silicate fluids migrating towards the intrusive margins.

5.7 Suggestions for Further Research

The most significant problem in the Main intrusion that still requires clarification is the origin of the potassic fenites. It is clear that they are geochemically inconsistent, and it has not been determined whether they are the product of one inhomogeneous metasomatic event, or the product of an early homogeneous metasomatic event which has been overprinted by a later inhomogeneous event. A much larger sample set, collected through an unbiased grid sampling method would provide the necessary data to better characterize the fenitization process. Given that significant niobium enrichment was encountered in the potassic fenites, understanding this process will lead to better constraints on mineralization.

Chapter 6: Conclusions

1. Niobium mineralization is most prominent in potassic fenites and siliciocarbonatites, while uranium mineralization is constrained mainly to siliciocarbonatites. In both rock types, pyrochlore is the principal host mineral for both elements.
2. Pyrochlore core and rim compositions are interpreted to both be magmatic. The cores are interpreted to have formed in a tranquil magmatic environment, supersaturated in Nb, Ca, Na, U, and Si. Periodic super-saturation is interpreted to be responsible for the development of narrow oscillatory zones characterized by significant quantities of U and Si. The outer rims of uranoan pyrochlore and uranpyrochlore encountered in siliciocarbonatites are believed to be magmatic rather than hydrothermal.
3. Siliciocarbonatite appears to be a magmatic phase which crystallized from residual carbonatite magma, rich in silica and volatiles, producing significant quantities of aegirine, apatite, carbonate and pyrochlore. This lithology appears to be most predominant along the margins of the intrusion.
4. Crystallization of fluorapatite in siliciocarbonatite is interpreted to have enhanced rapid pyrochlore rim crystallization by reducing the solubility of uranium and niobium through a reduction of fluorine and phosphate complexing capacity.
5. On the basis of REE mantle signatures, the nepheline syenite and carbonatite bodies are likely to be genetically related, sharing a common HREE, Nb and U-enriched metasomatised mantle source.
6. Potassic fenites are metasomatic in origin, forming from a nepheline syenite protolith. This lithology is most likely the product of an early potassium-rich metasomatism, which was heterogeneously overprinted by a later calcium and sodium rich alteration event. However, further research is required to resolve this issue.

References

Atencio, D., Andrade, M.B., Christy, A.G., Gieré, R., Kartashov., 2010. The Pyrochlore Supergroup of Minerals: Nomenclature. *The Canadian Mineralogist*, Vol. 48, pp. 673-698.

Castor, S.B., 2008. Rare Earth Deposits of North America. *Resource Geology*, Vol. 58, pp. 337-347.

Frets, D. C., 1969. Geology and structure of the Huab-Welwitschia area. South West Africa, Chamber of Mines, Precambrian Research Unit: University of Capetown Libraries. 235 p.

Geological Survey of Namibia, 2002. Simplified Geological Map of Namibia. www.mme.gov.na/gsn/simplegeomap.html. Downloaded Mar. 16, 2012.

Gieré, R., 1996. Formation of rare earth minerals in hydrothermal systems. *In: Jones AP, Wall F, Williams T (eds)* Rare Earth Minerals: Chemistry, Origin and Ore Deposits. *Mineralogical Society, Series 7.* pp: 105-150.

Goodge, J., 2012a. Electron probe micro-analyzer (EPMA). *SERC*. Retrieved March 16, 2013, from http://serc.carleton.edu/research_education/geochemsheets/techniques/EPMA.html

Goodge, J., 2012b. Energy-dispersive detector (EDS). *SERC*. Retrieved March 16, 2013, from http://serc.carleton.edu/research_education/geochemsheets/eds.html

Goodge, J., 2012c. Element mapping. *SERC*. Retrieved March 16, 2013, from http://serc.carleton.edu/research_education/geochemsheets/elementmapping.html

Goodge, J., & Henry, D., 2012. Wavelength-dispersive spectroscopy (WDS). *SERC*. Retrieved March 16, 2013, from http://serc.carleton.edu/research_education/geochemsheets/wds.html

Goodge, J., Henry, D., Eby, N., & Mogk, D., 2012. BraggsLaw. *SERC*. Retrieved March 16, 2013, from http://serc.carleton.edu/research_education/geochemsheets/BraggsLaw.html

Henderson, P., 1996. The rare earth elements: introduction and review. *In Jones AP, Wall F, Williams T (eds)* Rare Earth Minerals: Chemistry, Origin and Ore Deposits. *Mineralogical Society, Series 7,* pp. 1-20.

Hendersen, S.J., Shebanova, O., Hector, A.L., McMillan, P.F., Weller, M.T., 2007. Structural Variations in Pyrochlore-Structured Bi2Hf2O7, Bi2Ti2O7 and Bi2Hf2-xTixo7 Solid Solutions as a Function of Composition and Temperature by Neutron and X-ray Diffraction and Raman Spectroscopy. *Chemistry of Materials*, Vol. 19, pp. 1712-1722.

Hoffman, P.E., Hawkins, D.P., Isachsen, C.E., and Bowering, S.A. 1996. Precise U-Pb zircon ages for early Damaran magmatism in the Summas Mountains and Welwitschia Inlier, northern Damara belt, Namibia*. Communication of the Geological Survey of Namibia*, Vol. 11, pp. 47-52.

Hogarth, D.D., 1989. Pyrochlore, Apatite, and Amphibole: Distinctive Minerals in Carbonatite. In Bell, K. (ed) Carbonatites: Genesis and Evolution. *Unwin Hyman Ltd*., London. pp. 105-149.

Hogarth, D.D., Williams, C.T., Jones, P., 2000. Primary zoning in pyrochlore group minerals from carbonatites. *Mineralogical Magazine*, Vol. 64(4), pp. 683-697.

Holm, P.E., 1985. The geochemical fingerprints of different tectonomagmatic environments using hygramagmatopgile element abundances of tholeiitic basalts and basaltic andesites. *Chemical Geology*, Vol. 51, pp. 303-323.

Jung, S., Hoffer, E., Hoernes, S., 2006. Neo-Proterozoic rift-related syenites (northern Damara belt, Namibia): Geochemical and Nd-Sr-Pb-O isotope constraints for mantle sources and petrogenesis , *Lithos*, Vol. 96, pp.415-435.

Van Groos, Koster A. F., Wyllie, P. J., 1966. Liquid Immiscibility in the System Na_2O-Al_2O_3-SiO_2-CO_2 at Pressures to 1 Kilobar. *American Journal of Science*, Vol. 264, March 1966, pp. 234-255.

Le Bas, M.J., 2008. Fenites Associated with Carbonatites. *The Canadian Mineralogist,* Vol. 46, pp. 915-932.

Le Maitre, R.W., 2002. Igneous Rocks: A Classification and Glossary of Terms (2nd Edition). Great Britain: *Cambridge University Press*, pp. 10.

Mariano, A.N., 1989. Nature of economic mineralization in carbonatites and related rocks. *In Bell, K (ed)* Carbonatites: Genesis and Evolution. *Unwin Hyman Ltd*., London. pp. 149-177.

Mitchell, R.H., Zurevinski, S.E., 2004. Extreme compositional variation of pyrochlore-group minerals at the Oka carbonatite complex, Quebec: Evidence of magma mixing? *The Canadian Mineralogist*, Vol. 42, pp. 1159-1168.

Namibia Rare Earths Ltd., 2011. Unpublished geological map of the Lofdal area

O'Connor, D. 2010. Petrogenesis of Nepheline Syenites and Phonolites from the Lofdal Intrusive Complex, Kunene Region, Namibia. *Unpublished Bachelors Thesis*., Dalhousie University, Halifax, Ns, 103p.

Schneider, G., 2008. The Roadside Geology of Namibia, 2nd Edition*, Gebruder Borntaeger Stuttgart*, Germany. 294p.

Swinden, H.S., Siegfried, P., 2011. Amended 43-101 Technical Report on the Rare Earth Element Occurrences in the Lofdal Carbonatite Complex, Kunene Region, Khorixas District, Namibia. Halifax,. *Unpublished report for Namibia Rare Earths Ltd*., Halifax, Ns. 210p.

Swinden, H. S., 2012. Preliminary Report on Geological Mapping in Area 7, Lofdal Property, and Recommendations for Further Work. *Unpublished report for Namibia Rare Earths Ltd.*, 14 p.

Winter, J.D., 2010. Principles of Igneous and Metamorphic Petrology (2nd Edition). *Pearson Education Inc.*, pp. 409-420.

Woolley, A. R., and D. R. C. Kempe., 1989.Carbonatites: nomenclature, average chemical compositions, and element distribution. *In Bell, K (ed)* Carbonatites: Genesis and Evolution. *Unwin Hyman, London*. pp. 1-14.

Woolley, A.R., Kjarsgaard, B.A., 2008. Paragenetic types of carbonatite as indicated by the diversity and relative abundance of associated silicate rocks: evidence from a global database. *The Canadian Mineralogist*, Vol. 4, pp. 741-752.

Wyllie, P., Tuttle, O., 1960. The System CaO-CO_2-H_2O and the Origin of Carbonatites. *Journal of Petrology*, vol: 1, pp. 1-46.

Appendix A-1

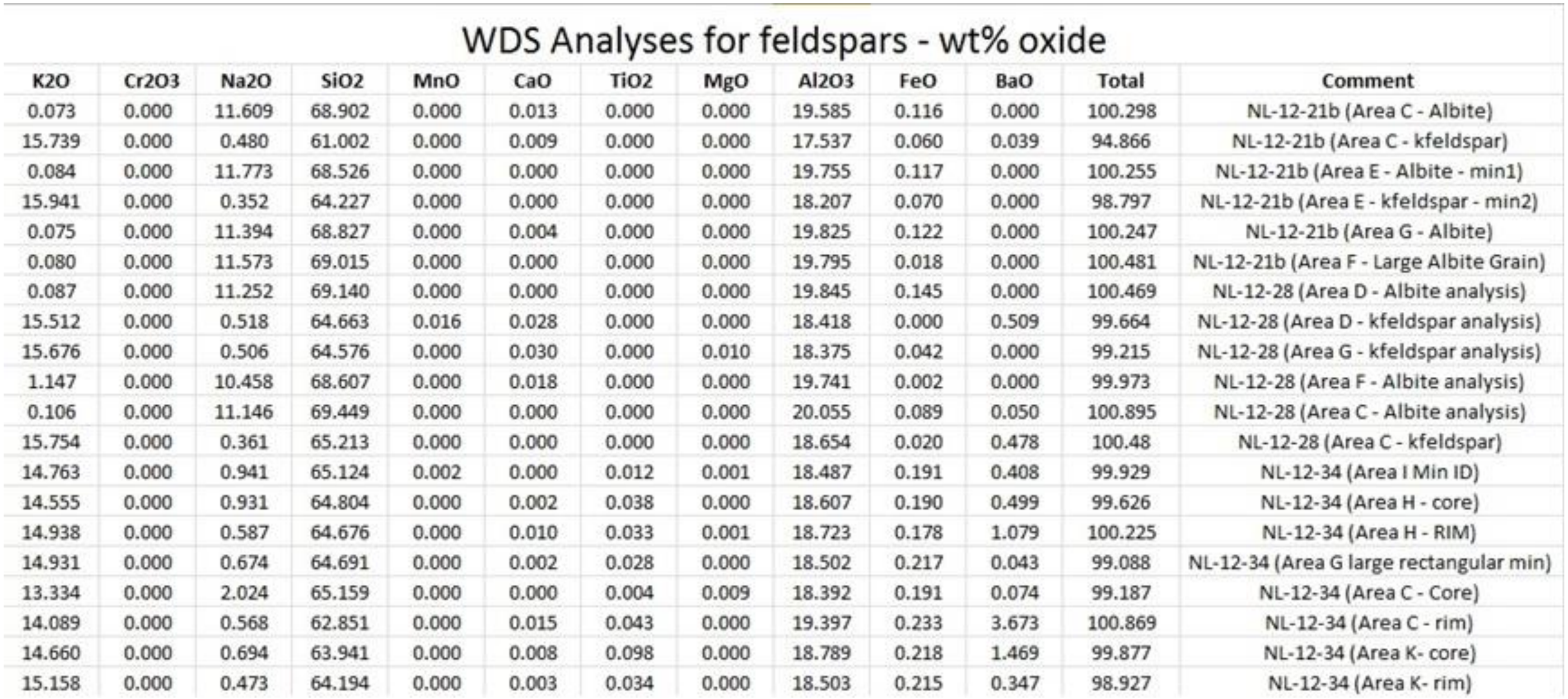

WDS Analyses for feldspars - wt% oxide

K2O	Cr2O3	Na2O	SiO2	MnO	CaO	TiO2	MgO	Al2O3	FeO	BaO	Total	Comment
0.073	0.000	11.609	68.902	0.000	0.013	0.000	0.000	19.585	0.116	0.000	100.298	NL-12-21b (Area C - Albite)
15.739	0.000	0.480	61.002	0.000	0.009	0.000	0.000	17.537	0.060	0.039	94.866	NL-12-21b (Area C - kfeldspar)
0.084	0.000	11.773	68.526	0.000	0.000	0.000	0.000	19.755	0.117	0.000	100.255	NL-12-21b (Area E - Albite - min1)
15.941	0.000	0.352	64.227	0.000	0.000	0.000	0.000	18.207	0.070	0.000	98.797	NL-12-21b (Area E - kfeldspar - min2)
0.075	0.000	11.394	68.827	0.000	0.004	0.000	0.000	19.825	0.122	0.000	100.247	NL-12-21b (Area G - Albite)
0.080	0.000	11.573	69.015	0.000	0.000	0.000	0.000	19.795	0.018	0.000	100.481	NL-12-21b (Area F - Large Albite Grain)
0.087	0.000	11.252	69.140	0.000	0.000	0.000	0.000	19.845	0.145	0.000	100.469	NL-12-28 (Area D - Albite analysis)
15.512	0.000	0.518	64.663	0.016	0.028	0.000	0.000	18.418	0.000	0.509	99.664	NL-12-28 (Area D - kfeldspar analysis)
15.676	0.000	0.506	64.576	0.000	0.030	0.000	0.010	18.375	0.042	0.000	99.215	NL-12-28 (Area G - kfeldspar analysis)
1.147	0.000	10.458	68.607	0.000	0.018	0.000	0.000	19.741	0.002	0.000	99.973	NL-12-28 (Area F - Albite analysis)
0.106	0.000	11.146	69.449	0.000	0.000	0.000	0.000	20.055	0.089	0.050	100.895	NL-12-28 (Area C - Albite analysis)
15.754	0.000	0.361	65.213	0.000	0.000	0.000	0.000	18.654	0.020	0.478	100.48	NL-12-28 (Area C - kfeldspar)
14.763	0.000	0.941	65.124	0.002	0.000	0.012	0.001	18.487	0.191	0.408	99.929	NL-12-34 (Area I Min ID)
14.555	0.000	0.931	64.804	0.000	0.002	0.038	0.000	18.607	0.190	0.499	99.626	NL-12-34 (Area H - core)
14.938	0.000	0.587	64.676	0.000	0.010	0.033	0.001	18.723	0.178	1.079	100.225	NL-12-34 (Area H - RIM)
14.931	0.000	0.674	64.691	0.000	0.002	0.028	0.000	18.502	0.217	0.043	99.088	NL-12-34 (Area G large rectangular min)
13.334	0.000	2.024	65.159	0.000	0.000	0.004	0.009	18.392	0.191	0.074	99.187	NL-12-34 (Area C - Core)
14.089	0.000	0.568	62.851	0.000	0.015	0.043	0.000	19.397	0.233	3.673	100.869	NL-12-34 (Area C - rim)
14.660	0.000	0.694	63.941	0.000	0.008	0.098	0.000	18.789	0.218	1.469	99.877	NL-12-34 (Area K- core)
15.158	0.000	0.473	64.194	0.000	0.003	0.034	0.000	18.503	0.215	0.347	98.927	NL-12-34 (Area K- rim)

WDS Analyses for Feldspars – Oxide data

Appendix A-2

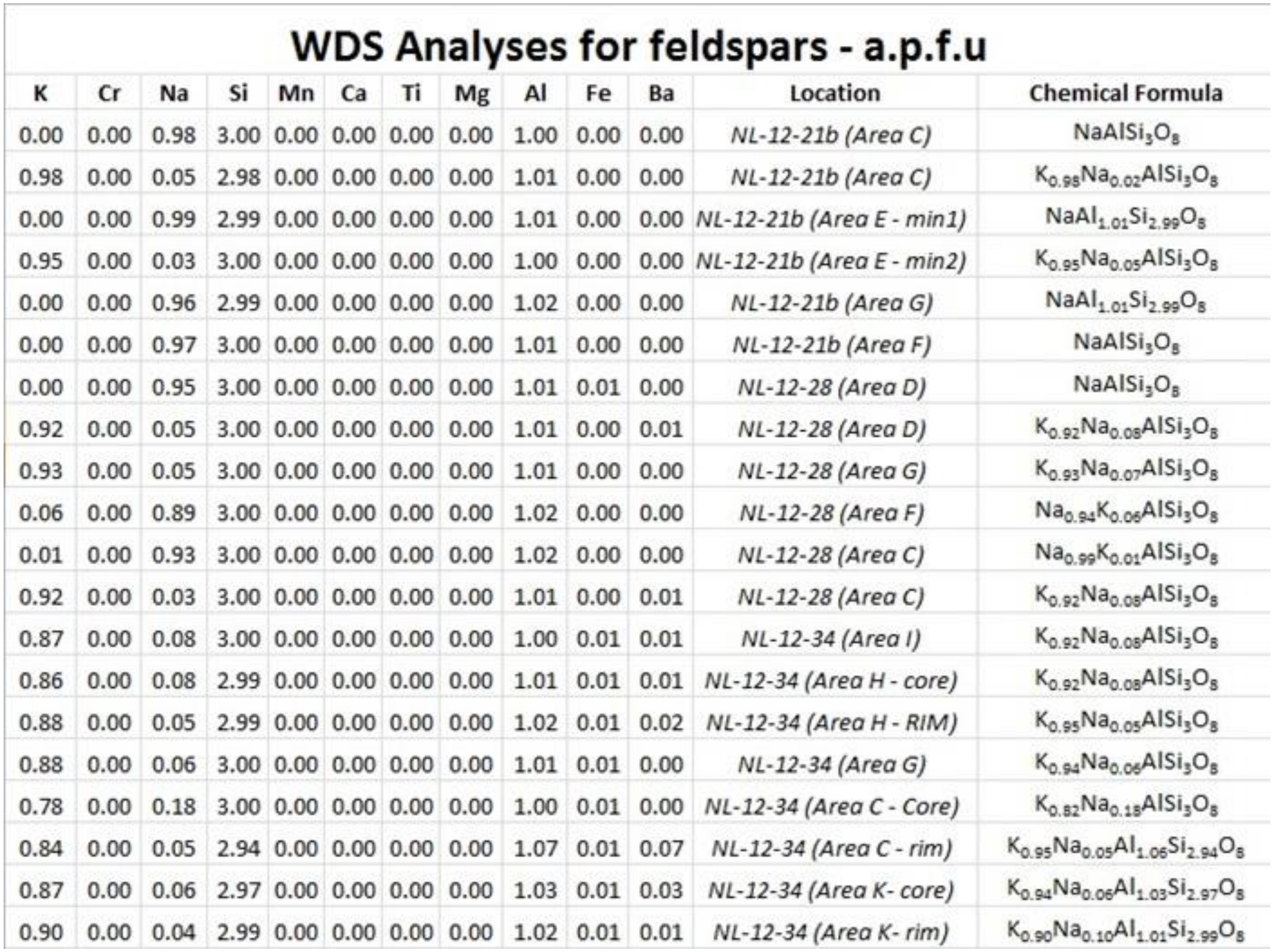

WDS Analyses for feldspars - a.p.f.u

K	Cr	Na	Si	Mn	Ca	Ti	Mg	Al	Fe	Ba	Location	Chemical Formula
0.00	0.00	0.98	3.00	0.00	0.00	0.00	0.00	1.00	0.00	0.00	*NL-12-21b (Area C)*	$NaAlSi_3O_8$
0.98	0.00	0.05	2.98	0.00	0.00	0.00	0.00	1.01	0.00	0.00	*NL-12-21b (Area C)*	$K_{0.98}Na_{0.02}AlSi_3O_8$
0.00	0.00	0.99	2.99	0.00	0.00	0.00	0.00	1.01	0.00	0.00	*NL-12-21b (Area E - min1)*	$NaAl_{1.01}Si_{2.99}O_8$
0.95	0.00	0.03	3.00	0.00	0.00	0.00	0.00	1.00	0.00	0.00	*NL-12-21b (Area E - min2)*	$K_{0.95}Na_{0.05}AlSi_3O_8$
0.00	0.00	0.96	2.99	0.00	0.00	0.00	0.00	1.02	0.00	0.00	*NL-12-21b (Area G)*	$NaAl_{1.01}Si_{2.99}O_8$
0.00	0.00	0.97	3.00	0.00	0.00	0.00	0.00	1.01	0.00	0.00	*NL-12-21b (Area F)*	$NaAlSi_3O_8$
0.00	0.00	0.95	3.00	0.00	0.00	0.00	0.00	1.01	0.01	0.00	*NL-12-28 (Area D)*	$NaAlSi_3O_8$
0.92	0.00	0.05	3.00	0.00	0.00	0.00	0.00	1.01	0.00	0.01	*NL-12-28 (Area D)*	$K_{0.92}Na_{0.08}AlSi_3O_8$
0.93	0.00	0.05	3.00	0.00	0.00	0.00	0.00	1.01	0.00	0.00	*NL-12-28 (Area G)*	$K_{0.93}Na_{0.07}AlSi_3O_8$
0.06	0.00	0.89	3.00	0.00	0.00	0.00	0.00	1.02	0.00	0.00	*NL-12-28 (Area F)*	$Na_{0.94}K_{0.06}AlSi_3O_8$
0.01	0.00	0.93	3.00	0.00	0.00	0.00	0.00	1.02	0.00	0.00	*NL-12-28 (Area C)*	$Na_{0.99}K_{0.01}AlSi_3O_8$
0.92	0.00	0.03	3.00	0.00	0.00	0.00	0.00	1.01	0.00	0.01	*NL-12-28 (Area C)*	$K_{0.92}Na_{0.08}AlSi_3O_8$
0.87	0.00	0.08	3.00	0.00	0.00	0.00	0.00	1.00	0.01	0.01	*NL-12-34 (Area I)*	$K_{0.92}Na_{0.08}AlSi_3O_8$
0.86	0.00	0.08	2.99	0.00	0.00	0.00	0.00	1.01	0.01	0.01	*NL-12-34 (Area H - core)*	$K_{0.92}Na_{0.08}AlSi_3O_8$
0.88	0.00	0.05	2.99	0.00	0.00	0.00	0.00	1.02	0.01	0.02	*NL-12-34 (Area H - RIM)*	$K_{0.95}Na_{0.05}AlSi_3O_8$
0.88	0.00	0.06	3.00	0.00	0.00	0.00	0.00	1.01	0.01	0.00	*NL-12-34 (Area G)*	$K_{0.94}Na_{0.06}AlSi_3O_8$
0.78	0.00	0.18	3.00	0.00	0.00	0.00	0.00	1.00	0.01	0.00	*NL-12-34 (Area C - Core)*	$K_{0.82}Na_{0.18}AlSi_3O_8$
0.84	0.00	0.05	2.94	0.00	0.00	0.00	0.00	1.07	0.01	0.07	*NL-12-34 (Area C - rim)*	$K_{0.95}Na_{0.05}Al_{1.06}Si_{2.94}O_8$
0.87	0.00	0.06	2.97	0.00	0.00	0.00	0.00	1.03	0.01	0.03	*NL-12-34 (Area K- core)*	$K_{0.94}Na_{0.06}Al_{1.03}Si_{2.97}O_8$
0.90	0.00	0.04	2.99	0.00	0.00	0.00	0.00	1.02	0.01	0.01	*NL-12-34 (Area K- rim)*	$K_{0.90}Na_{0.10}Al_{1.01}Si_{2.99}O_8$

WDS Results for Feldspars – Mineral formula calculations

Appendix B-1

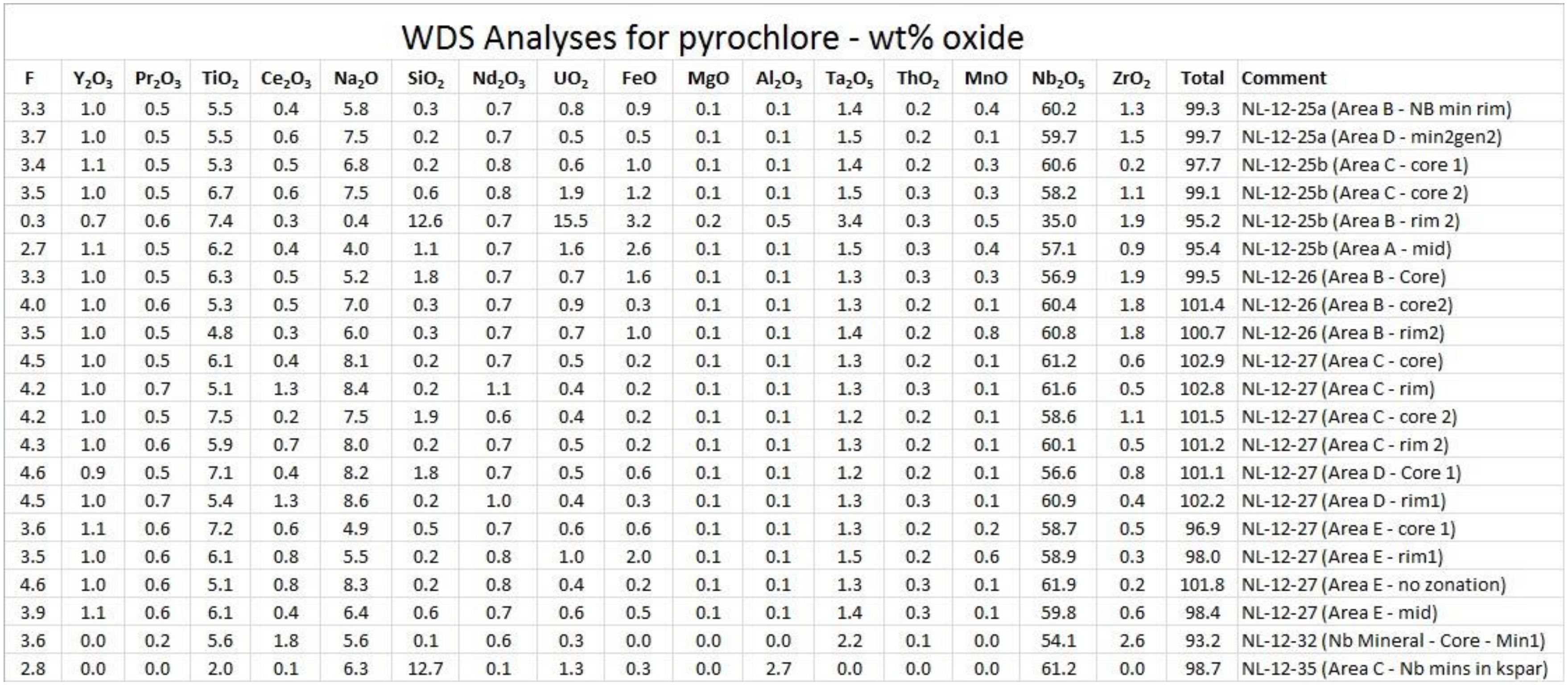

WDS Analyses for pyrochlore - wt% oxide

F	Y_2O_3	Pr_2O_3	TiO_2	Ce_2O_3	Na_2O	SiO_2	Nd_2O_3	UO_2	FeO	MgO	Al_2O_3	Ta_2O_5	ThO_2	MnO	Nb_2O_5	ZrO_2	Total	Comment
3.3	1.0	0.5	5.5	0.4	5.8	0.3	0.7	0.8	0.9	0.1	0.1	1.4	0.2	0.4	60.2	1.3	99.3	NL-12-25a (Area B - NB min rim)
3.7	1.0	0.5	5.5	0.6	7.5	0.2	0.7	0.5	0.5	0.1	0.1	1.5	0.2	0.1	59.7	1.5	99.7	NL-12-25a (Area D - min2gen2)
3.4	1.1	0.5	5.3	0.5	6.8	0.2	0.8	0.6	1.0	0.1	0.1	1.4	0.2	0.3	60.6	0.2	97.7	NL-12-25b (Area C - core 1)
3.5	1.0	0.5	6.7	0.6	7.5	0.6	0.8	1.9	1.2	0.1	0.1	1.5	0.3	0.3	58.2	1.1	99.1	NL-12-25b (Area C - core 2)
0.3	0.7	0.6	7.4	0.3	0.4	12.6	0.7	15.5	3.2	0.2	0.5	3.4	0.3	0.5	35.0	1.9	95.2	NL-12-25b (Area B - rim 2)
2.7	1.1	0.5	6.2	0.4	4.0	1.1	0.7	1.6	2.6	0.1	0.1	1.5	0.3	0.4	57.1	0.9	95.4	NL-12-25b (Area A - mid)
3.3	1.0	0.5	6.3	0.5	5.2	1.8	0.7	0.7	1.6	0.1	0.1	1.3	0.3	0.3	56.9	1.9	99.5	NL-12-26 (Area B - Core)
4.0	1.0	0.6	5.3	0.5	7.0	0.3	0.7	0.9	0.3	0.1	0.1	1.3	0.2	0.1	60.4	1.8	101.4	NL-12-26 (Area B - core2)
3.5	1.0	0.5	4.8	0.3	6.0	0.3	0.7	0.7	1.0	0.1	0.1	1.4	0.2	0.8	60.8	1.8	100.7	NL-12-26 (Area B - rim2)
4.5	1.0	0.5	6.1	0.4	8.1	0.2	0.7	0.5	0.2	0.1	0.1	1.3	0.2	0.1	61.2	0.6	102.9	NL-12-27 (Area C - core)
4.2	1.0	0.7	5.1	1.3	8.4	0.2	1.1	0.4	0.2	0.1	0.1	1.3	0.3	0.1	61.6	0.5	102.8	NL-12-27 (Area C - rim)
4.2	1.0	0.5	7.5	0.2	7.5	1.9	0.6	0.4	0.2	0.1	0.1	1.2	0.2	0.1	58.6	1.1	101.5	NL-12-27 (Area C - core 2)
4.3	1.0	0.6	5.9	0.7	8.0	0.2	0.7	0.5	0.2	0.1	0.1	1.3	0.2	0.1	60.1	0.5	101.2	NL-12-27 (Area C - rim 2)
4.6	0.9	0.5	7.1	0.4	8.2	1.8	0.7	0.5	0.6	0.1	0.1	1.2	0.2	0.1	56.6	0.8	101.1	NL-12-27 (Area D - Core 1)
4.5	1.0	0.7	5.4	1.3	8.6	0.2	1.0	0.4	0.3	0.1	0.1	1.3	0.3	0.1	60.9	0.4	102.2	NL-12-27 (Area D - rim1)
3.6	1.1	0.6	7.2	0.6	4.9	0.5	0.7	0.6	0.6	0.1	0.1	1.3	0.2	0.2	58.7	0.5	96.9	NL-12-27 (Area E - core 1)
3.5	1.0	0.6	6.1	0.8	5.5	0.2	0.8	1.0	2.0	0.1	0.1	1.5	0.2	0.6	58.9	0.3	98.0	NL-12-27 (Area E - rim1)
4.6	1.0	0.6	5.1	0.8	8.3	0.2	0.8	0.4	0.2	0.1	0.1	1.3	0.3	0.1	61.9	0.2	101.8	NL-12-27 (Area E - no zonation)
3.9	1.1	0.6	6.1	0.4	6.4	0.6	0.7	0.6	0.5	0.1	0.1	1.4	0.3	0.1	59.8	0.6	98.4	NL-12-27 (Area E - mid)
3.6	0.0	0.2	5.6	1.8	5.6	0.1	0.6	0.3	0.0	0.0	0.0	2.2	0.1	0.0	54.1	2.6	93.2	NL-12-32 (Nb Mineral - Core - Min1)
2.8	0.0	0.0	2.0	0.1	6.3	12.7	0.1	1.3	0.3	0.0	2.7	0.0	0.0	0.0	61.2	0.0	98.7	NL-12-35 (Area C - Nb mins in kspar)

WDS Analyses for Pyrochlore – Oxide Data

Appendix B-2

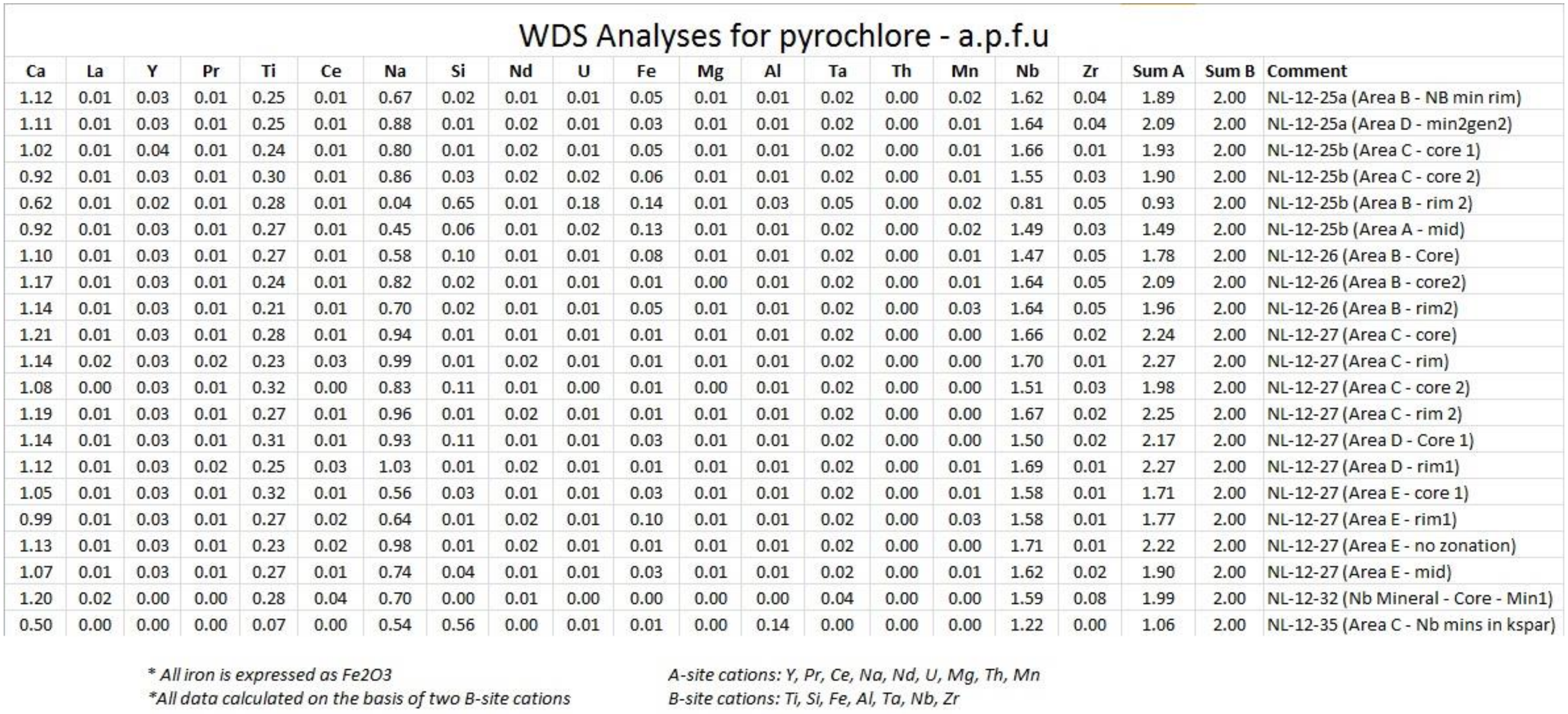

WDS Analyses for pyrochlore - a.p.f.u

Ca	La	Y	Pr	Ti	Ce	Na	Si	Nd	U	Fe	Mg	Al	Ta	Th	Mn	Nb	Zr	Sum A	Sum B	Comment
1.12	0.01	0.03	0.01	0.25	0.01	0.67	0.02	0.01	0.01	0.05	0.01	0.01	0.02	0.00	0.02	1.62	0.04	1.89	2.00	NL-12-25a (Area B - NB min rim)
1.11	0.01	0.03	0.01	0.25	0.01	0.88	0.01	0.02	0.01	0.03	0.01	0.01	0.02	0.00	0.01	1.64	0.04	2.09	2.00	NL-12-25a (Area D - min2gen2)
1.02	0.01	0.04	0.01	0.24	0.01	0.80	0.01	0.02	0.01	0.05	0.01	0.01	0.02	0.00	0.01	1.66	0.01	1.93	2.00	NL-12-25b (Area C - core 1)
0.92	0.01	0.03	0.01	0.30	0.01	0.86	0.03	0.02	0.02	0.06	0.01	0.01	0.02	0.00	0.01	1.55	0.03	1.90	2.00	NL-12-25b (Area C - core 2)
0.62	0.01	0.02	0.01	0.28	0.01	0.04	0.65	0.01	0.18	0.14	0.01	0.03	0.05	0.00	0.02	0.81	0.05	0.93	2.00	NL-12-25b (Area B - rim 2)
0.92	0.01	0.03	0.01	0.27	0.01	0.45	0.06	0.01	0.02	0.13	0.01	0.01	0.02	0.00	0.02	1.49	0.03	1.49	2.00	NL-12-25b (Area A - mid)
1.10	0.01	0.03	0.01	0.27	0.01	0.58	0.10	0.01	0.01	0.08	0.01	0.01	0.02	0.00	0.01	1.47	0.05	1.78	2.00	NL-12-26 (Area B - Core)
1.17	0.01	0.03	0.01	0.24	0.01	0.82	0.02	0.01	0.01	0.01	0.00	0.01	0.02	0.00	0.01	1.64	0.05	2.09	2.00	NL-12-26 (Area B - core2)
1.14	0.01	0.03	0.01	0.21	0.01	0.70	0.02	0.01	0.01	0.05	0.01	0.01	0.02	0.00	0.03	1.64	0.05	1.96	2.00	NL-12-26 (Area B - rim2)
1.21	0.01	0.03	0.01	0.28	0.01	0.94	0.01	0.01	0.01	0.01	0.01	0.01	0.02	0.00	0.00	1.66	0.02	2.24	2.00	NL-12-27 (Area C - core)
1.14	0.02	0.03	0.02	0.23	0.03	0.99	0.01	0.02	0.01	0.01	0.01	0.01	0.02	0.00	0.00	1.70	0.01	2.27	2.00	NL-12-27 (Area C - rim)
1.08	0.00	0.03	0.01	0.32	0.00	0.83	0.11	0.01	0.00	0.01	0.00	0.01	0.02	0.00	0.00	1.51	0.03	1.98	2.00	NL-12-27 (Area C - core 2)
1.19	0.01	0.03	0.01	0.27	0.01	0.96	0.01	0.02	0.01	0.01	0.01	0.01	0.02	0.00	0.00	1.67	0.02	2.25	2.00	NL-12-27 (Area C - rim 2)
1.14	0.01	0.03	0.01	0.31	0.01	0.93	0.11	0.01	0.01	0.03	0.01	0.01	0.02	0.00	0.00	1.50	0.02	2.17	2.00	NL-12-27 (Area D - Core 1)
1.12	0.01	0.03	0.02	0.25	0.03	1.03	0.01	0.02	0.01	0.01	0.01	0.01	0.02	0.00	0.01	1.69	0.01	2.27	2.00	NL-12-27 (Area D - rim1)
1.05	0.01	0.03	0.01	0.32	0.01	0.56	0.03	0.01	0.01	0.03	0.01	0.01	0.02	0.00	0.01	1.58	0.01	1.71	2.00	NL-12-27 (Area E - core 1)
0.99	0.01	0.03	0.01	0.27	0.02	0.64	0.01	0.02	0.01	0.10	0.01	0.01	0.02	0.00	0.03	1.58	0.01	1.77	2.00	NL-12-27 (Area E - rim1)
1.13	0.01	0.03	0.01	0.23	0.02	0.98	0.01	0.02	0.01	0.01	0.01	0.01	0.02	0.00	0.00	1.71	0.01	2.22	2.00	NL-12-27 (Area E - no zonation)
1.07	0.01	0.03	0.01	0.27	0.01	0.74	0.04	0.01	0.01	0.03	0.01	0.01	0.02	0.00	0.01	1.62	0.02	1.90	2.00	NL-12-27 (Area E - mid)
1.20	0.02	0.00	0.00	0.28	0.04	0.70	0.00	0.01	0.00	0.00	0.00	0.00	0.04	0.00	0.00	1.59	0.08	1.99	2.00	NL-12-32 (Nb Mineral - Core - Min1)
0.50	0.00	0.00	0.00	0.07	0.00	0.54	0.56	0.00	0.01	0.01	0.00	0.14	0.00	0.00	0.00	1.22	0.00	1.06	2.00	NL-12-35 (Area C - Nb mins in kspar)

** All iron is expressed as Fe2O3*
**All data calculated on the basis of two B-site cations*

A-site cations: Y, Pr, Ce, Na, Nd, U, Mg, Th, Mn
B-site cations: Ti, Si, Fe, Al, Ta, Nb, Zr

WDS Analyses for Pyrochlore – Mineral site assignments calculated on the basis of full B-site occupancy. All iron considered as Fe^{3+}.

Appendix C

Sample #	Alb	K-fsp	Cal	Nph	Aeg	Biot	Canc	Apat	Mag	Pyro	Accessory Minerals
Nepheline Syenite											
NLOFR8832	6	38	5	10		2	30	1	8		Zrc, nb-rut
NLOFR8834		40	2	10		2	40	3	3		Zrc
NLOFR8841		35	3	15		12	30		5		
Carbonatite											
NLOFR8822			98 dol					2			
NLOFR8827			90		7			1	1	1	rieb
NLOFR8831	1	1	98								pyrite, barite, celestine, cpy, pyrr
NLOFR8837	1	3	93			1		1	1		mon, zrclte
NLOFR8842	5		87			2		1	5		Mon, pyrite, celestine
Siliciocarbonatite											
NLOFR8843	26		37			2		25	8	2	
NLOFR8844	5	23	18		25	2		22	3	2	Ilm
NLOFR8845	3		35		45	2		12	3		mon, rieb
NLOFR8826			10		86	1		trace	trace	3	mon, rut, Ilm
NLOFR8825a			7		84	2		4	1	1	
Potassic Fenite											
NLOFR8821	16	71	8 (vn)		1 (vn)				3	1	mon, columb, ttn, ilm, zrc, zrclte
NLOFR8823	8	79	10						3		columb, Zrc, Zrclte
NLOFR8824	5	82	2 (vn)		10			1	1	1	rut, columb, zrclte
NLOFR8828	12	53	30						1	1	
NLOFR8830	1 (tr)	88	10						2		
NLOFR8835	5	87	3 (vn)						4	1	pyrite, barite
NLOFR8840		66	27			1			6		
NLOFR8836	5	55	30			3			3	1	zrclte, zrc, pyrite
NLOFR8833	5	40	3	tr		trace	40	3	2		
NLOFR8825b	3	85	2		2	2		1	2	3	

Petrographic Summary – Samples are categorized into 4 headings with both the main modal and accessory mineralogy listed for each sample. Alb (Albite), K-fsp (potassium feldspar), Cal (calcite), Nph (nepheline), Aeg (aegirine), Biot (biotite), Canc (cancrinite), Apat (apatite), Mag (magnetite), Pyro (pyrochlore), Zrc (zircon), Nb-rut (niobian rutile), Rieb (riebeckite), mon (monazite), zrclte (zirconolite), cpy (chalcopyrite), pyrr (pyrrhotite), Ilm (ilmenite), columb (columbite), rut (rutile), ttn (titanite),

Appendix D-1

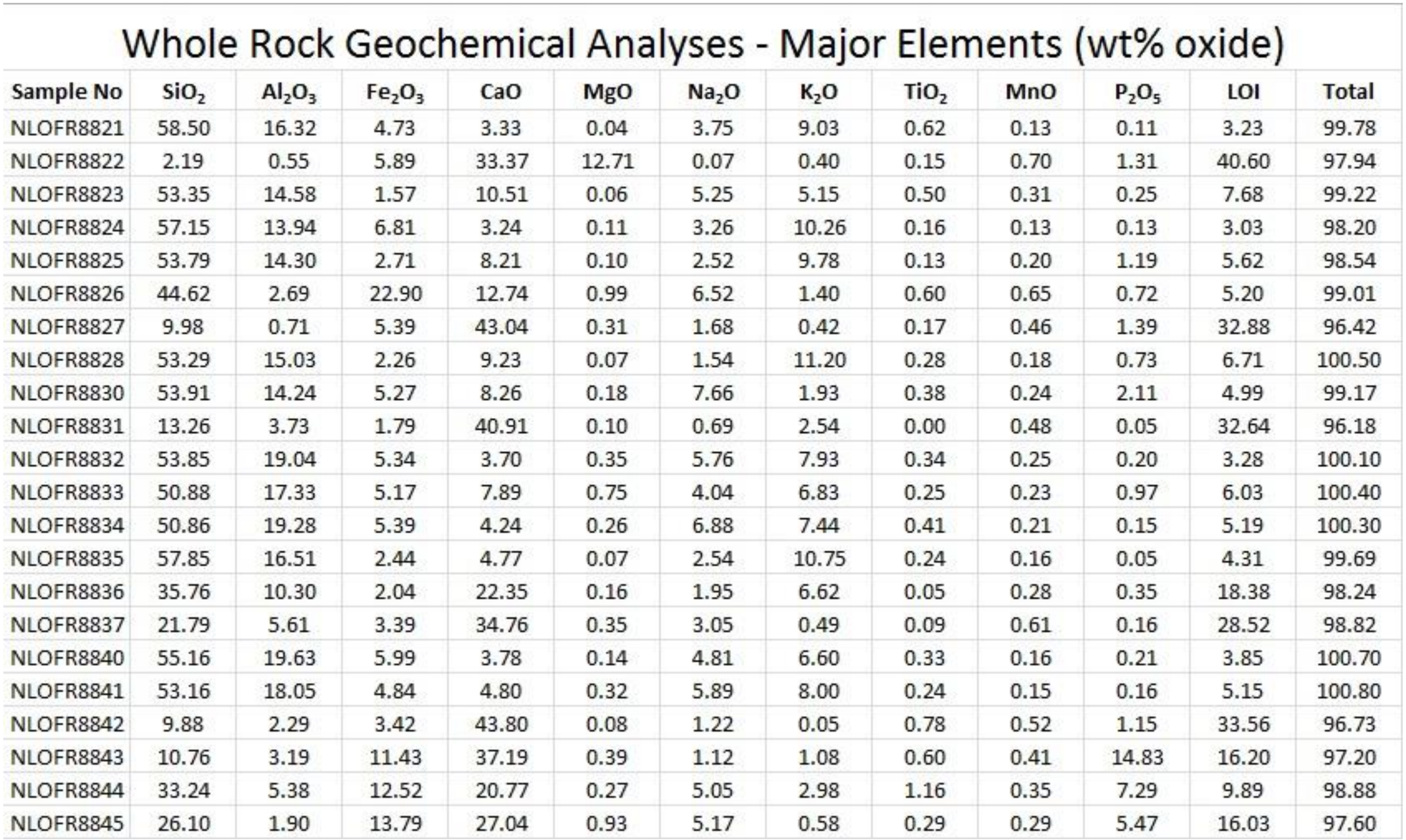

Whole Rock Geochemical Analyses - Major Elements (wt% oxide)

Sample No	SiO_2	Al_2O_3	Fe_2O_3	CaO	MgO	Na_2O	K_2O	TiO_2	MnO	P_2O_5	LOI	Total
NLOFR8821	58.50	16.32	4.73	3.33	0.04	3.75	9.03	0.62	0.13	0.11	3.23	99.78
NLOFR8822	2.19	0.55	5.89	33.37	12.71	0.07	0.40	0.15	0.70	1.31	40.60	97.94
NLOFR8823	53.35	14.58	1.57	10.51	0.06	5.25	5.15	0.50	0.31	0.25	7.68	99.22
NLOFR8824	57.15	13.94	6.81	3.24	0.11	3.26	10.26	0.16	0.13	0.13	3.03	98.20
NLOFR8825	53.79	14.30	2.71	8.21	0.10	2.52	9.78	0.13	0.20	1.19	5.62	98.54
NLOFR8826	44.62	2.69	22.90	12.74	0.99	6.52	1.40	0.60	0.65	0.72	5.20	99.01
NLOFR8827	9.98	0.71	5.39	43.04	0.31	1.68	0.42	0.17	0.46	1.39	32.88	96.42
NLOFR8828	53.29	15.03	2.26	9.23	0.07	1.54	11.20	0.28	0.18	0.73	6.71	100.50
NLOFR8830	53.91	14.24	5.27	8.26	0.18	7.66	1.93	0.38	0.24	2.11	4.99	99.17
NLOFR8831	13.26	3.73	1.79	40.91	0.10	0.69	2.54	0.00	0.48	0.05	32.64	96.18
NLOFR8832	53.85	19.04	5.34	3.70	0.35	5.76	7.93	0.34	0.25	0.20	3.28	100.10
NLOFR8833	50.88	17.33	5.17	7.89	0.75	4.04	6.83	0.25	0.23	0.97	6.03	100.40
NLOFR8834	50.86	19.28	5.39	4.24	0.26	6.88	7.44	0.41	0.21	0.15	5.19	100.30
NLOFR8835	57.85	16.51	2.44	4.77	0.07	2.54	10.75	0.24	0.16	0.05	4.31	99.69
NLOFR8836	35.76	10.30	2.04	22.35	0.16	1.95	6.62	0.05	0.28	0.35	18.38	98.24
NLOFR8837	21.79	5.61	3.39	34.76	0.35	3.05	0.49	0.09	0.61	0.16	28.52	98.82
NLOFR8840	55.16	19.63	5.99	3.78	0.14	4.81	6.60	0.33	0.16	0.21	3.85	100.70
NLOFR8841	53.16	18.05	4.84	4.80	0.32	5.89	8.00	0.24	0.15	0.16	5.15	100.80
NLOFR8842	9.88	2.29	3.42	43.80	0.08	1.22	0.05	0.78	0.52	1.15	33.56	96.73
NLOFR8843	10.76	3.19	11.43	37.19	0.39	1.12	1.08	0.60	0.41	14.83	16.20	97.20
NLOFR8844	33.24	5.38	12.52	20.77	0.27	5.05	2.98	1.16	0.35	7.29	9.89	98.88
NLOFR8845	26.10	1.90	13.79	27.04	0.93	5.17	0.58	0.29	0.29	5.47	16.03	97.60

Whole Rock Geochemistry – Major Oxides

Appendix D-2

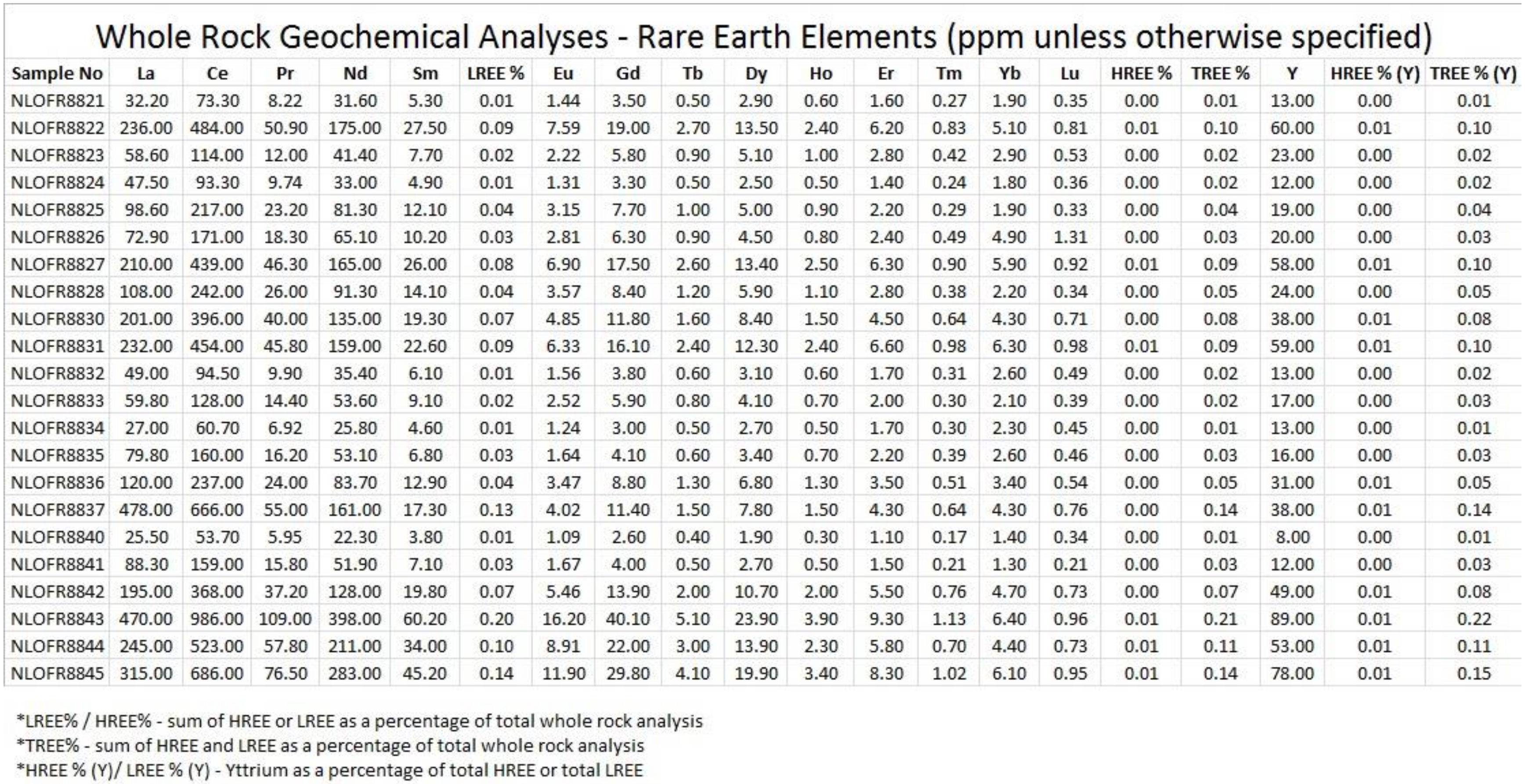

Whole Rock Geochemical Analyses - Rare Earth Elements (ppm unless otherwise specified)

Sample No	La	Ce	Pr	Nd	Sm	LREE %	Eu	Gd	Tb	Dy	Ho	Er	Tm	Yb	Lu	HREE %	TREE %	Y	HREE % (Y)	TREE % (Y)
NLOFR8821	32.20	73.30	8.22	31.60	5.30	0.01	1.44	3.50	0.50	2.90	0.60	1.60	0.27	1.90	0.35	0.00	0.01	13.00	0.00	0.01
NLOFR8822	236.00	484.00	50.90	175.00	27.50	0.09	7.59	19.00	2.70	13.50	2.40	6.20	0.83	5.10	0.81	0.01	0.10	60.00	0.01	0.10
NLOFR8823	58.60	114.00	12.00	41.40	7.70	0.02	2.22	5.80	0.90	5.10	1.00	2.80	0.42	2.90	0.53	0.00	0.02	23.00	0.00	0.02
NLOFR8824	47.50	93.30	9.74	33.00	4.90	0.01	1.31	3.30	0.50	2.50	0.50	1.40	0.24	1.80	0.36	0.00	0.02	12.00	0.00	0.02
NLOFR8825	98.60	217.00	23.20	81.30	12.10	0.04	3.15	7.70	1.00	5.00	0.90	2.20	0.29	1.90	0.33	0.00	0.04	19.00	0.00	0.04
NLOFR8826	72.90	171.00	18.30	65.10	10.20	0.03	2.81	6.30	0.90	4.50	0.80	2.40	0.49	4.90	1.31	0.00	0.03	20.00	0.00	0.03
NLOFR8827	210.00	439.00	46.30	165.00	26.00	0.08	6.90	17.50	2.60	13.40	2.50	6.30	0.90	5.90	0.92	0.01	0.09	58.00	0.01	0.10
NLOFR8828	108.00	242.00	26.00	91.30	14.10	0.04	3.57	8.40	1.20	5.90	1.10	2.80	0.38	2.20	0.34	0.00	0.05	24.00	0.00	0.05
NLOFR8830	201.00	396.00	40.00	135.00	19.30	0.07	4.85	11.80	1.60	8.40	1.50	4.50	0.64	4.30	0.71	0.00	0.08	38.00	0.01	0.08
NLOFR8831	232.00	454.00	45.80	159.00	22.60	0.09	6.33	16.10	2.40	12.30	2.40	6.60	0.98	6.30	0.98	0.01	0.09	59.00	0.01	0.10
NLOFR8832	49.00	94.50	9.90	35.40	6.10	0.01	1.56	3.80	0.60	3.10	0.60	1.70	0.31	2.60	0.49	0.00	0.02	13.00	0.00	0.02
NLOFR8833	59.80	128.00	14.40	53.60	9.10	0.02	2.52	5.90	0.80	4.10	0.70	2.00	0.30	2.10	0.39	0.00	0.02	17.00	0.00	0.03
NLOFR8834	27.00	60.70	6.92	25.80	4.60	0.01	1.24	3.00	0.50	2.70	0.50	1.70	0.30	2.30	0.45	0.00	0.01	13.00	0.00	0.01
NLOFR8835	79.80	160.00	16.20	53.10	6.80	0.03	1.64	4.10	0.60	3.40	0.70	2.20	0.39	2.60	0.46	0.00	0.03	16.00	0.00	0.03
NLOFR8836	120.00	237.00	24.00	83.70	12.90	0.04	3.47	8.80	1.30	6.80	1.30	3.50	0.51	3.40	0.54	0.00	0.05	31.00	0.01	0.05
NLOFR8837	478.00	666.00	55.00	161.00	17.30	0.13	4.02	11.40	1.50	7.80	1.50	4.30	0.64	4.30	0.76	0.00	0.14	38.00	0.01	0.14
NLOFR8840	25.50	53.70	5.95	22.30	3.80	0.01	1.09	2.60	0.40	1.90	0.30	1.10	0.17	1.40	0.34	0.00	0.01	8.00	0.00	0.01
NLOFR8841	88.30	159.00	15.80	51.90	7.10	0.03	1.67	4.00	0.50	2.70	0.50	1.50	0.21	1.30	0.21	0.00	0.03	12.00	0.00	0.03
NLOFR8842	195.00	368.00	37.20	128.00	19.80	0.07	5.46	13.90	2.00	10.70	2.00	5.50	0.76	4.70	0.73	0.00	0.07	49.00	0.01	0.08
NLOFR8843	470.00	986.00	109.00	398.00	60.20	0.20	16.20	40.10	5.10	23.90	3.90	9.30	1.13	6.40	0.96	0.01	0.21	89.00	0.01	0.22
NLOFR8844	245.00	523.00	57.80	211.00	34.00	0.10	8.91	22.00	3.00	13.90	2.30	5.80	0.70	4.40	0.73	0.01	0.11	53.00	0.01	0.11
NLOFR8845	315.00	686.00	76.50	283.00	45.20	0.14	11.90	29.80	4.10	19.90	3.40	8.30	1.02	6.10	0.95	0.01	0.14	78.00	0.01	0.15

*LREE% / HREE% - sum of HREE or LREE as a percentage of total whole rock analysis
*TREE% - sum of HREE and LREE as a percentage of total whole rock analysis
*HREE % (Y)/ LREE % (Y) - Yttrium as a percentage of total HREE or total LREE

Whole Rock Geochemistry – Rare Earth Elements

Appendix D-3

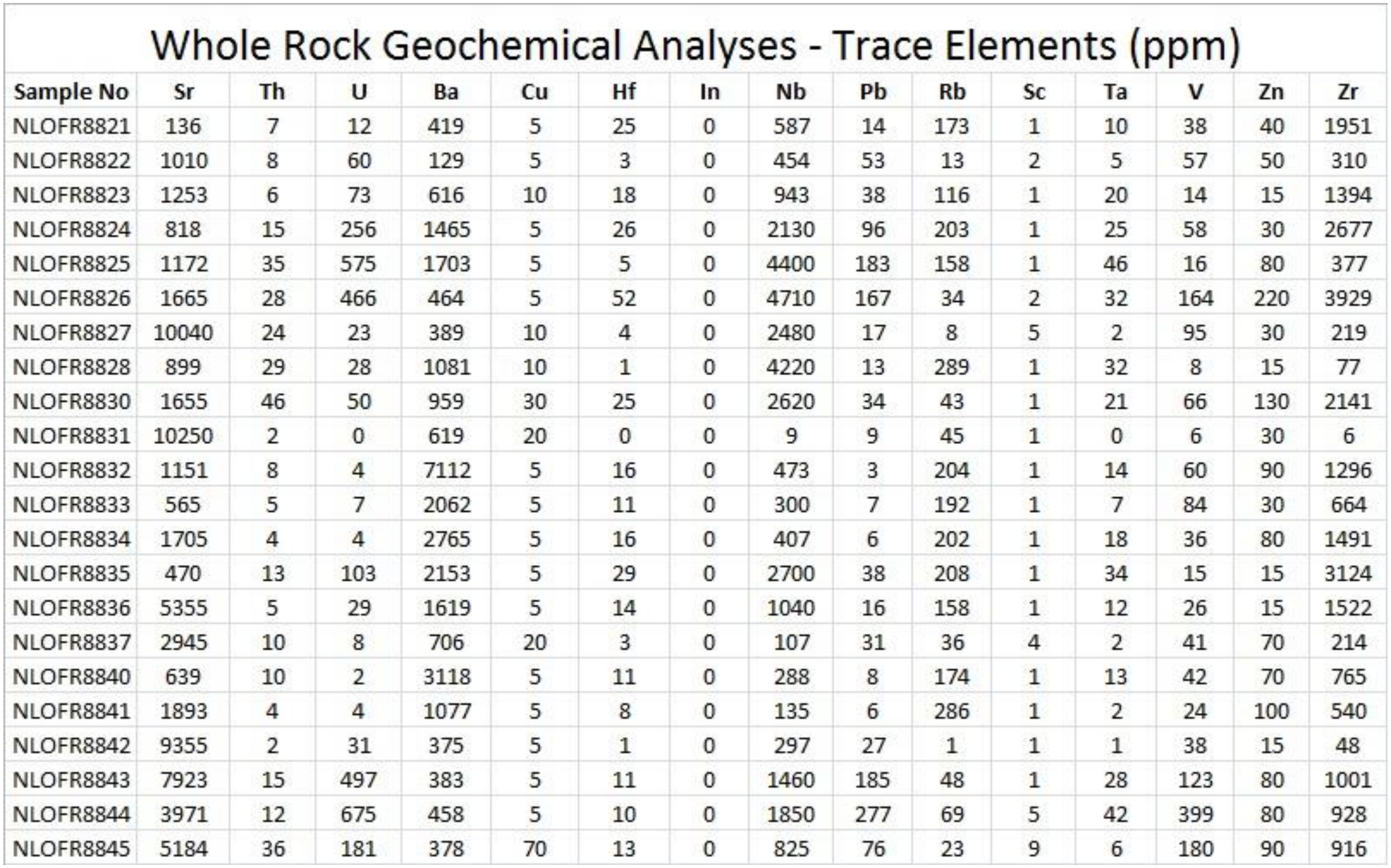

Whole Rock Geochemical Analyses - Trace Elements (ppm)

Sample No	Sr	Th	U	Ba	Cu	Hf	In	Nb	Pb	Rb	Sc	Ta	V	Zn	Zr
NLOFR8821	136	7	12	419	5	25	0	587	14	173	1	10	38	40	1951
NLOFR8822	1010	8	60	129	5	3	0	454	53	13	2	5	57	50	310
NLOFR8823	1253	6	73	616	10	18	0	943	38	116	1	20	14	15	1394
NLOFR8824	818	15	256	1465	5	26	0	2130	96	203	1	25	58	30	2677
NLOFR8825	1172	35	575	1703	5	5	0	4400	183	158	1	46	16	80	377
NLOFR8826	1665	28	466	464	5	52	0	4710	167	34	2	32	164	220	3929
NLOFR8827	10040	24	23	389	10	4	0	2480	17	8	5	2	95	30	219
NLOFR8828	899	29	28	1081	10	1	0	4220	13	289	1	32	8	15	77
NLOFR8830	1655	46	50	959	30	25	0	2620	34	43	1	21	66	130	2141
NLOFR8831	10250	2	0	619	20	0	0	9	9	45	1	0	6	30	6
NLOFR8832	1151	8	4	7112	5	16	0	473	3	204	1	14	60	90	1296
NLOFR8833	565	5	7	2062	5	11	0	300	7	192	1	7	84	30	664
NLOFR8834	1705	4	4	2765	5	16	0	407	6	202	1	18	36	80	1491
NLOFR8835	470	13	103	2153	5	29	0	2700	38	208	1	34	15	15	3124
NLOFR8836	5355	5	29	1619	5	14	0	1040	16	158	1	12	26	15	1522
NLOFR8837	2945	10	8	706	20	3	0	107	31	36	4	2	41	70	214
NLOFR8840	639	10	2	3118	5	11	0	288	8	174	1	13	42	70	765
NLOFR8841	1893	4	4	1077	5	8	0	135	6	286	1	2	24	100	540
NLOFR8842	9355	2	31	375	5	1	0	297	27	1	1	1	38	15	48
NLOFR8843	7923	15	497	383	5	11	0	1460	185	48	1	28	123	80	1001
NLOFR8844	3971	12	675	458	5	10	0	1850	277	69	5	42	399	80	928
NLOFR8845	5184	36	181	378	70	13	0	825	76	23	9	6	180	90	916

Whole Rock Geochemistry – Trace Elements